

CITATION REPORT

List of articles citing

User-guided 3D active contour segmentation of anatomical structures: significantly improved efficiency and reliability

DOI: 10.1016/j.neuroimage.2006.01.015
NeuroImage, 2006, 31, 1116-28.

Source: <https://exaly.com/paper-pdf/39689043/citation-report.pdf>

Version: 2024-04-10

This report has been generated based on the citations recorded by exaly.com for the above article. For the latest version of this publication list, visit the link given above.

The third column is the impact factor (IF) of the journal, and the fourth column is the number of citations of the article.

#	Paper	IF	Citations
2220	The Path-Ordered Formalism and Thermo Field Dynamics in Nonequilibrium Phenomena. 1987 , 4, 153-157		8
2219	Application of a Constrained Multi-Variable Controller to a Hydrogen Plant. 1989 ,		1
2218	.		
2217	Deformable registration of diffusion tensor MR images with explicit orientation optimization. 2006 , 10, 764-85		377
2216	Spinal crawlers: deformable organisms for spinal cord segmentation and analysis. 2006 , 9, 808-15		22
2215	Fiber tract-oriented statistics for quantitative diffusion tensor MRI analysis. 2006 , 10, 786-98		130
2214	Image analysis and superimposition of 3-dimensional cone-beam computed tomography models. 2006 , 129, 611-8		226
2213	Three-dimensional magnetic resonance microscopy of pulmonary solitary tumors in transgenic mice. 2006 , 56, 698-703		13
2212	Mapping Genetic Influences on Brain Shape using Multi-Atlas Fluid Image Alignment. 2007 , 2007, 482-489		
2211	Automatic brain segmentation in rhesus monkeys. 2007 , 6512, 883		14
2210	Early postnatal development of corpus callosum and corticospinal white matter assessed with quantitative tractography. 2007 , 28, 1789-95		94
2209	Subcortical structure segmentation using probabilistic atlas priors. 2007 ,		20
2208	Asymmetric bias in user guided segmentations of brain structures. 2007 ,		1
2207	Effects of heavy in utero cocaine exposure on adolescent caudate morphology. 2007 , 37, 275-9		54
2206	Hippocampus-specific fMRI group activation analysis using the continuous medial representation. <i>NeuroImage</i> , 2007 , 35, 1516-30	7.9	22
2205	Automatic segmentation of the caudate nucleus from human brain MR images. 2007 , 26, 509-17		31
2204	Measuring Cortical Thickness Using An Image Domain Local Surface Model And Topology Preserving Segmentation. 2007 ,		

2203	Shape-based normalization of the corpus callosum for DTI connectivity analysis. 2007 , 26, 1166-78	17
2202	Automating the Extraction of 3D Models from Medical Images for Virtual Reality and Haptic Simulations. 2007 ,	5
2201	Feasibility of using interpolated contours of targets and organs-at-risk in intensity-modulated radiation therapy treatment planning for advanced-stage NPC. 2007 , 1965-1968	
2200	A context-sensitive active contour for 2D corpus callosum segmentation. 2007 , 2007, 24826	16
2199	Validation of plaster endocast morphology through 3D CT image analysis. 2007 , 132, 183-92	30
2198	Asymmetrical ventricular enlargement in Parkinson's disease. 2007 , 22, 1657-60	9
2197	Brain mapping as a tool to study neurodegeneration. 2007 , 4, 387-400	45
2196	Corpus callosum morphology and ventricular size in chromosome 22q11.2 deletion syndrome. 2007 , 1131, 197-210	43
2195	Three dimensional digital atlas of the orbit constructed from multi-modal radiological images. 2007 , 1, 275-283	7
2194	Endothelial cell colonization and angiogenic potential of combined nano- and micro-fibrous scaffolds for bone tissue engineering. 2008 , 29, 4306-13	154
2193	Comparison of conventional MRI and 3D reconstruction model for evaluation of temporomandibular joint. 2008 , 30, 663-7	20
2192	A hybrid approach for segmentation of anatomic structures in medical images. 2008 , 3, 213-219	10
2191	Automatic localization of anatomical point landmarks for brain image processing algorithms. 2008 , 6, 135-48	9
2190	Systematic comparison and reconstruction of sea urchin (Echinoidea) internal anatomy: a novel approach using magnetic resonance imaging. 2008 , 6, 33	49
2189	EndoCAS navigator platform: a common platform for computer and robotic assistance in minimally invasive surgery. 2008 , 4, 242-51	20
2188	Efficient interactive 3D Livewire segmentation of complex objects with arbitrary topology. 2008 , 32, 639-50	37
2187	A model-based, semi-global segmentation approach for automatic 3-D point landmark localization in neuroimages. 2008 , 27, 1034-44	19
2186	Mapping progressive brain structural changes in early Alzheimer's disease and mild cognitive impairment. 2008 , 46, 1597-612	90

2185	Lowering the Barriers to Cancer Imaging. 2008 ,		12
2184	Absence of regional brain volume change in schizophrenia associated with short-term atypical antipsychotic treatment. 2008 , 98, 29-39		27
2183	Prenatal mild ventriculomegaly predicts abnormal development of the neonatal brain. 2008 , 64, 1069-76		54
2182	ECoG gamma activity during a language task: differentiating expressive and receptive speech areas. 2008 , 131, 2013-27		208
2181	Alterations of striatal glutamate transmission in rotenone-treated mice: MRI/MRS in vivo studies. 2008 , 209, 224-33		9
2180	Structural consequences of diffuse traumatic brain injury: a large deformation tensor-based morphometry study. <i>NeuroImage</i> , 2008 , 39, 1014-26	7.9	119
2179	Automated ventricular mapping with multi-atlas fluid image alignment reveals genetic effects in Alzheimer's disease. <i>NeuroImage</i> , 2008 , 40, 615-630	7.9	64
2178	Structure-specific statistical mapping of white matter tracts. <i>NeuroImage</i> , 2008 , 41, 448-61	7.9	138
2177	Validation of a fully automated 3D hippocampal segmentation method using subjects with Alzheimer's disease mild cognitive impairment, and elderly controls. <i>NeuroImage</i> , 2008 , 43, 59-68	7.9	162
2176	Evidence of rapid ongoing brain development beyond 2 years of age detected by fiber tracking. 2008 , 29, 1261-5		25
2175	Preoperative brain shift: study of three surgical cases. 2008 ,		1
2174	Localization and Atlas-Based Segmentation of the Heart from Cardiac MR Images: Validation with a Large Clinical Trial. 2008 ,		1
2173	Automatic and robust forearm segmentation using graph cuts. 2008 ,		10
2172	Navigation in laparoscopy--prototype research platform for improved image-guided surgery. 2008 , 17, 17-33		23
2171	Subjective cognitive failures and hippocampal volume in elderly with white matter lesions. 2008 , 71, 1152-9		81
2170	A structural MRI study of human brain development from birth to 2 years. 2008 , 28, 12176-82		725
2169	Combined Inactivation of MYC and K-Ras oncogenes reverses tumorigenesis in lung adenocarcinomas and lymphomas. 2008 , 3, e2125		71
2168	Identifying the human optic radiation using diffusion imaging and fiber tractography. 2008 , 8, 12.1-11		104

2167 Non-rigid registration based segmentation of brain subcortical structures using a priori knowledge. **2008**, 2008, 3971-4

2166 . **2008**, 6

2165 Heavy-ion radiotherapy treatment planning system and medical image processing algorithm used in it. **2008**, 2

2164 A least squares approach to estimating the probability distribution of unobserved data in multiphoton microscopy. **2008**, 1

2163 Integration of a real-time video grabber component with the open source image-guided surgery toolkit IGSTK. **2008**,

2162 Segmentation of Brain Internal Structures Automatically Using Non-rigid Registration with Simultaneous Intensity and Geometric Match. **2008**,

2161 Rapid prototyping of clinical software assistants. **2008**,

2160 Automatic regional analysis of DTI properties in the developmental macaque brain. **2008**, 3

2159 Practical contour segmentation algorithm for small animal digital radiography image. **2008**,

2158 [Three-dimensional superimposition of the skull base for the longitudinal evaluation of the effects of growth and of treatment]. **2009**, 80, 347-57 27

2157 Radial biases in the processing of motion and motion-defined contours by human visual cortex. **2009**, 102, 2974-81 21

2156 BDNF genotype modulates resting functional connectivity in children. **2009**, 3, 55 38

2155 Segmentation, tracking, and analysis of focal adhesion dynamics in cellular microscopy imaging. **2009**, 1

2154 Cortical enhanced tissue segmentation of neonatal brain MR images acquired by a dedicated phased array coil. **2009**, 2

2153 Visualization and Processing of Tensor Fields. **2009**, 11

2152 Bone remodelling analysis of a bovine femur for a veterinary implant design. **2009**, 12, 683-90 6

2151 Multi-parameter segmentation of brain images. **2009**,

2150 Soft X-ray tomography of phenotypic switching and the cellular response to antifungal peptoids in *Candida albicans*. **2009**, 106, 19375-80 114

2149	Brain Tissue Segmentation of Neonatal MR Images Using a Longitudinal Subject-specific Probabilistic Atlas. 2009 , 7259,	5
2148	Diffusion tensor imaging detects abnormalities in the corticospinal tracts of neonates with infantile Krabbe disease. 2009 , 30, 1017-21	55
2147	Hydrodynamic limb vein injection of adeno-associated virus serotype 8 vector carrying canine myostatin propeptide gene into normal dogs enhances muscle growth. 2009 , 20, 1-10	77
2146	Cerebral white matter integrity mediates adult age differences in cognitive performance. 2009 , 21, 289-302	197
2145	Longitudinal study of amygdala volume and joint attention in 2- to 4-year-old children with autism. 2009 , 66, 509-16	165
2144	Murine Glut-1 transporter haploinsufficiency: postnatal deceleration of brain weight and reactive astrogliosis. 2009 , 36, 60-9	25
2143	Comparison and evaluation of methods for liver segmentation from CT datasets. 2009 , 28, 1251-65	650
2142	Distributed local MRF models for tissue and structure brain segmentation. 2009 , 28, 1278-95	50
2141	Using the stochastic collocation method for the uncertainty quantification of drug concentration due to depot shape variability. 2009 , 56, 609-20	9
2140	A hybrid geometric-statistical deformable model for automated 3-D segmentation in brain MRI. 2009 , 56, 1838-48	31
2139	Interactive segmentation framework of the Medical Imaging Interaction Toolkit. 2009 , 96, 72-83	71
2138	Automated 3D mapping of hippocampal atrophy and its clinical correlates in 400 subjects with Alzheimer's disease, mild cognitive impairment, and elderly controls. 2009 , 30, 2766-88	153
2137	Mapping brain abnormalities in boys with autism. 2009 , 30, 3887-900	46
2136	Parametric surface modeling and registration for comparison of manual and automated segmentation of the hippocampus. 2009 , 19, 588-95	25
2135	Appearance and incomplete label matching for diffeomorphic template based hippocampus segmentation. 2009 , 19, 565-71	37
2134	Spiny versus stubby: 3D reconstruction of human myenteric (type I) neurons. 2009 , 131, 1-12	13
2133	The MRI volumetry of the posterior fossa and its substructures in trigeminal neuralgia: a validated study. 2009 , 151, 669-75	27
2132	Measurement of bone cyst fluid volume using k-means clustering. 2009 , 27, 1430-9	7

2131	Dynamic edge tracing: Boundary identification in medical images. 2009 , 113, 1039-1052	9
2130	Localization and registration accuracy in image guided neurosurgery: a clinical study. 2009 , 4, 45-52	63
2129	Teasing apart the heterogeneity of autism: Same behavior, different brains in toddlers with fragile X syndrome and autism. 2009 , 1, 81-90	84
2128	Interactive skeletonization of intensity volumes. 2009 , 25, 627-635	23
2127	Magnetic resonance microscopy defines ethanol-induced brain abnormalities in prenatal mice: effects of acute insult on gestational day 8. 2009 , 33, 1001-11	112
2126	Asymmetrical lateral ventricular enlargement in Parkinson's disease. 2009 , 16, 475-81	41
2125	Simulation of brain tumors in MR images for evaluation of segmentation efficacy. 2009 , 13, 297-311	94
2124	Interactive surface-guided segmentation of brain MRI data. 2009 , 39, 1153-60	13
2123	Microstructural callosal abnormalities in normal-appearing brain of children with developmental delay detected with diffusion tensor imaging. 2009 , 19, 1537-43	6
2122	Pharyngeal airway volume and shape from cone-beam computed tomography: relationship to facial morphology. 2009 , 136, 805-14	167
2121	Superimposition of 3-dimensional cone-beam computed tomography models of growing patients. 2009 , 136, 94-9	123
2120	Working with DICOM craniofacial images. 2009 , 136, 460-70	106
2119	Discrete curvature calculation for fast level set segmentation. 2009 ,	4
2118	Hippocampal volumetry and functional MRI of memory in temporal lobe epilepsy. 2009 , 16, 128-38	33
2117	Anterior hippocampal and orbitofrontal cortical structural brain abnormalities in association with cognitive deficits in schizophrenia. 2009 , 114, 110-8	71
2116	An interactive graph cut method for brain tumor segmentation. 2009 ,	15
2115	Brain size and brain organization of the whale shark, <i>Rhincodon typus</i> , using magnetic resonance imaging. 2009 , 74, 121-42	38
2114	A high-resolution computational atlas of the human hippocampus from postmortem magnetic resonance imaging at 9.4 T. <i>NeuroImage</i> , 2009 , 44, 385-98	7.9 134

2113	Automated mapping of hippocampal atrophy in 1-year repeat MRI data from 490 subjects with Alzheimer's disease, mild cognitive impairment, and elderly controls. <i>NeuroImage</i> , 2009 , 45, S3-15	7.9	178
2112	Registration based cortical thickness measurement. <i>NeuroImage</i> , 2009 , 45, 867-79	7.9	155
2111	A comparison of automated segmentation and manual tracing for quantifying hippocampal and amygdala volumes. <i>NeuroImage</i> , 2009 , 45, 855-66	7.9	418
2110	Discrimination of the local orientation structure of spiral Glass patterns early in human visual cortex. <i>NeuroImage</i> , 2009 , 46, 511-5	7.9	53
2109	An evaluation of four automatic methods of segmenting the subcortical structures in the brain. <i>NeuroImage</i> , 2009 , 47, 1435-47	7.9	148
2108	Interactive deformation registration of endorectal prostate MRI using ITK thin plate splines. 2009 , 16, 351-7		13
2107	Automatic analysis of medial temporal lobe atrophy from structural MRIs for the early assessment of Alzheimer disease. 2009 , 36, 3737-47		26
2106	Cortical Enhanced Tissue Segmentation of Neonatal Brain MR Images Acquired by a Dedicated Phased Array Coil. 2009 , 2009, 39-45		1
2105	An automatic quantification system for MS lesions with integrated DICOM structured reporting (DICOM-SR) for implementation within a clinical environment. 2010 ,		
2104	The development of a disease oriented eFolder for multiple sclerosis decision support. 2010 ,		
2103	Simulation in neurosurgery: a review of computer-based simulation environments and their surgical applications. 2010 , 67, 1105-16		135
2102	Segmentation of polycystic kidneys from MR images. 2010 ,		3
2101	Orientation anisotropies in human visual cortex. 2010 , 103, 3465-71		70
2100	Cranial base superimposition for 3-dimensional evaluation of soft-tissue changes. 2010 , 137, S120-9		75
2099	Three-dimensional analysis of maxillary protraction with intermaxillary elastics to miniplates. 2010 , 137, 274-84		94
2098	Three-dimensional surgical simulation. 2010 , 138, 361-71		100
2097	Three-dimensional assessment of mandibular advancement 1 year after surgery. 2010 , 137, S53.e1-S53.e12		6
2096	Three-dimensional assessment of mandibular advancement 1 year after surgery. 2010 , 137, S53.e1-12; discussion S53-5		31

2095	On two equations about brain volume, cranial capacity and age. 2010 , 32, 989-95	11
2094	A topology preserving non-rigid registration algorithm with integration shape knowledge to segment brain subcortical structures from MRI images. 2010 , 43, 2418-2427	13
2093	Technique for the computation of lower leg muscle bulk from magnetic resonance images. 2010 , 32, 926-33	12
2092	An automatic geometrical and statistical method to detect acoustic shadows in intraoperative ultrasound brain images. 2010 , 14, 195-204	24
2091	An efficient two-stage approach for image-based FSI analysis of atherosclerotic arteries. 2010 , 9, 213-23	16
2090	Carotid atheroma rupture observed in vivo and FSI-predicted stress distribution based on pre-rupture imaging. 2010 , 38, 2748-65	39
2089	Abstracts: EPSM-ABEC 2009. 2010 , 33, 65-117	
2088	Comparison of manual and automated determination of hippocampal volumes in MCI and early AD. 2010 , 4, 86-95	69
2087	Online 3-D reconstruction of the right atrium from echocardiography data via a topographic cellular contour extraction algorithm. 2010 , 57, 384-96	2
2086	Needle-based interventions with the image-guided surgery toolkit (IGSTK): from phantoms to clinical trials. 2010 , 57, 922-33	43
2085	Comparison of AdaBoost and support vector machines for detecting Alzheimer's disease through automated hippocampal segmentation. 2010 , 29, 30-43	150
2084	Volumetric and semiquantitative assessment of MRI-detected subchondral bone marrow lesions in knee osteoarthritis: a comparison of contrast-enhanced and non-enhanced imaging. 2010 , 18, 1062-6	35
2083	Comparison of actual surgical outcomes and 3-dimensional surgical simulations. 2010 , 68, 2412-21	119
2082	A time-saving and facilitating approach for segmentation of anatomically defined cortical regions: MRI volumetry. 2010 , 181, 211-8	9
2081	Manual validation of FreeSurfer's automated hippocampal segmentation in normal aging, mild cognitive impairment, and Alzheimer Disease subjects. 2010 , 181, 219-25	79
2080	Machines that learn to segment images: a crucial technology for connectomics. 2010 , 20, 653-66	111
2079	Three methods assessing red marrow dosimetry in lymphoma patients treated with radioimmunotherapy. 2010 , 116, 1093-100	24
2078	Hippocampal hyperactivation in presymptomatic familial Alzheimer's disease. 2010 , 68, 865-75	144

2077	Magnetic resonance microscopy-based analyses of the brains of normal and ethanol-exposed fetal mice. 2010 , 88, 953-64	50
2076	Comparison of segmentation methods for MRI measurement of cardiac function in rats. 2010 , 32, 869-77	23
2075	Comparative SNR for high-throughput mouse embryo MR microscopy. 2010 , 63, 1703-7	17
2074	Ultrashort echo time (UTE) MRI of the lung: assessment of tissue density in the lung parenchyma. 2010 , 64, 1491-8	77
2073	Determination of three-dimensional ventricular strain distributions in gene-targeted mice using tagged MRI. 2010 , 64, 1281-8	27
2072	Segmentation of image ensembles via latent atlases. 2010 , 14, 654-65	53
2071	A computational model of cerebral cortex folding. 2010 , 264, 467-78	48
2070	Building generic anatomical models using virtual model cutting and iterative registration. 2010 , 10, 5	
2069	Magnetic resonance microscopy defines ethanol-induced brain abnormalities in prenatal mice: effects of acute insult on gestational day 7. 2010 , 34, 98-111	93
2068	MRI estimation of global brain oxygen consumption rate. 2010 , 30, 1598-607	192
2067	Structural imaging of Alzheimer's disease. 313-331	
2066	Erratum. 2010 , 78, 124-124	
2065	. 2010 ,	14
2064	Aparelho de avanço mandibular aumenta o volume da via aérea superior de pacientes com apneia do sono. 2010 , 15, 166-171	4
2063	Mapping hV4 and ventral occipital cortex: the venous eclipse. 2010 , 10, 1	153
2062	Orientation-selective chromatic mechanisms in human visual cortex. 2010 , 10, 34	12
2061	Combination of subcortical color channels in human visual cortex. 2010 , 10, 25	42
2060	Deslocamentos esqueléticos associados à cirurgia de avanço mandibular: avaliação quantitativa tridimensional. 2010 , 15, 79-88	0

2059	Medial temporal lobe correlates of memory screening measures in normal aging, MCI, and AD. 2010 , 23, 100-8	18
2058	Correlation of automated volumetric analysis of brain MR imaging with cognitive impairment in a natural history study of mucopolysaccharidosis II. 2010 , 31, 1319-23	29
2057	Fluorescence microscopic imaging and image analysis of the cytoskeleton. 2010 ,	5
2056	Entorhinal cortex volume in older adults: reliability and validity considerations for three published measurement protocols. 2010 , 16, 846-55	20
2055	Hybrid echo and x-ray image guidance for cardiac catheterization procedures by using a robotic arm: a feasibility study. 2010 , 55, N371-82	13
2054	Data driven mean-shift belief propagation for non-gaussian MRFs. 2010 ,	3
2053	Variational segmentation of elongated volumetric structures. 2010 ,	11
2052	Multiscale modeling of the influence of Fe content in a AlSiCu alloy on the size distribution of intermetallic phases and micropores. 2010 , 107, 061804	19
2051	Segmentation of MRI brain data using a haptic device. 2010 ,	2
2050	Multi-function Based Modeling of 3D Heterogeneous Wound Scaffolds for Improved Wound Healing. 2010 , 7, 1-15	
2049	Augmented reality for anatomical education. 2010 , 33, 6-15	77
2048	A VISUALIZATION AND FUSION SYSTEM FOR IMAGE GUIDED RFA PROCEDURES. 2010 , 10, 155-174	
2047	ABC/XYZ estimates intracerebral hemorrhage volume as a percent of total brain volume in children. 2010 , 41, 691-4	25
2046	Selection of massive bone allografts using shape-matching 3-dimensional registration. 2010 , 81, 250-5	23
2045	Topography of covert visual attention in human superior colliculus. 2010 , 104, 3074-83	45
2044	Shells and Spheres: An n-Dimensional Framework for Medial-Based Image Segmentation. 2010 , 2010, 980872	2
2043	Respiratory motion compensated overlay of surface models from cardiac MR on interventional x-ray fluoroscopy for guidance of cardiac resynchronization therapy procedures. 2010 ,	2
2042	3D bone mineral density distribution and shape reconstruction of the proximal femur from a single simulated DXA image: an in vitro study. 2010 ,	5

2041	Formalin fixation could interfere with the clinical assessment of the tumor-free margin in tumor surgery: magnetic resonance imaging-based study. 2010 , 78, 115-24		39
2040	Predictors of outcome in childhood intracerebral hemorrhage: a prospective consecutive cohort study. 2010 , 41, 313-8		98
2039	Quantitative CT for volumetric analysis of medical images: initial results for liver tumors. 2010 ,		4
2038	Prenatal and neonatal brain structure and white matter maturation in children at high risk for schizophrenia. 2010 , 167, 1083-91		74
2037	Maturation trajectories of cortical brain development through the pubertal transition: unique species and sex differences in the monkey revealed through structural magnetic resonance imaging. 2010 , 20, 1053-63		77
2036	Attention deficits in schizophrenia--preliminary evidence of dissociable transient and sustained deficits. 2010 , 122, 104-12		44
2035	Preliminary 3D computational analysis of the relationship between aortic displacement force and direction of endograft movement. 2010 , 51, 1488-97; discussion 1497		36
2034	A neurocomputational method for fully automated 3D dendritic spine detection and segmentation of medium-sized spiny neurons. <i>NeuroImage</i> , 2010 , 50, 1472-84	7.9	29
2033	Microstructural connectivity of the arcuate fasciculus in adolescents with high-functioning autism. <i>NeuroImage</i> , 2010 , 51, 1117-25	7.9	168
2032	Construction of multi-region-multi-reference atlases for neonatal brain MRI segmentation. <i>NeuroImage</i> , 2010 , 51, 684-93	7.9	84
2031	The influence of global form on local orientation anisotropies in human visual cortex. <i>NeuroImage</i> , 2010 , 52, 600-5	7.9	22
2030	Cerebral cortical folding analysis with multivariate modeling and testing: Studies on gender differences and neonatal development. <i>NeuroImage</i> , 2010 , 53, 450-9	7.9	52
2029	Three-Dimensional Superimposition for Quantification of Treatment Outcomes. 2010 , 36-44		2
2028	Compositional-prior-guided image reconstruction algorithm for multi-modality imaging. 2010 , 1, 223-235		21
2027	3D maps localize caudate nucleus atrophy in 400 Alzheimer's disease, mild cognitive impairment, and healthy elderly subjects. 2010 , 31, 1312-25		87
2026	Quantification of condylar resorption in temporomandibular joint osteoarthritis. 2010 , 110, 110-7		105
2025	Neonatal brain image segmentation in longitudinal MRI studies. <i>NeuroImage</i> , 2010 , 49, 391-400	7.9	155
2024	Multivariate tensor-based morphometry on surfaces: application to mapping ventricular abnormalities in HIV/AIDS. <i>NeuroImage</i> , 2010 , 49, 2141-57	7.9	75

2023	Exploration of 4D MRI blood flow using stylistic visualization. 2010 , 16, 1339-47	35
2022	DigiWarp: a method for deformable mouse atlas warping to surface topographic data. 2010 , 55, 6197-214	15
2021	High resolution imaging of the medial temporal lobe in Alzheimer's disease and dementia with Lewy bodies. 2010 , 21, 1129-40	37
2020	Cells segmentation from 3-D confocal images of early zebrafish embryogenesis. 2010 , 19, 770-81	66
2019	Statistical Atlases and Computational Models of the Heart. 2010 ,	11
2018	Probabilistic interactive segmentation using multiphase level sets. 2010 ,	0
2017	3D reconstruction of both shape and Bone Mineral Density distribution of the femur from DXA images. 2010 ,	9
2016	Intuition in Medical Image Segmentation: Visualizing Graph Edge Weights. 2011 ,	
2015	Quantitative comparison of 4D MRI flow measurements to 3D computational fluid dynamics simulation of cerebrospinal fluid movement in the spinal subarachnoid space. 2011 ,	4
2014	Novel vector beamformers for EEG source imaging. 2011 ,	1
2013	Atlas-guided automated analysis of small-animal PET studies. 2011 ,	1
2012	Mobile C-arm cone-beam CT for guidance of spine surgery: image quality, radiation dose, and integration with interventional guidance. 2011 , 38, 4563-74	90
2011	Research on the segmentation of tiny multi-target in brain tissues based on support vector machines. 2011 ,	1
2010	Hybrid Artificial Intelligent Systems. 2011 ,	
2009	Combined optical and X-ray tomosynthesis breast imaging. 2011 , 258, 89-97	151
2008	Computational analysis of stresses acting on intermodular junctions in thoracic aortic endografts. 2011 , 18, 559-68	37
2007	105 Development of an augmented reality system for robotic prostatectomy: Towards reducing the learning curve. 2011 , 10, 570	
2006	Clinical application of 3D imaging for assessment of treatment outcomes. 2011 , 17, 72-80	46

2005	Design of nano- and microfiber combined scaffolds by electrospinning of collagen onto starch-based fiber meshes: a man-made equivalent of natural extracellular matrix. 2011 , 17, 463-73		51
2004	Patient Specific Hemodynamics: Combined 4D Flow-Sensitive MRI and CFD. 2011 , 27-38		5
2003	Biomechanical Aspects of Abdominal Aortic Aneurysm (AAA) and its Risk of Rupture: Fluid Structure Interaction (FSI) Studies. 2011 , 181-220		6
2002	Computational Analysis of Displacement Forces Acting on Endografts Used to Treat Aortic Aneurysms. 2011 , 221-246		5
2001	Regional volume analysis of the Parkinson disease brain in early disease stage: gray matter, white matter, striatum, and thalamus. 2011 , 32, 682-7		51
2000	A learning-based wrapper method to correct systematic errors in automatic image segmentation: consistently improved performance in hippocampus, cortex and brain segmentation. <i>NeuroImage</i> , 2011 , 55, 968-85	7.9	143
1999	DTI registration in atlas based fiber analysis of infantile Krabbe disease. <i>NeuroImage</i> , 2011 , 55, 1577-86	7.9	97
1998	The relationships between extent and microstructural properties of the midsagittal corpus callosum in human brain. <i>NeuroImage</i> , 2011 , 56, 174-84	7.9	5
1997	High-field (9.4 T) MRI of brain dysmyelination by quantitative mapping of magnetic susceptibility. <i>NeuroImage</i> , 2011 , 56, 930-8	7.9	175
1996	Direct visualization of non-human primate subcortical nuclei with contrast-enhanced high field MRI. <i>NeuroImage</i> , 2011 , 58, 60-8	7.9	12
1995	Imaging genetics in multiple sclerosis: a volumetric and diffusion tensor MRI study of APOE ϵ 4. <i>NeuroImage</i> , 2011 , 58, 724-31	7.9	5
1994	Population-averaged diffusion tensor imaging atlas of the Sprague Dawley rat brain. <i>NeuroImage</i> , 2011 , 58, 975-83	7.9	26
1993	Lesion Explorer: a comprehensive segmentation and parcellation package to obtain regional volumetrics for subcortical hyperintensities and intracranial tissue. <i>NeuroImage</i> , 2011 , 54, 963-73	7.9	92
1992	Volumetric MRI and MRS provide sensitive measures of Alzheimer's disease neuropathology in inducible Tau transgenic mice (rTg4510). <i>NeuroImage</i> , 2011 , 54, 2652-8	7.9	52
1991	Quantitative susceptibility mapping of human brain reflects spatial variation in tissue composition. <i>NeuroImage</i> , 2011 , 55, 1645-56	7.9	374
1990	Survival and death signals can predict tumor response to therapy after oncogene inactivation. 2011 , 3, 103ra99		34
1989	Biomechanics and Mechanobiology of Aneurysms. 2011 ,		16
1988	MRI-based 3D shape analysis of thigh muscles patients with chronic obstructive pulmonary disease versus healthy adults. 2011 , 18, 155-66		17

1987	Image analysis for understanding embryo development: a bridge from microscopy to biological insights. 2011 , 21, 630-7	29
1986	Anterior cingulate cortex volume and emotion regulation: is bigger better?. 2011 , 86, 379-82	73
1985	Image-based multi-scale modelling and validation of radio-frequency ablation in liver tumours. 2011 , 369, 4233-54	40
1984	Voxel-based haptic training simulator for screw insertion in knee osteotomy. 2011 ,	1
1983	Soft tissue response to mandibular advancement using 3D CBCT scanning. 2011 , 40, 353-9	44
1982	Inter-Parietal White Matter Development Predicts Numerical Performance in Young Children. 2011 , 21, 672-680	19
1981	In vivo 3-dimensional analysis of scapular kinematics: comparison of dominant and nondominant shoulders. 2011 , 20, 659-65	74
1980	Lateral ventricle volume is poor predictor of post unilateral DBS motor change for Parkinson's disease. 2011 , 17, 343-7	8
1979	Three-dimensional quantification of mandibular asymmetry through cone-beam computerized tomography. 2011 , 111, 757-70	52
1978	Rapid magnetic resonance measurement of global cerebral metabolic rate of oxygen consumption in humans during rest and hypercapnia. 2011 , 31, 1504-12	82
1977	Synergy of image analysis for animal and human neuroimaging supports translational research on drug abuse. 2011 , 2, 53	5
1976	Micro and macro pattern analyses of fMRI data support both early and late interaction of numerical and spatial information. 2011 , 5, 115	16
1975	Hippocampal shape deformation in female patients with unremitting major depressive disorder. 2011 , 32, 671-6	35
1974	High-pitch spiral computed tomography: effect on image quality and radiation dose in pediatric chest computed tomography. 2011 , 46, 116-23	130
1973	The medial sural artery as recipient vessel and the impact on the medial gastrocnemius. 2011 , 67, 382-6	11
1972	An enhanced version of ITK-SNAP for preoperative inspection and refinement of surface mesh models. 2011 ,	
1971	Image-based segmentation for characterization and quantitative analysis of the spinal cord injuries by using diffusion patterns. 2011 ,	
1970	Evaluation of an automatic multiple sclerosis lesion quantification tool in an informatics-based MS e-folder system. 2011 ,	

1969	Evaluating Design of Abdominal Aortic Aneurysm Endografts in a Patient-Specific Model Using Computational Fluid Dynamics. 2011 , 5,	4
1968	Automated segmentation and tracking for large-scale analysis of focal adhesion dynamics. 2011 , 241, 37-53	19
1967	Advanced image fusion to overlay coronary sinus anatomy with real-time fluoroscopy to facilitate left ventricular lead implantation in CRT. 2011 , 34, 226-34	29
1966	Transversal maxillary dento-alveolar changes in patients treated with active and passive self-ligating brackets: a randomized clinical trial using CBCT-scans and digital models. 2011 , 14, 222-33	63
1965	Wiring specificity in the direction-selectivity circuit of the retina. 2011 , 471, 183-8	625
1964	A computational tool to support pre-operative planning of stentless aortic valve implant. 2011 , 33, 1183-92	24
1963	Three-dimensional regional displacements after mandibular advancement surgery: one year of follow-up. 2011 , 69, 1447-57	38
1962	Medial temporal structures and memory functions in adolescents with heavy cannabis use. 2011 , 45, 1055-66	164
1961	Reduction of dorsolateral prefrontal cortex gray matter in late-life depression. 2011 , 193, 1-6	73
1960	Diffusion tensor imaging in Alzheimer's disease and dementia with Lewy bodies. 2011 , 194, 176-83	22
1959	Estimation of lung's air volume and its variations throughout respiratory CT image sequences. 2011 , 58, 152-8	9
1958	Multiple-object 2-D-3-D registration for noninvasive pose identification of fracture fragments. 2011 , 58, 1592-601	14
1957	Effect of posture change on the geometric features of the healthy carotid bifurcation. 2011 , 15, 148-54	12
1956	Reconstructing the 3D shape and bone mineral density distribution of the proximal femur from dual-energy X-ray absorptiometry. 2011 , 30, 2101-14	56
1955	Surface-based analysis methods for high-resolution functional magnetic resonance imaging. 2011 , 73, 313-322	23
1954	Magnetic resonance-based imaging in animal models of fetal alcohol spectrum disorder. 2011 , 21, 167-85	54
1953	ADC histograms predict response to anti-angiogenic therapy in patients with recurrent high-grade glioma. 2011 , 53, 291-302	83
1952	MRI-based volumetric assessment of joint effusion in knee osteoarthritis using proton density-weighted fat-suppressed and T1-weighted contrast-enhanced fat-suppressed sequences. 2011 , 40, 1581-5	18

1951	Markov surfaces: A probabilistic framework for user-assisted three-dimensional image segmentation. 2011 , 115, 1375-1383	1
1950	Neuronal tracing for connectomic studies. 2011 , 9, 159-66	30
1949	An open source multivariate framework for n-tissue segmentation with evaluation on public data. 2011 , 9, 381-400	340
1948	Modeling and Registration for Electrophysiology Procedures Based on Three-Dimensional Imaging. 2011 , 4, 116-126	9
1947	Three-dimensional reconstruction of cranial defect using active contour model and image registration. 2011 , 49, 203-11	15
1946	Outcome quantification using SPHARM-PDM toolbox in orthognathic surgery. 2011 , 6, 617-26	35
1945	15th Annual Conference of the International Society for Computer Aided Surgery. 2011 , 6, 226-295	2
1944	A fully-automatic caudate nucleus segmentation of brain MRI: application in volumetric analysis of pediatric attention-deficit/hyperactivity disorder. 2011 , 10, 105	20
1943	Gebiss: an ImageJ plugin for the specification of ground truth and the performance evaluation of 3D segmentation algorithms. 2011 , 12, 232	5
1942	How to build patient-specific synthetic abdominal anatomies. An innovative approach from physical toward hybrid surgical simulators. 2011 , 7, 202-13	31
1941	Cardiac MRI to investigate myocardial scar and coronary venous anatomy using a slow infusion of dimeglumine gadobenate in patients undergoing assessment for cardiac resynchronization therapy. 2011 , 33, 87-95	28
1940	Ventilation/perfusion imaging of the lung using ultra-short echo time (UTE) MRI in an animal model of pulmonary embolism. 2011 , 34, 539-46	39
1939	Ventilation-based segmentation of the lungs using hyperpolarized (3)He MRI. 2011 , 34, 831-41	48
1938	Combined R2* and diffusion tensor imaging changes in the substantia nigra in Parkinson's disease. 2011 , 26, 1627-32	129
1937	White matter lesions defined by diffusion tensor imaging in older adults. 2011 , 70, 465-76	86
1936	CENTS: cortical enhanced neonatal tissue segmentation. 2011 , 32, 382-96	34
1935	Simulation of blood flow in deformable vessels using subject-specific geometry and spatially varying wall properties. 2011 , 27, 1000-1016	46
1934	Prospective randomized double-blind pilot study of site-specific consensus atlas implementation for rectal cancer target volume delineation in the cooperative group setting. 2011 , 79, 481-9	67

1933	Integrating spatial fuzzy clustering with level set methods for automated medical image segmentation. 2011 , 41, 1-10	310
1932	Segmentation of 3D cell membrane images by PDE methods and its applications. 2011 , 41, 326-39	19
1931	Clinical application of SPHARM-PDM to quantify temporomandibular joint osteoarthritis. 2011 , 35, 345-52	44
1930	A strain energy filter for 3D vessel enhancement with application to pulmonary CT images. 2011 , 15, 112-24	59
1929	Finite difference neuroelectric modeling software. 2011 , 198, 359-63	4
1928	The evaluation of single-view and multi-view fusion 3D echocardiography using image-driven segmentation and tracking. 2011 , 15, 514-28	39
1927	Comparison of two methods for quantitative assessment of mandibular asymmetry using cone beam computed tomography image volumes. 2011 , 40, 351-7	33
1926	Comparison between manual and semiautomated volumetric measurements of pituitary adenomas. 2011 , 21, 365-72	3
1925	Hemorrhagic transformation of childhood arterial ischemic stroke. 2011 , 42, 941-6	56
1924	A novel research platform for electromagnetic navigated bronchoscopy using cone beam CT imaging and an animal model. 2011 , 20, 30-41	15
1923	Ultrasound-based surgical navigation for percutaneous renal intervention: In vivo measurements and in vitro assessment. 2011 ,	5
1922	Methodology to register prostate B-mode and ARFI images to MR and histology. 2011 ,	1
1921	Semi-automatic 3-D segmentation of Computed Tomographic imagery by iterative gradient-driven volume growing. 2011 ,	
1920	Optimization of image registration and application to human disc mechanics with nucleotomy. 2011 ,	
1919	An interactive approach to liver segmentation in CT based on deformable model integrated with attractor force. 2011 ,	5
1918	Superpixels, Occlusion and Stereo. 2011 ,	3
1917	Multi-function Based Modeling of 3D Heterogeneous Wound Scaffolds for Improved Wound Healing. 2011 , 8, 43-57	16
1916	Automated MR Hip Bone Segmentation. 2011 ,	4

1915	Internal motion prediction using kernel density estimation and general canonical correlation model. 2011 ,	1
1914	Magnetic resonance angiography study of a normal mouse brain for creating a three-dimensional cerebral vasculature atlas and software for labeling vessels. 2011 ,	1
1913	Targeted imaging of the spatial and temporal variation of matrix metalloproteinase activity in a porcine model of postinfarct remodeling: relationship to myocardial dysfunction. 2011 , 4, 381-91	70
1912	O-(2-18F-fluoroethyl)-L-tyrosine PET predicts failure of antiangiogenic treatment in patients with recurrent high-grade glioma. 2011 , 52, 856-64	138
1911	Color responsiveness argues against a dorsal component of human V4. 2011 , 11,	28
1910	Manganese accumulation in the olfactory bulbs and other brain regions of "asymptomatic" welders. 2011 , 121, 160-7	43
1909	Twin-singleton differences in neonatal brain structure. 2011 , 14, 268-76	19
1908	Interactive registration of 2D histology and 3D CT data for assessment of radiofrequency ablation treatment. 2011 , 2, S9	7
1907	Study of Supervised Segmentation Algorithm Based on Ant Colony for Putamen Region in Brain MRI. 2011 , 340, 357-362	
1906	Fabrication and Properties of Aligned Sr 0.6 K 0.4 Fe 2 As 2 Superconductors by High Magnetic Field Processing. 2011 , 28, 067402	3
1905	Level-set based vessel segmentation accelerated with periodic monotonic speed function. 2011 ,	12
1904	Zic2 hypomorphic mutant mice as a schizophrenia model and ZIC2 mutations identified in schizophrenia patients. 2011 , 1, 16	14
1903	A framework for automated coronary artery tracking of low axial resolution multi slice CT images. 2011 ,	
1902	Feature-based US to CT registration of the aortic root. 2011 ,	4
1901	A comparison of MR-based attenuation correction in PET versus SPECT. 2011 , 56, 4613-29	11
1900	Depressive Symptoms and Amygdala Volume in Elderly with Cerebral Small Vessel Disease: The RUN DMC Study. 2011 , 2011, 647869	8
1899	Aerobic fitness and obesity: relationship to cerebral white matter integrity in the brain of active and sedentary older adults. 2011 , 45, 1208-15	100
1898	R6/2 Huntington's disease mice develop early and progressive abnormal brain metabolism and seizures. 2012 , 32, 6456-67	60

1897	Towards a Virtual Reality Simulator for Orthognathic Basic Skills. 2012 , 162, 352-357	5
1896	Computer Vision and Graphics. 2012 ,	2
1895	Volume specific response criteria for brain metastases following salvage stereotactic radiosurgery and associated predictors of response. 2012 , 51, 629-35	24
1894	Detecting representations of recent and remote autobiographical memories in vmPFC and hippocampus. 2012 , 32, 16982-91	154
1893	Hippocampal atrophy and ventricular enlargement in normal aging, mild cognitive impairment (MCI), and Alzheimer Disease. 2012 , 26, 17-27	188
1892	Improved precision of syndesmophyte measurement for the evaluation of ankylosing spondylitis using CT: a phantom and patient study. 2012 , 57, 4683-704	12
1891	An integrated platform for image-guided cardiac resynchronization therapy. 2012 , 57, 2953-68	17
1890	Differential susceptibility to axonopathy in necrotic and non-necrotic perinatal white matter injury. 2012 , 43, 178-84	54
1889	Three-dimensional segmentation of the upper airway using cone beam CT: a systematic review. 2012 , 41, 276-84	69
1888	Towards a porous media model of the human lung. 2012 ,	4
1887	Patient-specific surgical simulator for the pre-operative planning of single-incision laparoscopic surgery with bimanual robots. 2012 , 17, 103-12	8
1886	Computer guidance system for single-incision bimanual robotic surgery. 2012 , 17, 161-71	6
1885	Safety and feasibility of high-pressure transvenous limb perfusion with 0.9% saline in human muscular dystrophy. 2012 , 20, 456-61	38
1884	Brain volume findings in 6-month-old infants at high familial risk for autism. 2012 , 169, 601-8	68
1883	Head posture influences the geometric and hemodynamic features on the healthy human carotid bifurcation. 2012 ,	
1882	Unilateral hip joint segmentation with shape priors learned from missing data. 2012 ,	1
1881	Maximum principal strain correlates with spinal cord tissue damage in contusion and dislocation injuries in the rat cervical spine. 2012 , 29, 1574-85	53
1880	Canonical and atypical E2Fs regulate the mammalian endocycle. 2012 , 14, 1192-202	99

1879	A comparison between adaptive kernel density estimation and Gaussian Mixture Regression for real-time tumour motion prediction from external surface motion. 2012,	1
1878	Fully automatic 3D segmentation of iceball for image-guided cryoablation. 2012, 2012, 2327-30	5
1877	Evaluation of 3D correspondence methods for building point distribution models of the kidney. 2012,	1
1876	Quantification of lymphedema in a rat model by 3D-active contour segmentation by magnetic resonance imaging. 2012, 10, 25-9	10
1875	Chronic prenatal ethanol exposure increases adiposity and disrupts pancreatic morphology in adult guinea pig offspring. 2012, 2, e57	31
1874	Registration-based segmentation of murine 4D cardiac micro-CT data using symmetric normalization. 2012, 57, 6125-45	13
1873	Position sensitivity in the visual word form area. 2012, 109, E1568-77	53
1872	Stimulation strength and focality of electroconvulsive therapy with individualized current amplitude: a preclinical study. 2012, 2012, 6430-3	4
1871	Fast interactive multi-region cardiac segmentation with linearly ordered labels. 2012,	20
1870	Fully automatic segmentation of the open mitral leaflets in 3D transesophageal echocardiographic images using multi-atlas label fusion and deformable medial modeling. 2012,	
1869	3D reconstruction of intervertebral discs from T1-weighted magnetic resonance images. 2012,	1
1868	Variable lung density consideration in attenuation correction of whole-body PET/MRI. 2012, 53, 977-84	44
1867	The effect of glaucoma on the optical attenuation coefficient of the retinal nerve fiber layer in spectral domain optical coherence tomography images. 2012, 53, 2424-30	63
1866	Modelling of bioimpedance measurements: unstructured mesh application to real human anatomy. 2012, 27,	10
1865	Modified Pediatric ASPECTS Correlates with Infarct Volume in Childhood Arterial Ischemic Stroke. 2012, 3, 122	25
1864	A digital atlas of the dog brain. 2012, 7, e52140	61
1863	Assessment of morphometry of pulmonary acini in mouse lungs by nondestructive imaging using multiscale microcomputed tomography. 2012, 109, 17105-10	81
1862	Real-time collision detection for long thin medical instruments in virtual reality-based simulators. 2012,	2

1861	Fermi surface nesting and spin density wave instability in the overdoped superconducting iron pnictides. 2012 , 100, 47004	1
1860	Deformable Registration of the Inflated and Deflated Lung for Cone-Beam CT-Guided Thoracic Surgery. 2012 , 8316,	2
1859	A mouse model of massive rotator cuff tears. 2012 , 94, e41	64
1858	High-performance C-arm cone-beam CT guidance of thoracic surgery. 2012 ,	3
1857	High-resolution functional magnetic resonance imaging methods for human midbrain. 2012 , e3746	5
1856	. 2012 ,	
1855	Brain tumor enhancement revealed by 3D intraoperative ultrasound imaging in a navigation system. 2012 , 57,	2
1854	Automatic lung lobe segmentation of COPD patients using iterative B-spline fitting. 2012 ,	2
1853	An automated landmark-based elastic registration technique for large deformation recovery from 4-D CT lung images. 2012 ,	1
1852	Lesion comparison of multiple sclerosis in hispanic and caucasian patients utilizing an imaging informatics-based eFolder system. 2012 ,	
1851	Predicting target vessel location on robot-assisted coronary artery bypass graft using CT to ultrasound registration. 2012 , 39, 1579-87	3
1850	High pressure nano-tomography using an iterative method. 2012 , 111, 112626	19
1849	Development of a semi-automated method for mitral valve modeling with medial axis representation using 3D ultrasound. 2012 , 39, 933-50	26
1848	Gain control in the response of human visual cortex to plaids. 2012 , 107, 2570-80	9
1847	Biophysical modeling of brain tumor progression: from unconditionally stable explicit time integration to an inverse problem with parabolic PDE constraints for model calibration. 2012 , 39, 4444-59	22
1846	Mesh generation and computational modeling techniques for bioimpedance measurements: an example using the VHP data. 2012 , 407, 012004	4
1845	3D fiber tractography with susceptibility tensor imaging. <i>NeuroImage</i> , 2012 , 59, 1290-8	7.9 76
1844	A finite element model to simulate femoral fractures in calves: testing different polymers for intramedullary interlocking nails. 2012 , 41, 838-44	7

1843	Fractional anisotropy distributions in 2- to 6-year-old children with autism. 2013 , 57, 1037-49	11
1842	Three-dimensional sonographic examination of the midbrain for computer-aided diagnosis of movement disorders. 2012 , 38, 2041-50	24
1841	Simulation-based joint estimation of body deformation and elasticity parameters for medical image analysis. 2012 , 31, 2156-2168	50
1840	Group-wise registration of point sets for statistical shape models. 2012 , 31, 2025-34	54
1839	Age-Related Changes in Vertebral Morphometry by Statistical Shape Analysis. 2012 , 30-39	1
1838	Cerebral gray and white matter changes and clinical course in metachromatic leukodystrophy. 2012 , 79, 1662-70	31
1837	Voxelized computational model for convection-enhanced delivery in the rat ventral hippocampus: comparison with in vivo MR experimental studies. 2012 , 40, 2043-58	22
1836	Effects of orthopedic maxillary expansion on nasal cavity size in growing subjects: a low dose computer tomography clinical trial. 2012 , 76, 1547-51	27
1835	A preliminary study of computer assisted evaluation of congenital tracheal stenosis: a new tool for surgical decision-making. 2012 , 76, 1552-7	19
1834	Pretreatment predictors of adverse radiation effects after radiosurgery for arteriovenous malformation. 2012 , 82, 803-8	34
1833	Improving the quality of electron tomography image volumes using pre-reconstruction filtering. 2012 , 180, 132-42	11
1832	Automatic segmentation of human facial tissue by MRI-CT fusion: a feasibility study. 2012 , 108, 1106-20	15
1831	3D hybrid wound devices for spatiotemporally controlled release kinetics. 2012 , 108, 922-31	11
1830	An analytical drilling force model and GPU-accelerated haptics-based simulation framework of the pilot drilling procedure for micro-implants surgery training. 2012 , 108, 1170-84	12
1829	Using manual prostate contours to enhance deformable registration of endorectal MRI. 2012 , 108, 330-7	9
1828	Initial experience with magnetic resonance imaging of atrial scar and co-registration with electroanatomic voltage mapping during atrial fibrillation: success and limitations. 2012 , 9, 2003-9	118
1827	A semi-automatic algorithm for determining the demyelination load in metachromatic leukodystrophy. 2012 , 19, 26-34	40
1826	Semi-automatic segmentation software for quantitative clinical brain glioblastoma evaluation. 2012 , 19, 977-85	30

1825	Morphological and tissue characterization of the medicinal fungus <i>Hericium coralloides</i> by a structural and molecular imaging platform. 2012 , 137, 1584-95	33
1824	Morphology-Based Interslice Interpolation on Manual Segmentations of Joint Bones and Muscles in MRI. 2012 ,	1
1823	Biomechanical analysis of the anterior cervical fusion. 2012 , 15, 1337-46	9
1822	Learning to see words. 2012 , 63, 31-53	93
1821	Exercise might bias skeletal-muscle fat fraction calculation from Dixon images. 2012 , 22 Suppl 2, S107-10	16
1820	Longitudinal measures of visual function, tumor volume, and prediction of visual outcomes after treatment of optic pathway gliomas. 2012 , 119, 1231-7	54
1819	Increased white matter integrity in the corpus callosum in subjects with high genetic loading for schizophrenia. 2012 , 37, 50-5	11
1818	. 2012 , 12, 464-473	35
1817	Human neural stem cells induce functional myelination in mice with severe dysmyelination. 2012 , 4, 155ra136	97
1816	Étude clinique de phase I avec bénéfice individuel direct de radioimmunothérapie du myélome multiple utilisant l'anticorps anti-CD138 marqué à l'isotope 131 (131I-B-B4). 2012 , 36, 83-93	
1815	A method for quantitative characterization of growth in the 3-D structure of rat pulmonary arteries. 2012 , 83, 146-53	16
1814	Automated threshold-independent cortex segmentation by 3D-texture analysis of HR-pQCT scans. 2012 , 51, 480-7	23
1813	Fronto-striatal circuitry and inhibitory control in autism: findings from diffusion tensor imaging tractography. 2012 , 48, 183-93	173
1812	The effect of a gadolinium-based contrast agent on diffusion tensor imaging. 2012 , 81, 1877-82	6
1811	Imaging nigral pathology and clinical progression in Parkinson's disease. 2012 , 27, 1636-43	84
1810	Longitudinal MRI contrast enhanced monitoring of early tumour development with manganese chloride (MnCl ₂) and superparamagnetic iron oxide nanoparticles (SPIOs) in a CT1258 based in vivo model of prostate cancer. 2012 , 12, 284	20
1809	Fully automated chest wall line segmentation in breast MRI by using context information. 2012 ,	7
1808	Alteration of brain volume in IL-6 overexpressing mice related to autism. 2012 , 30, 554-9	17

1807	Imaging software accuracy for 3-dimensional analysis of the upper airway. 2012 , 142, 801-13		139
1806	The ketogenic diet increases brain glucose and ketone uptake in aged rats: a dual tracer PET and volumetric MRI study. 2012 , 1488, 14-23		37
1805	Dynamic contrast-enhanced MRI in patients with luminal Crohn's disease. 2012 , 81, 3019-27		39
1804	Asymmetric bias in user guided segmentations of brain structures. <i>NeuroImage</i> , 2012 , 59, 1315-23	7.9	41
1803	Deficient MWF mapping in multiple sclerosis using 3D whole-brain multi-component relaxation MRI. <i>NeuroImage</i> , 2012 , 59, 2670-7	7.9	62
1802	High resolution MR anatomy of the subthalamic nucleus: imaging at 9.4 T with histological validation. <i>NeuroImage</i> , 2012 , 59, 2035-44	7.9	70
1801	Confirmation of functional zones within the human subthalamic nucleus: patterns of connectivity and sub-parcellation using diffusion weighted imaging. <i>NeuroImage</i> , 2012 , 60, 83-94	7.9	246
1800	Multi-stage segmentation of white matter hyperintensity, cortical and lacunar infarcts. <i>NeuroImage</i> , 2012 , 60, 2379-88	7.9	43
1799	NODDI: practical in vivo neurite orientation dispersion and density imaging of the human brain. <i>NeuroImage</i> , 2012 , 61, 1000-16	7.9	1589
1798	LABEL: pediatric brain extraction using learning-based meta-algorithm. <i>NeuroImage</i> , 2012 , 62, 1975-86	7.9	136
1797	Ultra-high resolution diffusion tensor imaging of the microscopic pathways of the medial temporal lobe. <i>NeuroImage</i> , 2012 , 62, 2065-82	7.9	48
1796	Quantitative mouse brain phenotyping based on single and multispectral MR protocols. <i>NeuroImage</i> , 2012 , 63, 1633-45	7.9	27
1795	Comportamiento de los dispositivos mandibulares en el tratamiento de la apnea del sueño. 2012 , 28, 237-242		1
1794	Do patients treated with bimaxillary surgery have more stable condylar positions than those who have undergone single-jaw surgery?. 2012 , 70, 2143-52		35
1793	A 3D interactive multi-object segmentation tool using local robust statistics driven active contours. 2012 , 16, 1216-27		56
1792	An atlas-based geometry pipeline for cardiac Hermite model construction and diffusion tensor reorientation. 2012 , 16, 1130-41		31
1791	3D Slicer as an image computing platform for the Quantitative Imaging Network. 2012 , 30, 1323-41		2965
1790	3D Medical Imaging. 2012 , 445-495		4

1789	The paradox of muscle hypertrophy in muscular dystrophy. 2012 , 23, 149-72, xii	67
1788	Dynamic in vivo glenohumeral kinematics during scapular plane abduction in healthy shoulders. 2012 , 42, 96-104	52
1787	Deformable registration of the inflated and deflated lung in cone-beam CT-guided thoracic surgery: initial investigation of a combined model- and image-driven approach. 2013 , 40, 017501	26
1786	Computational Biomechanics for Medicine. 2012 ,	0
1785	Automated analysis of small animal PET studies through deformable registration to an atlas. 2012 , 39, 1807-20	17
1784	Model generation of coronary artery bifurcations from CTA and single plane angiography. 2013 , 40, 013701	3
1783	In vivo assessment of optimal b-value range for perfusion-insensitive apparent diffusion coefficient imaging. 2012 , 39, 4832-9	41
1782	A preclinical assessment of neural stem cells as delivery vehicles for anti-amyloid therapeutics. 2012 , 7, e34097	17
1781	Mapping molecular agents distributions in whole mice hearts using born-normalized optical projection tomography. 2012 , 7, e34427	5
1780	The Digital Fish Library: using MRI to digitize, database, and document the morphological diversity of fish. 2012 , 7, e34499	37
1779	4D multi-modality tissue segmentation of serial infant images. 2012 , 7, e44596	55
1778	Improvements on the Feasibility of Active Shape Model-based Subthalamic Nucleus Segmentation. 2012 , 57,	2
1777	Modeling center-surround configurations in population receptive fields using fMRI. 2012 , 12, 10	83
1776	Methodology for reconstructing early zebrafish development from in vivo multiphoton microscopy. 2012 , 21, 2335-40	13
1775	MRI-leukoaraiosis thresholds and the phenotypic expression of dementia. 2012 , 79, 734-40	40
1774	A novel MRI-compatible brain ventricle phantom for validation of segmentation and volumetry methods. 2012 , 36, 476-82	11
1773	Combined magnitude and phase-based segmentation of the cerebral cortex in 7T MR images of the elderly. 2012 , 36, 99-109	5
1772	Accuracy of the cylinder approximation for susceptometric measurement of intravascular oxygen saturation. 2012 , 67, 808-13	30

1771	Automatic segmentation of amyloid plaques in MR images using unsupervised support vector machines. 2012 , 67, 1794-802	9
1770	Prospective high-resolution respiratory-resolved whole-heart MRI for image-guided cardiovascular interventions. 2012 , 68, 205-13	9
1769	The effect of augmented real-time image guidance on task workload during endoscopic sinus surgery. 2012 , 2, 405-10	26
1768	Enabling user-guided segmentation and tracking of surface-labeled cells in time-lapse image sets of living tissues. 2012 , 81, 409-18	45
1767	Interactive segmentation and tracking in optical microscopic images. 2012 , 81, 357-9	3
1766	Dosimetry results suggest feasibility of radioimmunotherapy using anti-CD138 (B-B4) antibody in multiple myeloma patients. 2012 , 33, 679-88	43
1765	Automatic subarachnoid space segmentation and hemorrhage detection in clinical head CT scans. 2012 , 7, 507-16	23
1764	3D quantification of mandibular asymmetry using the SPHARM-PDM tool box. 2012 , 7, 265-71	26
1763	An effective visualisation and registration system for image-guided robotic partial nephrectomy. 2012 , 6, 23-31	45
1762	Common atlas format and 3D brain atlas reconstructor: infrastructure for constructing 3D brain atlases. 2012 , 10, 181-97	36
1761	Radiation dose considerations by intra-individual Monte Carlo simulations in dual source spiral coronary computed tomography angiography with electrocardiogram-triggered tube current modulation and adaptive pitch. 2012 , 22, 569-78	4
1760	Fast optimization-based elasticity parameter estimation using reduced models. 2012 , 28, 553-562	5
1759	Evaluation of texture for classification of abdominal aortic aneurysm after endovascular repair. 2012 , 25, 369-76	20
1758	Two anatomic resources of canine pelvic limb muscles based on CT and MRI. 2012 , 53, 266-72	2
1757	The effect of phonation into a straw on the vocal tract adjustments and formant frequencies. A preliminary MRI study on a single subject completed with acoustic results. 2012 , 7, 50-57	37
1756	Biomedical systems researchNew perspectives opened by quantitative medical imaging. 2012 , 36, 1-9	6
1755	Computational methods and challenges for large-scale circuit mapping. 2012 , 22, 162-9	60
1754	Dynamic contrast-enhanced MRI of Gd-albumin delivery to the rat hippocampus in vivo by convection-enhanced delivery. 2012 , 209, 62-73	13

1753	Registration of 3D trans-esophageal echocardiography to X-ray fluoroscopy using image-based probe tracking. 2012 , 16, 38-49	81
1752	Multi-modal registration of speckle-tracked freehand 3D ultrasound to CT in the lumbar spine. 2012 , 16, 675-86	22
1751	Quantitative comparison between a multiecho sequence and a single-echo sequence for susceptibility-weighted phase imaging. 2012 , 30, 722-30	21
1750	High b-value diffusion-weighted imaging: a sensitive method to reveal white matter differences in schizophrenia. 2012 , 201, 144-51	18
1749	Comparison of the endocranial ontogenies between chimpanzees and bonobos via temporal regression and spatiotemporal registration. 2012 , 62, 74-88	57
1748	Particle filter with a mode tracker for visual tracking across illumination changes. 2012 , 21, 2340-6	28
1747	Diffusion tensor imaging of the hippocampus and verbal memory performance: the RUN DMC study. 2012 , 33, 542-51	36
1746	Age-related changes of digital endocranial volume during human ontogeny: results from an osteological reference collection. 2012 , 147, 312-8	25
1745	TREK: an integrated system architecture for intraoperative cone-beam CT-guided surgery. 2012 , 7, 159-73	30
1744	Canine models of Duchenne muscular dystrophy and their use in therapeutic strategies. 2012 , 23, 85-108	117
1743	Value of multidetector computed tomography image segmentation for preoperative planning in general surgery. 2012 , 26, 616-26	32
1742	External tissue support and fluid-structure simulation in blood flows. 2012 , 11, 1-18	153
1741	Quantitative phenotyping of inflammatory bowel disease in the IL-10-deficient mouse by use of noninvasive magnetic resonance imaging. 2013 , 19, 185-93	24
1740	Skeletal age assessment in children using an open compact MRI system. 2013 , 69, 1697-702	51
1739	An optimal design for patient-specific templates for pedicle spine screws placement. 2013 , 9, 298-304	22
1738	Fatigue design of a mechanically biocompatible lattice for a proof-of-concept femoral stem. 2013 , 22, 65-83	57
1737	Deformable templates guided discriminative models for robust 3D brain MRI segmentation. 2013 , 11, 447-68	8
1736	Novel role for vinculin in ventricular myocyte mechanics and dysfunction. 2013 , 104, 1623-33	26

1735	An optical tracker based robot registration and servoing method for ultrasound guided percutaneous renal access. 2013 , 12, 47	10
1734	A two-stage rule-constrained seedless region growing approach for mandibular body segmentation in MRI. 2013 , 8, 723-32	5
1733	A computerized MRI biomarker quantification scheme for a canine model of Duchenne muscular dystrophy. 2013 , 8, 763-74	29
1732	3D Imaging in Dental Research and Practice. 2013 , 8, 243-247	
1731	Association of grey matter volume deviation with insight impairment in first-episode affective and non-affective psychosis. 2013 , 263, 133-41	21
1730	iBEAT: A toolbox for infant brain magnetic resonance image processing. 2013 , 11, 211-25	62
1729	Thiazolidinediones partially reverse the metabolic disturbances observed in Bslc2/seipin-deficient mice. 2013 , 56, 1813-25	65
1728	Altered diffusion tensor imaging measurements in aged transgenic Huntington disease rats. 2013 , 218, 767-78	16
1727	Surgeons blinded by enhanced navigation: the effect of augmented reality on attention. 2013 , 27, 454-61	84
1726	Multidimensional analysis of fetal posterior fossa in health and disease. 2013 , 12, 632-44	24
1725	High spatial and temporal resolution 4D FEM simulation of the thoracic bioimpedance using MRI scans. 2013 , 434, 012074	1
1724	Contributions of the hippocampal subfields and entorhinal cortex to disambiguation during working memory. 2013 , 23, 467-75	37
1723	An algorithm to estimate anatomical connectivity between brain regions using diffusion MRI. 2013 , 31, 353-8	1
1722	Lumbar spine segmentation using a statistical multi-vertebrae anatomical shape+pose model. 2013 , 32, 1890-900	86
1721	A multichannel Markov random field framework for tumor segmentation with an application to classification of gene expression-based breast cancer recurrence risk. 2013 , 32, 637-48	39
1720	Effect of head posture on the healthy human carotid bifurcation hemodynamics. 2013 , 51, 207-18	13
1719	Toward a comprehensive framework for the spatiotemporal statistical analysis of longitudinal shape data. 2013 , 103, 22-59	85
1718	A proposed mechanism for the observed ontogenetic improvement in the hearing ability of hapuka (Polyprion oxygeneios). 2013 , 199, 653-61	8

1717	Segmentation and volumetric analysis of the caudate nucleus in Alzheimer's disease. 2013 , 82, 1525-30	42
1716	3D brain atlas reconstructor service--online repository of three-dimensional models of brain structures. 2013 , 11, 507-18	11
1715	Hybrid Artificial Intelligent Systems. 2013 ,	
1714	Repetitive and self-injurious behaviors: associations with caudate volume in autism and fragile X syndrome. 2013 , 5, 12	64
1713	The influence of fetal ethanol exposure on subsequent development of the cerebral cortex as revealed by magnetic resonance imaging. 2013 , 37, 924-32	33
1712	Magnetic resonance microscopy-based analyses of the neuroanatomical effects of gestational day 9 ethanol exposure in mice. 2013 , 39, 77-83	34
1711	Higher iron in the red nucleus marks Parkinson's dyskinesia. 2013 , 34, 1497-503	53
1710	Neurofeedback training induces changes in white and gray matter. 2013 , 44, 265-72	84
1709	Sexual dimorphism in the human corpus callosum: an MRI study using the OASIS brain database. 2013 , 23, 2514-20	69
1708	Parcellation of the human substantia nigra based on anatomical connectivity to the striatum. <i>NeuroImage</i> , 2013 , 81, 191-198	7.9 44
1707	Content-based image retrieval of multiphase CT images for focal liver lesion characterization. 2013 , 40, 103502	13
1706	Automated quantification of white matter lesion in magnetic resonance imaging of patients with acute infarction. 2013 , 213, 138-46	38
1705	Human cortical and behavioral sensitivity to patterns of complex motion at eccentricity. 2013 , 110, 2545-56	9
1704	Experimental validation of finite element model for proximal composite femur using optical measurements. 2013 , 21, 86-94	61
1703	Topographic representation of numerosity in the human parietal cortex. 2013 , 341, 1123-6	320
1702	Temporomandibular joint condylar changes following maxillomandibular advancement and articular disc repositioning. 2013 , 71, 1759.e1-15	47
1701	Mapping region-specific longitudinal cortical surface expansion from birth to 2 years of age. 2013 , 23, 2724-33	155
1700	Orthodontic and Orthognathic Planning Using Cone Beam Computed Tomography. 2013 , 91-107	

1699	One-year assessment of surgical outcomes in Class III patients using cone beam computed tomography. 2013 , 42, 780-9	18
1698	Smart Brush: A real time segmentation tool for 3D medical images. 2013 ,	8
1697	Involvement of neuronal IL-1 β in acquired brain lesions in a rat model of neonatal encephalopathy. 2013 , 10, 110	27
1696	Automatic intracranial space segmentation for computed tomography brain images. 2013 , 26, 563-71	4
1695	Changes in geometric configuration and biomechanical parameters of a rapidly growing abdominal aortic aneurysm may provide insight in aneurysms natural history and rupture risk. 2013 , 10, 67	10
1694	3D time series analysis of cell shape using Laplacian approaches. 2013 , 14, 296	13
1693	Performance divergence with data discrepancy: a review. 2013 , 40, 429-455	6
1692	Description and assessment of a registration-based approach to include bones for attenuation correction of whole-body PET/MRI. 2013 , 40, 082509	32
1691	A three-dimensional finite element model of human atrial anatomy: new methods for cubic Hermite meshes with extraordinary vertices. 2013 , 17, 525-37	31
1690	Anatomical variability predicts individual differences in transcranial electric stimulation motor threshold. 2013 , 2013, 815-8	4
1689	Sketch-Based Editing Tools for Tumour Segmentation in 3D Medical Images. 2013 , 32, 144-157	22
1688	A deformable model to segment discontinuous boundaries of bone fractures in X-ray images. 2013 ,	
1687	Synthetic reconstruction of human carotid vasculature using a 2-D/3-D interface. 2013 ,	7
1686	. 2013 ,	2
1685	Design of 3-D Phantoms for Human Carotid Vasculature. 2013 ,	6
1684	. 2013 ,	1
1683	Worst-Case Local Boundary Precision in Global Measures of Segmentation Reproducibility. 2013 ,	1
1682	Cerebellar atrophy in patients with subcortical-type vascular cognitive impairment. 2013 , 12, 35-42	11

1681	Distinguishing radiation fibrosis from tumour recurrence after stereotactic ablative radiotherapy (SABR) for lung cancer: a quantitative analysis of CT density changes. 2013 , 52, 910-8		40
1680	Aneurysm Intraluminal Thrombus Compressibility Estimated in vivo Using Electrocardiographically Gated Computed Tomography: A Feasibility Study. 2013 , 26, e4-e6		1
1679	Structural integrity of the substantia nigra and subthalamic nucleus predicts flexibility of instrumental learning in older-age individuals. 2013 , 34, 2261-70		33
1678	Assessing hippocampal functional reserve in temporal lobe epilepsy: a multi-voxel pattern analysis of fMRI data. 2013 , 105, 140-9		24
1677	Patient-specific aortic endografting simulation: from diagnosis to prediction. 2013 , 43, 386-94		46
1676	Diffusion MRI of the developing cerebral cortical gray matter can be used to detect abnormalities in tissue microstructure associated with fetal ethanol exposure. <i>NeuroImage</i> , 2013 , 83, 1081-7	7.9	22
1675	Interactive medical image segmentation using PDE control of active contours. 2013 , 32, 2127-39		29
1674	Surface fluid registration of conformal representation: application to detect disease burden and genetic influence on hippocampus. <i>NeuroImage</i> , 2013 , 78, 111-34	7.9	59
1673	Cerebral microbleeds are related to subjective cognitive failures: the RUN DMC study. 2013 , 34, 2225-30		29
1672	3D reconstruction of the lumbar vertebrae from anteroposterior and lateral dual-energy X-ray absorptiometry. 2013 , 17, 475-87		14
1671	Manganese-enhanced magnetic resonance imaging (MEMRI) reveals brain circuitry involved in responding to an acute novel stress in rats with a history of repeated social stress. 2013 , 122, 228-36		23
1670	Discrepancies in determination of abdominal aortic aneurysms maximum diameter and growth rate, using axial and orthogonal computed tomography measurements. 2013 , 82, 1398-403		15
1669	Three-dimensional reconstruction of human vocal folds and standard laryngeal cartilages using computed tomography scan data. 2013 , 27, 769-77		10
1668	Collaborative patch-based super-resolution for diffusion-weighted images. <i>NeuroImage</i> , 2013 , 83, 245-61	7.9	74
1667	Extended-field-of-view three-dimensional transesophageal echocardiography using image-based X-ray probe tracking. 2013 , 39, 993-1005		13
1666	Gamma knife radiosurgery for the treatment of cystic cerebral metastases. 2013 , 85, 667-71		14
1665	3D robust Chan-Vese model for industrial computed tomography volume data segmentation. 2013 , 51, 1235-1244		8
1664	Striatal shape in Parkinson's disease. 2013 , 34, 2510-6		49

1663	Multiparametric brainstem segmentation using a modified multivariate mixture of Gaussians. 2013 , 2, 684-94		48
1662	2D/3D Image Registration using Regression Learning. 2013 , 117, 1095-1106		40
1661	Long-term 3-dimensional stability of mandibular advancement surgery. 2013 , 71, 1588-97		24
1660	PVA Cryogel for Construction of Deformable PET-MR Visible Phantoms. 2013 , 60, 95-102		10
1659	Regional vulnerability in Huntington's disease: fMRI-guided molecular analysis in patients and a mouse model of disease. 2013 , 52, 84-93		15
1658	Automated chest wall line detection for whole-breast segmentation in sagittal breast MR images. 2013 , 40, 042301		55
1657	A Supervised Graph-Cut Deformable Model for Brain MRI Segmentation. 2013 , 237-259		
1656	Breast MR imaging at 3 T with dual-source radiofrequency transmission offers superior B1 homogeneity: an intraindividual comparison with breast MR imaging at 1.5 T. 2013 , 267, 602-8		4
1655	Imaging patients with psychosis and a mouse model establishes a spreading pattern of hippocampal dysfunction and implicates glutamate as a driver. 2013 , 78, 81-93		344
1654	White matter fiber tractography: why we need to move beyond DTI. 2013 , 118, 1367-77		286
1653	Spatial and temporal mapping of the PfEMP1 export pathway in Plasmodium falciparum. 2013 , 15, 1401-18		54
1652	Nanographene oxide-based radioimmunoconstructs for in vivo targeting and SPECT imaging of HER2-positive tumors. 2013 , 34, 1146-54		71
1651	Analysis of 3D soft tissue changes after 1- and 2-jaw orthognathic surgery in mandibular prognathism patients. 2013 , 71, 151-61		45
1650	AdaPT: An adaptive preterm segmentation algorithm for neonatal brain MRI. <i>NeuroImage</i> , 2013 , 65, 97-108		62
1649	Microstructural integrity of the cingulum is related to verbal memory performance in elderly with cerebral small vessel disease: the RUN DMC study. <i>NeuroImage</i> , 2013 , 65, 416-23	7.9	22
1648	Frequency specific spatial interactions in human electrocorticography: V1 alpha oscillations reflect surround suppression. <i>NeuroImage</i> , 2013 , 65, 424-32	7.9	52
1647	A direct morphometric comparison of five labeling protocols for multi-atlas driven automatic segmentation of the hippocampus in Alzheimer's disease. <i>NeuroImage</i> , 2013 , 66, 50-70	7.9	44
1646	Femoral neck cross-sectional geometry and exercise loading. 2013 , 33, 258-66		13

1645	Comparison of cephalic and extracephalic montages for Transcranial Direct Current Stimulation - A numerical study. 2013 ,	1
1644	Volumetric changes of the nose and nasal airway 2 years after tooth-borne and bone-borne surgically assisted rapid maxillary expansion. 2013 , 121, 450-6	32
1643	A novel tool for segmenting 3D medical images based on generalized cylinders and active surfaces. 2013 , 111, 148-65	13
1642	Automated bone segmentation from large field of view 3D MR images of the hip joint. 2013 , 58, 7375-90	50
1641	Acoustic noise reduction in pseudo-continuous arterial spin labeling (pCASL). 2014 , 27, 269-76	1
1640	Characterization of fast and slow diffusion from diffusion-weighted MRI of pediatric Crohn's disease. 2013 , 37, 156-63	31
1639	UNC-Utah NA-MIC DTI framework: Atlas Based Fiber Tract Analysis with Application to a Study of Nicotine Smoking Addiction. 2013 , 8669,	3
1638	A gaussian mixture + demons deformable registration method for cone-beam CT-guided robotic transoral base-of-tongue surgery. 2013 ,	2
1637	CT image feature analysis in distinguishing radiation fibrosis from tumour recurrence after stereotactic ablative radiotherapy (SABR) for lung cancer: a preliminary study. 2013 ,	1
1636	Temporal pattern of cytotoxic edema in the perihematomal region after intracerebral hemorrhage: a serial magnetic resonance imaging study. 2013 , 44, 1144-6	25
1635	Cardiac magnetic resonance-derived anatomy, scar, and dyssynchrony fused with fluoroscopy to guide LV lead placement in cardiac resynchronization therapy: a comparison with acute haemodynamic measures and echocardiographic reverse remodelling. 2013 , 14, 692-9	50
1634	Intratumoral haemorrhage causing an unusual clinical presentation of a vestibular schwannoma. 2013 , 26, 30-4	5
1633	CT colonography: external clinical validation of an algorithm for computer-assisted prone and supine registration. 2013 , 268, 752-60	5
1632	Urinary bladder segmentation in CT urography (CTU) using CLASS. 2013 , 40, 111906	9
1631	Medical Computer Vision. Recognition Techniques and Applications in Medical Imaging. 2013 ,	2
1630	Quality metrics for high order meshes: analysis of the mechanical simulation of the heart beat. 2013 , 32, 130-8	15
1629	Automated cerebral infarct volume measurement in follow-up noncontrast CT scans of patients with acute ischemic stroke. 2013 , 34, 1522-7	67
1628	Intracranial aneurysm neck size overestimation with 3D rotational angiography: the impact on intra-aneurysmal hemodynamics simulated with computational fluid dynamics. 2013 , 34, 121-8	37

1627	Hippocampal abnormalities of glutamate/glutamine, N-acetylaspartate and choline in patients with depression are related to past illness burden. 2013 , 38, 107-16	64
1626	Chronic effects of pulmonary artery stenosis on hemodynamic and structural development of the lungs. 2013 , 304, L17-28	11
1625	High temporal resolution MRI quantification of global cerebral metabolic rate of oxygen consumption in response to apneic challenge. 2013 , 33, 1514-22	43
1624	Medial temporal lobe contributions to short-term memory for faces. 2013 , 142, 1309-22	18
1623	Prenatal cerebral ischemia disrupts MRI-defined cortical microstructure through disturbances in neuronal arborization. 2013 , 5, 168ra7	117
1622	Multi-Atlas Segmentation with Joint Label Fusion. 2013 , 35, 611-23	566
1621	Detection of tumor progression in optic pathway glioma with and without neurofibromatosis type 1. 2013 , 15, 1560-7	19
1620	A statistical multi-vertebrae shape+pose model for segmentation of CT images. 2013 ,	7
1619	Lateral ventricle morphology analysis via mean latitude axis. 2013 , 8672,	12
1618	Diffusion tensor imaging-based characterization of brain neurodevelopment in primates. 2013 , 23, 36-48	39
1617	Infarct Segmentation Challenge on Delayed Enhancement MRI of the Left Ventricle. 2013 , 97-104	2
1616	Human parietofrontal networks related to action observation detected at rest. 2013 , 23, 178-86	12
1615	Pressure-induced densification in GeO ₂ glass: A transmission x-ray microscopy study. 2013 , 103, 261909	22
1614	Evaluation of a semi-automatic segmentation algorithm in 3D intraoperative ultrasound brain angiography. 2013 , 58, 293-302	5
1613	Surgical guides (patient-specific instruments) for pediatric tibial bone sarcoma resection and allograft reconstruction. 2013 , 2013, 787653	71
1612	Novel method of lung area extraction in chest perfusion computed tomography. 2013 , 58, 79-86	1
1611	A multiscale computational approach to estimating axonal damage under inertial loading of the head. 2013 , 30, 102-18	75
1610	Magnetization transfer-based 3D visualization of foot peripheral nerves. 2013 , 37, 1234-7	5

1609	Automatic prostate segmentation in cone-beam computed tomography images using rigid registration. 2013 , 2013, 3993-7	2
1608	Failure mode and effects analysis in designing a virtual reality-based training simulator for bilateral sagittal split osteotomy. 2013 , 9, e1-9	8
1607	Coronary artery segmentation in cardiac angiography images based on a hybrid approach. 2013 ,	1
1606	Electric field characteristics of electroconvulsive therapy with individualized current amplitude: a preclinical study. 2013 , 2013, 3082-5	5
1605	Longitudinal Heschl's gyrus growth during childhood and adolescence in typical development and autism. 2013 , 6, 78-90	24
1604	Validating and improving CT ventilation imaging by correlating with ventilation 4D-PET/CT using ⁶⁸ Ga-labeled nanoparticles. 2014 , 41, 011910	62
1603	. 2013 ,	4
1602	Virtual surgical planning in endoscopic skull base surgery. 2013 , 123, 2935-9	14
1601	Automated MRI segmentation for individualized modeling of current flow in the human head. 2013 , 10, 066004	105
1600	Deformable image registration for cone-beam CT guided transoral robotic base-of-tongue surgery. 2013 , 58, 4951-79	15
1599	Neuroimaging correlates of everyday action in dementia. 2013 , 35, 993-1005	13
1598	Quantification of porcine vocal fold geometry in three dimensions. 2013 ,	
1597	Evaluation of whole-body MR to CT deformable image registration. 2013 , 14, 4163	32
1596	Spacers in the treatment of hip joint infections: numerical analysis of their durability. 2013 , 477, 012002	
1595	Constructing a 4D murine cardiac micro-CT atlas for automated segmentation and phenotyping applications. 2013 ,	3
1594	Aortic Biological Prosthetic Valve for Open-Surgery and Percutaneous Implant: Procedure Simulation and Performance Assessment. 2013 , 131-168	
1593	Assessing the performance of atlas-based prefrontal brain parcellation in an aging cohort. 2013 , 37, 257-64	8
1592	Toward physiologically motivated registration of diagnostic CT and PET/CT of lung volumes. 2013 , 40, 021903	10

1591 Referencing and Registration of Three-Dimensional Images. **2013**, 112-125

1590 aBEAT: a toolbox for consistent analysis of longitudinal adult brain MRI. **2013**, 8, e60344

7

1589 3-dimensional diffusion tensor imaging (DTI) atlas of the rat brain. **2013**, 8, e67334

36

1588 A magnetic resonance image based atlas of the rabbit brain for automatic parcellation. **2013**, 8, e67418

28

1587 Machine learning of hierarchical clustering to segment 2D and 3D images. **2013**, 8, e71715

78

1586 Morphological features of the porcine lacrimal gland and its compatibility for human lacrimal gland xenografting. **2013**, 8, e74046

13

1585 Structural layers of ex vivo rat hippocampus at 7T MRI. **2013**, 8, e76135

6

1584 Brown adipose tissue quantification in human neonates using water-fat separated MRI. **2013**, 8, e77907

55

1583 Enrichment and training improve cognition in rats with cortical malformations. **2013**, 8, e84492

26

1582 Tonotopic organization in the depth of human inferior colliculus. **2013**, 7, 586

20

1581 Fully automated rodent brain MR image processing pipeline on a Midas server: from acquired images to region-based statistics. **2013**, 7, 15

22

1580 Incorrect ICBM-DTI-81 atlas orientation and white matter labels. **2013**, 7, 4

23

1579 Embryonic heart morphogenesis from confocal microscopy imaging and automatic segmentation. **2013**, 2013, 293069

3

1578 Nonrigid 3D medical image registration and fusion based on deformable models. **2013**, 2013, 902470

4

1577 Development of image segmentation methods for intracranial aneurysms. **2013**, 2013, 715325

8

1576 A Manual, Semi-Automated and Automated ROI Study of fMRI Hemodynamic Response in the Caudate Nucleus. **2013**, 2,

1575 Knowledge-guided robust MRI brain extraction for diverse large-scale neuroimaging studies on humans and non-human primates. **2014**, 9, e77810

69

1574 An intra-individual comparison of MRI, [18F]-FET and [18F]-FLT PET in patients with high-grade gliomas. **2014**, 9, e95830

56

1573	Quantifying metabolic heterogeneity in head and neck tumors in real time: 2-DG uptake is highest in hypoxic tumor regions. 2014 , 9, e102452	22
1572	Two-point magnitude MRI for rapid mapping of brown adipose tissue and its application to the R6/2 mouse model of Huntington disease. 2014 , 9, e105556	13
1571	Identifying predictors of early growth response and adverse radiation effects of vestibular schwannomas to radiosurgery. 2014 , 9, e110823	5
1570	A novel region-growing based semi-automatic segmentation protocol for three-dimensional condylar reconstruction using cone beam computed tomography (CBCT). 2014 , 9, e111126	45
1569	Mild cognitive impairment, poor episodic memory, and late-life depression are associated with cerebral cortical thinning and increased white matter hyperintensities. 2014 , 6, 306	44
1568	Injury of the mammillothalamic tract in patients with thalamic hemorrhage. 2014 , 8, 259	8
1567	UNC-Utah NA-MIC framework for DTI fiber tract analysis. 2014 , 7, 51	45
1566	Merging functional and structural properties of the monkey auditory cortex. 2014 , 8, 198	10
1565	. 2014 ,	7
1564	Speckle in ultrasound images: Friend or FOE?. 2014 ,	3
1563	Social competence following pediatric stroke: contributions of brain insult and family environment. 2014 , 9, 471-83	32
1562	COMPUTING VOLUME OF THE HEART'S RIGHT VENTRICLE USING 2D ECHOCARDIOGRAPHY IMAGES. 2014 , 19, 556-567	
1561	Semi-automatic segmentation of preterm neonate ventricle system from 3D ultrasound images. 2014 ,	0
1560	Software pipeline for midsagittal corpus callosum thickness profile processing : automated segmentation, manual editor, thickness profile generator, group-wise statistical comparison and results display. 2014 , 12, 595-614	18
1559	Novel anthropomorphic hip phantom corrects systemic interscanner differences in proximal femoral vBMD. 2014 , 59, 7819-34	9
1558	Changes in talocrural and subtalar joint kinematics of barefoot versus shod forefoot landing. 2014 , 7, 42	4
1557	Automatic hip cartilage segmentation from 3D MR images using arc-weighted graph searching. 2014 , 59, 7245-66	30
1556	Endogenous attention signals evoked by threshold contrast detection in human superior colliculus. 2014 , 34, 892-900	22

1555	Global Ca ²⁺ signaling drives ribbon-independent synaptic transmission at rod bipolar cell synapses. 2014 , 34, 6233-44	24
1554	3D Planning and Treatment Outcomes of Bone Anchored Maxillary Protraction. 2014 , 427-436	
1553	Assessment of regional MR diffusion changes in dementia with Lewy bodies and Alzheimer's disease. 2014 , 26, 627-35	8
1552	Factors affecting subject-specific finite element models of implant-fitted rat bone specimens: critical analysis of a technical protocol. 2014 , 17, 1403-17	6
1551	Stimulation strength and focality of electroconvulsive therapy and magnetic seizure therapy in a realistic head model. 2014 , 2014, 410-3	10
1550	Approximating transcranial magnetic stimulation with electric stimulation in mouse: a simulation study. 2014 , 2014, 6129-32	8
1549	Computational generation of the Purkinje network driven by clinical measurements: the case of pathological propagations. 2014 , 30, 1558-77	19
1548	Geodesic Active Contours with Adaptive Configuration for Cerebral Vessel and Aneurysm Segmentation. 2014 ,	4
1547	Full-body visible human project—female computational phantom and its applications for biomedical electromagnetic modeling. 2014 ,	
1546	Nonstationary Hemodynamics Modelling in a Cerebral Aneurysm of a Blood Vessel. 2014 , 29,	6
1545	Semi-automatic segmentation of vertebral bodies in volumetric MR images using a statistical shape+pose model. 2014 ,	6
1544	Medial temporal lobe resection attenuates superior temporal sulcus response to faces. 2014 , 61, 291-8	10
1543	Internal three-dimensional strains in human intervertebral discs under axial compression quantified noninvasively by magnetic resonance imaging and image registration. 2014 , 136,	16
1542	Minimally invasive multiport surgery of the lateral skull base. 2014 , 2014, 379295	10
1541	Left Atrial Segmentation Challenge: A Unified Benchmarking Framework. 2014 , 1-13	3
1540	Finite element based nonlinear normalization of human lumbar intervertebral disc stiffness to account for its morphology. 2014 , 136, 061003	9
1539	Intraluminal cell transplantation prevents growth and rupture in a model of rupture-prone saccular aneurysms. 2014 , 45, 3684-90	20
1538	Nonlocal intracranial cavity extraction. 2014 , 2014, 820205	35

1537	. 2014 ,	1
1536	Loss of mural cells leads to wall degeneration, aneurysm growth, and eventual rupture in a rat aneurysm model. 2014 , 45, 248-54	63
1535	Comparison of CLASS and ITK-SNAP in segmentation of urinary bladder in CT urography. 2014 ,	
1534	Design and Evaluation of Interactive Proofreading Tools for Connectomics. 2014 , 20, 2466-75	29
1533	An allometric scaling relationship in the brain of preterm infants. 2014 , 1, 933-7	6
1532	Contrast 3D echocardiographic segmentation by image inversion. 2014 ,	
1531	Impact of regional white matter lesions on cognitive function in subcortical vascular cognitive impairment. 2014 , 36, 434-43	14
1530	User-guided segmentation for volumetric retinal optical coherence tomography images. 2014 , 19, 086020	105
1529	Age, kidney function, and risk factors associate differently with cortical and medullary volumes of the kidney. 2014 , 85, 677-85	96
1528	Accuracy of noninvasive, single-plane fluoroscopic analysis for measurement of three-dimensional femorotibial joint poses in dogs treated by tibial plateau leveling osteotomy. 2014 , 75, 486-93	9
1527	An Adaptive Inverse Image Construction Method for Contrast 3D Echocardiography. 2014 ,	
1526	Efficient feature-based 2D/3D registration of transesophageal echocardiography to x-ray fluoroscopy for cardiac interventions. 2014 ,	2
1525	Brain volume estimation from post-mortem newborn and fetal MRI. 2014 , 6, 438-44	16
1524	The relevance of MRI for patient modeling in head and neck hyperthermia treatment planning: a comparison of CT and CT-MRI based tissue segmentation on simulated temperature. 2014 , 41, 123302	21
1523	Understanding embryonic heart morphogenesis through automatic segmentation and confocal imaging with optical clearing. 2014 ,	
1522	A multi-tissue segmentation of the human head for detailed computational models. 2014 , 2014, 2484-7	
1521	Fast level-set based image segmentation using coherent propagation. 2014 , 41, 073501	26
1520	Optimal spatial design of non-invasive magnetic field-based localization systems. 2014 ,	8

1519	Quantitative magnetic resonance imaging analysis of the relationship between contact force and left atrial scar formation after catheter ablation of atrial fibrillation. 2014 , 25, 138-45	59
1518	Volumetric changes in hippocampal subregions and their relation to memory in pediatric nonlesional localization-related epilepsy. 2014 , 55, 519-27	8
1517	A longitudinal comparison of hemodynamics and intraluminal thrombus deposition in abdominal aortic aneurysms. 2014 , 307, H1786-95	58
1516	Postnatal development of the hippocampus in the Rhesus macaque (<i>Macaca mulatta</i>): a longitudinal magnetic resonance imaging study. 2014 , 24, 794-807	21
1515	Augmented real-time navigation with critical structure proximity alerts for endoscopic skull base surgery. 2014 , 124, 853-9	40
1514	Lesion symptom mapping of manipulable object naming in nonfluent aphasia: can a brain be both embodied and disembodied?. 2014 , 31, 287-312	21
1513	Aortic relative pressure components derived from four-dimensional flow cardiovascular magnetic resonance. 2014 , 72, 1162-9	32
1512	CA3 size predicts the precision of memory recall. 2014 , 111, 10720-5	56
1511	Do maternal opioids reduce neonatal regional brain volumes? A pilot study. 2014 , 34, 909-13	47
1510	Atlas-guided volumetric diffuse optical tomography enhanced by generalized linear model analysis to image risk decision-making responses in young adults. 2014 , 35, 4249-66	20
1509	Automated segmentation of the incus and malleus ossicles in conventional tri-dimensional computed tomography images. 2014 , 228, 810-8	4
1508	Fully automated segmentation of cartilage from the MR images of knee using a multi-atlas and local structural analysis method. 2014 , 41, 092303	39
1507	The utility of deformable image registration for small artery visualisation in contrast-enhanced whole body MR angiography. 2014 , 30, 898-908	2
1506	Graft inflow stenosis induced by the inflatable ring fixation mechanism of the Ovation stent-graft system: hemodynamic and clinical implications. 2014 , 21, 829-38	16
1505	Intensity inhomogeneity correction for magnetic resonance imaging of human brain at 7T. 2014 , 41, 022302	23
1504	Medical Computer Vision: Algorithms for Big Data. 2014 ,	3
1503	Rupture-associated changes of cerebral aneurysm geometry: high-resolution 3D imaging before and after rupture. 2014 , 35, 1358-62	44
1502	Modeling transcranial electric stimulation in mouse: a high resolution finite element study. 2014 , 2014, 406-9	8

1501	. 2014 ,	1
1500	2D segmentation of intervertebral discs and its degree of degeneration from T2-weighted magnetic resonance images. 2014 ,	5
1499	A surgical navigation system for non-contact diffuse optical tomography and intraoperative cone-beam CT. 2014 ,	2
1498	Automated registration of optical coherence tomography and dermoscopy in the assessment of sub-clinical spread in basal cell carcinoma. 2014 , 19, 1-12	10
1497	Preclinical evaluation of the engineered stem cell chemokine stromal cell-derived factor 1 analog in a translational ovine myocardial infarction model. 2014 , 114, 650-9	35
1496	Measurement of population receptive fields in human early visual cortex using back-projection tomography. 2014 , 14,	31
1495	Representations of specific acoustic patterns in the auditory cortex and hippocampus. 2014 , 281, 20141000	22
1494	High-resolution magnetic resonance microscopy and diffusion tensor imaging to assess brain structural abnormalities in the murine mucopolysaccharidosis VII model. 2014 , 73, 39-49	10
1493	Optimistic update bias increases in older age. 2014 , 44, 2003-12	42
1492	Encyclopedia of Computational Neuroscience. 2014 , 1-29	1
1491	First experimental results of motion mitigation by continuous line scanning of protons. 2014 , 59, 5707-23	19
1490	Long-term risperidone treatment induces visceral adiposity associated with hepatic steatosis in mice: a magnetic resonance approach. 2014 , 2014, 429291	6
1489	Rapid Automated Target Segmentation and Tracking on 4D Data without Initial Contours. 2014 , 2014, 547075	3
1488	A Longitudinal Low Dose μ CT Analysis of Bone Healing in Mice: A Pilot Study. 2014 , 2014, 791539	1
1487	Computer-Assisted Planning and Patient-Specific Instruments for Bone Tumor Resection within the Pelvis: A Series of 11 Patients. 2014 , 2014, 842709	66
1486	Accuracy of noninvasive, single-plane fluoroscopic analysis for measurement of three-dimensional femorotibial joint poses in dogs. 2014 , 75, 477-85	12
1485	An open-source automated platform for three-dimensional visualization of subdural electrodes using CT-MRI coregistration. 2014 , 55, 2028-2037	20
1484	Myocardium segmentation combining T2 and DE MRI using Multi-Component Bivariate Gaussian mixture model. 2014 ,	2

1483	Common variants in psychiatric risk genes predict brain structure at birth. 2014 , 24, 1230-46		100
1482	A spatio-temporal latent atlas for semi-supervised learning of fetal brain segmentations and morphological age estimation. 2014 , 18, 9-21		36
1481	Waxholm Space atlas of the Sprague Dawley rat brain. <i>NeuroImage</i> , 2014 , 97, 374-86	7.9	190
1480	Microstructural changes in the substantia nigra of asymptomatic agricultural workers. 2014 , 41, 60-4		14
1479	Hybrid structural and texture distinctiveness vector field convolution for region segmentation. 2014 , 125, 85-96		12
1478	Value of volume measurements in evaluating abdominal aortic aneurysms growth rate and need for surgical treatment. 2014 , 83, 1051-1056		17
1477	Patient specific tumor growth prediction using multimodal images. 2014 , 18, 555-66		47
1476	MBIS: multivariate Bayesian image segmentation tool. 2014 , 115, 76-94		3
1475	Human intervertebral disc stiffness correlates better with the Otsu threshold computed from axial T2 map of its posterior annulus fibrosus than with clinical classifications. 2014 , 36, 219-25		10
1474	Interventional radiology virtual simulator for liver biopsy. 2014 , 9, 255-67		22
1473	Corpus callosum shape changes in early Alzheimer's disease: an MRI study using the OASIS brain database. 2014 , 219, 343-52		46
1472	Functional Imaging in Oncology. 2014 ,		1
1471	Injectable and bioresponsive hydrogels for on-demand matrix metalloproteinase inhibition. 2014 , 13, 653-61		346
1470	Segmentation of neonatal brain MR images using patch-driven level sets. <i>NeuroImage</i> , 2014 , 84, 141-58	7.9	136
1469	Quantitative magnetic susceptibility of the developing mouse brain reveals microstructural changes in the white matter. <i>NeuroImage</i> , 2014 , 88, 134-42	7.9	37
1468	Intrinsic Polynomials for Regression on Riemannian Manifolds. 2014 , 50, 32-52		47
1467	EXOSC3 mutations in pontocerebellar hypoplasia type 1: novel mutations and genotype-phenotype correlations. 2014 , 9, 23		60
1466	Evaluation of conventional, dynamic contrast enhanced and diffusion weighted MRI for quantitative Crohn's disease assessment with histopathology of surgical specimens. 2014 , 24, 619-29		142

1465	Population-based studies of myocardial hypertrophy: high resolution cardiovascular magnetic resonance atlases improve statistical power. 2014 , 16, 16	34
1464	IntraVAD, an intra-ventricular assistive device for heart failure patients: design and proof of concept simulations. 2014 , 42, 999-1011	3
1463	Patient-specific analysis of post-operative aortic hemodynamics: a focus on thoracic endovascular repair (TEVAR). 2014 , 54, 943-953	17
1462	Efficient Parallel Transport of Deformations in Time Series of Images: From Schild's to Pole Ladder. 2014 , 50, 5-17	28
1461	In vivo normative atlas of the hippocampal subfields using multi-echo susceptibility imaging at 7 Tesla. 2014 , 35, 3588-601	34
1460	A high-resolution study of hippocampal and medial temporal lobe correlates of spatial context and prospective overlapping route memory. 2014 , 24, 819-39	36
1459	Whole-brain imaging with single-cell resolution using chemical cocktails and computational analysis. 2014 , 157, 726-39	768
1458	A brief guide to synchrotron radiation-based microtomography in (structural) geology and rock mechanics. 2014 , 65, 1-16	77
1457	An intelligent technique for detecting Alzheimer's disease based on brain structural changes and hippocampal shape. 2014 , 2, 121-128	7
1456	Growth patterns of pituitary adenomas and histopathological correlates. 2014 , 99, 1330-8	31
1455	Cardiovascular and Cardiac Therapeutic Devices. 2014 ,	4
1454	Wall shear stress calculations based on 3D cine phase contrast MRI and computational fluid dynamics: a comparison study in healthy carotid arteries. 2014 , 27, 826-34	48
1453	Regional 3D superimposition to assess temporomandibular joint condylar morphology. 2014 , 43, 20130273	41
1452	Application of fused lasso logistic regression to the study of corpus callosum thickness in early Alzheimer's disease. 2014 , 221, 78-84	15
1451	Virtual unrolling and information recovery from scanned scrolled historical documents. 2014 , 47, 248-259	26
1450	Optimization in Cardiovascular Modeling. 2014 , 46, 519-546	54
1449	Multimodal MR imaging model to predict tumor infiltration in patients with gliomas. 2014 , 56, 107-15	21
1448	Hippocampal sclerosis after febrile status epilepticus: the FEBSTAT study. 2014 , 75, 178-85	180

1447	Shape Analysis in Medical Image Analysis. 2014 ,	2
1446	Colour vision impairment is associated with disease severity in multiple sclerosis. 2014 , 20, 1207-16	31
1445	Should we be doing the Norwood procedure sooner?. 2014 , 148, 2188-9	2
1444	Time to surgery and preoperative cerebral hemodynamics predict postoperative white matter injury in neonates with hypoplastic left heart syndrome. 2014 , 148, 2181-8	80
1443	Dysmorphogenic effects of first trimester-equivalent ethanol exposure in mice: a magnetic resonance microscopy-based study. 2014 , 38, 2008-14	27
1442	A Flexible Method for Multi-Material Decomposition of Dual-Energy CT Images. 2014 , 33, 99-116	113
1441	Early prediction of tumor recurrence based on CT texture changes after stereotactic ablative radiotherapy (SABR) for lung cancer. 2014 , 41, 033502	73
1440	Comparison of cephalic and extracephalic montages for transcranial direct current stimulation--a numerical study. 2014 , 61, 2488-98	42
1439	Targeted injection of a biocomposite material alters macrophage and fibroblast phenotype and function following myocardial infarction: relation to left ventricular remodeling. 2014 , 350, 701-9	22
1438	Can cone-beam computed tomography superimposition help orthodontists better understand relapse in surgical patients?. 2014 , 146, 641-54	6
1437	3D blob based brain tumor detection and segmentation in MR images. 2014 ,	10
1436	A patient-specific measurement technique to model shoulder joint kinematics. 2014 , 100, 715-9	27
1435	Patient-specific simulation of a stentless aortic valve implant: the impact of fibres on leaflet performance. 2014 , 17, 277-85	21
1434	CT colonography: clinical evaluation of a method for automatic coregistration of polyps at follow-up surveillance studies. 2014 , 273, 417-24	1
1433	Decreased hippocampal volume and increased anxiety in a transgenic mouse model expressing the human CYP2C19 gene. 2014 , 19, 733-41	38
1432	Impact of head rotation on the individualized common carotid flow and carotid bifurcation hemodynamics. 2014 , 18, 783-9	9
1431	Prediction of periventricular leukomalacia occurrence in neonates after heart surgery. 2014 , 18, 1453-60	11
1430	3D Diagnosis and Management of Facial Asymmetries. 2014 , 453-461	

1429	Motion-defined surface segregation in human visual cortex. 2014 , 26, 2479-89	3
1428	Micro-CT of rodents: state-of-the-art and future perspectives. 2014 , 30, 619-34	121
1427	Pericardial fat volume is associated with clinical recurrence after catheter ablation for persistent atrial fibrillation, but not paroxysmal atrial fibrillation: an analysis of over 600-patients. 2014 , 176, 841-6	39
1426	Prediction of 3-dimensional pharyngeal airway changes after orthognathic surgery: a preliminary study. 2014 , 146, 299-309	43
1425	Patient-specific modeling of ventricular activation pattern using surface ECG-derived vectorcardiogram in bundle branch block. 2014 , 115, 305-13	20
1424	Toward long-term and accurate augmented-reality for monocular endoscopic videos. 2014 , 61, 2609-20	32
1423	Is Breast Asymmetry Present in Girls with Adolescent Idiopathic Scoliosis?. 2014 , 2, 374-379	8
1422	Computational Modeling of Objects Presented in Images. Fundamentals, Methods, and Applications. 2014 ,	1
1421	Segmentation of B-mode cardiac ultrasound data by Bayesian Probability Maps. 2014 , 18, 1184-99	12
1420	Simulation of transcatheter aortic valve implantation through patient-specific finite element analysis: two clinical cases. 2014 , 47, 2547-55	73
1419	mTORC1 inhibition delays growth of neurofibromatosis type 2 schwannoma. 2014 , 16, 493-504	47
1418	Prenatal alcohol exposure reduces magnetic susceptibility contrast and anisotropy in the white matter of mouse brains. <i>NeuroImage</i> , 2014 , 102 Pt 2, 748-55	7.9 25
1417	A spatiotemporal-based scheme for efficient registration-based segmentation of thoracic 4-D MRI. 2014 , 18, 969-77	9
1416	Modeling the Vocal Tract Transfer Function Using a 3D Digital Waveguide Mesh. 2014 , 22, 453-464	10
1415	Automatic quantification of subarachnoid hemorrhage on noncontrast CT. 2014 , 35, 2279-86	35
1414	Influence of gait loads on implant integration in rat tibiae: experimental and numerical analysis. 2014 , 47, 3255-63	8
1413	Automated assessment of renal cortical surface roughness from computerized tomography images and its association with age. 2014 , 21, 1441-5	7
1412	Reproducibility, and age, body-weight and gender dependency of candidate skeletal muscle MRI outcome measures in healthy volunteers. 2014 , 24, 1610-20	49

1411	MRI-based 3D pelvic autonomous innervation: a first step towards image-guided pelvic surgery. 2014 , 24, 1989-97	15
1410	Intra-operative correction of brain-shift. 2014 , 156, 1301-10	53
1409	Visualization and Quantification of Vascular Structure of Fruit Using Magnetic Resonance Microimaging. 2014 , 45, 517-525	8
1408	On simulating sustained isometric muscle fatigue: a phenomenological model considering different fiber metabolisms. 2014 , 13, 1373-85	8
1407	Entropy of T2-weighted imaging combined with apparent diffusion coefficient in prediction of uterine leiomyoma volume response after uterine artery embolization. 2014 , 21, 437-44	15
1406	Hepatocyte cocultures with endothelial cells and fibroblasts on micropatterned fibrous mats to promote liver-specific functions and capillary formation capabilities. 2014 , 15, 1044-54	76
1405	Neuropsychological syndromes associated with Alzheimer's/vascular dementia: a latent class analysis. 2014 , 42, 999-1014	30
1404	Logical circularity in voxel-based analysis: normalization strategy may induce statistical bias. 2014 , 35, 745-59	35
1403	Four-dimensional radiotherapeutic dose calculation using biomechanical respiratory motion description. 2014 , 9, 449-57	9
1402	Characterization of a genetic mouse model of lung cancer: a promise to identify Non-Small Cell Lung Cancer therapeutic targets and biomarkers. 2014 , 15 Suppl 3, S1	17
1401	Focused shape models for hip joint segmentation in 3D magnetic resonance images. 2014 , 18, 567-78	44
1400	Three-dimensional spatiotemporal features for fast content-based retrieval of focal liver lesions. 2014 , 61, 2768-78	31
1399	Prognostic value of CA4/DG volumetry with 3T magnetic resonance imaging on postoperative outcome of epilepsy patients with dentate gyrus pathology. 2014 , 108, 1315-25	14
1398	Computational Methods and Clinical Applications for Spine Imaging. 2014 ,	2
1397	Cortical thinning and caudate abnormalities in first episode psychosis and their association with clinical outcome. 2014 , 159, 36-42	27
1396	Rapid automatic segmentation of the human cerebellum and its lobules (RASCAL)--implementation and application of the patch-based label-fusion technique with a template library to segment the human cerebellum. 2014 , 35, 5026-39	32
1395	Impact of sex and gonadal steroids on neonatal brain structure. 2014 , 24, 2721-31	67
1394	Integration of sparse multi-modality representation and anatomical constraint for isointense infant brain MR image segmentation. <i>NeuroImage</i> , 2014 , 89, 152-64	7.9 80

1393	Robust segmentation methods with an application to aortic pulse wave velocity calculation. 2014 , 38, 179-89		8
1392	Bone marrow fat accumulation accelerated by high fat diet is suppressed by exercise. 2014 , 64, 39-46		109
1391	Real-time magnetic resonance imaging technique for determining left ventricle pressure-volume loops. 2014 , 97, 1597-603		14
1390	Real-time 3D interactive segmentation of echocardiographic data through user-based deformation of B-spline explicit active surfaces. 2014 , 38, 57-67		14
1389	Histology-derived volumetric annotation of the human hippocampal subfields in postmortem MRI. <i>NeuroImage</i> , 2014 , 84, 505-23	7.9	97
1388	Comparison of miR-124-3p and miR-16 for early diagnosis of hemorrhagic and ischemic stroke. 2014 , 433, 139-44		51
1387	Fully automatic segmentation of the mitral leaflets in 3D transesophageal echocardiographic images using multi-atlas joint label fusion and deformable medial modeling. 2014 , 18, 118-29		58
1386	Characteristics of magnetic resonance imaging biomarkers in a natural history study of golden retriever muscular dystrophy. 2014 , 24, 178-91		41
1385	Human L3/L4 intervertebral disc mean 3D shape, modes of variation, and their relationship to degeneration. 2014 , 47, 2452-9		37
1384	Risk factors for preoperative periventricular leukomalacia in term neonates with hypoplastic left heart syndrome are patient related. 2014 , 147, 1312-8		40
1383	Treatment planning and image guidance for radiofrequency ablation of large tumors. 2014 , 18, 920-8		29
1382	Nonrigid registration of volumetric images using ranked order statistics. 2014 , 33, 422-32		4
1381	Continuous wave simulations on the propagation of electromagnetic fields through the human head. 2014 , 61, 1676-83		16
1380	Accuracy of abdominal ultrasound and MRI for detection of Crohn disease and ulcerative colitis in children. 2014 , 44, 1370-8		27
1379	Deformable Models in Medical Image Segmentation. 2014 , 81-106		10
1378	Universal fractional noncubic power law for density of metallic glasses. 2014 , 112, 185502		56
1377	Image guidance for all--TilePro display of 3-dimensionally reconstructed images in robotic partial nephrectomy. 2014 , 84, 237-42		31
1376	Robust, accurate and fast automatic segmentation of the spinal cord. <i>NeuroImage</i> , 2014 , 98, 528-36	7.9	103

1375	Biomechanical modeling to prevent ischial pressure ulcers. 2014 , 47, 2231-6	29
1374	Track L: miscellaneous. 2014 , 59 Suppl 1, s758-909	10
1373	Ex vivo micro-CT imaging of murine brain models using non-ionic iodinated contrast. 2014 ,	
1372	A comprehensive protocol for manual segmentation of the medial temporal lobe structures. 2014 ,	12
1371	Metastatic brain cancer: prediction of response to whole-brain helical tomotherapy with simultaneous intralesional boost for metastatic disease using quantitative MR imaging features. 2014 ,	
1370	Three-dimensional kinematics of the talocrural and subtalar joints during drop landing. 2014 , 30, 160-5	11
1369	Estimating intracranial volume using intracranial area in healthy children and those with childhood status epilepticus. 2014 , 4, 936-42	6
1368	Associations between tumor vascularization assessed by in vivo DCE-MRI and the presence of disseminated tumor cells in bone marrow in breast cancer patients at the time of diagnosis. 2014 , 40, 1382-91	8
1367	Cellular imaging and texture analysis distinguish differences in cellular dynamics in mouse brain tumors. 2014 , 71, 1531-41	5
1366	Microstructural origins of gadolinium-enhanced susceptibility contrast and anisotropy. 2014 , 72, 1702-11	16
1365	Early prediction of lung cancer recurrence after stereotactic radiotherapy using second order texture statistics. 2014 ,	1
1364	Inattentive blindness increased with augmented reality surgical navigation. 2014 , 28, 433-7	37
1363	Quantification of the fat fraction in the liver using dual-energy computed tomography and multicomponent decomposition. 2014 , 38, 845-52	29
1362	Patient-specific left atrial wall-thickness measurement and visualization for radiofrequency ablation. 2014 ,	2
1361	MRI-based pseudo-CT generation using sorted atlas images in whole-body PET/MRI. 2014 ,	3
1360	Image to physical space registration of supine breast MRI for image guided breast surgery. 2014 ,	5
1359	Prerequisite of SPECT/CT image segmentation approach potentially leading to precise absolute quantification of myocardial focal tracer uptake: Phantom and canine validations. 2014 ,	0
1358	Posterior structural brain volumes differ in maltreated youth with and without chronic posttraumatic stress disorder. 2015 , 27, 1555-76	43

1357	A bi-ventricular cardiac atlas built from 1000+ high resolution MR images of healthy subjects and an analysis of shape and motion. 2015 , 26, 133-45	84
1356	Viscous dissipation energy as a risk factor in multiple cerebral aneurysms. 2015 , 30,	8
1355	Real-time tracking of deformable target in 3D ultrasound images. 2015 ,	2
1354	Liver Tumor Segmentation Using SVM Framework and Pathology Characterization Using Content-Based Image Retrieval. 2015 , 325-360	2
1353	A hybrid approach for fusing 4D-MRI temporal information with 3D-CT for the study of lung and lung tumor motion. 2015 , 42, 4484-96	18
1352	Magnetization transfer imaging of suicidal patients with major depressive disorder. 2015 , 5, 9670	28
1351	Coupling treatment planning with navigation system: a new technological approach in treatment of head and neck tumors by electrochemotherapy. 2015 , 14 Suppl 3, S2	45
1350	Improved dosimetry for targeted radionuclide therapy using nonrigid registration on sequential SPECT images. 2015 , 42, 1060-70	10
1349	The pediatric template of brain perfusion. 2015 , 2, 150003	40
1348	Estimation of the number of alveolar capillaries by the Euler number (Euler-Poincaré characteristic). 2015 , 309, L1286-93	20
1347	Utiliza� de programas de p�-processamento de imagens tomogr�ficas na avalia� da articula� temporomandibular: descri� de t�cnica. 2015 , 56, 262-267	
1346	Identification of the optic recess region as a morphogenetic entity in the zebrafish forebrain. 2015 , 5, 8738	31
1345	. 2015 ,	5
1344	Magnetic susceptibility anisotropy of myocardium imaged by cardiovascular magnetic resonance reflects the anisotropy of myocardial filament helix polypeptide bonds. 2015 , 17, 60	29
1343	Stereological study of pyramidal neurons in the human superior temporal gyrus from childhood to adulthood. 2015 , 523, 1054-72	9
1342	Patient-specific anisotropic model of human trunk based on MR data. 2015 , 31, e02724	
1341	Intraoperative image-guided transoral robotic surgery: pre-clinical studies. 2015 , 11, 256-67	15
1340	Automated fiducial point selection for reducing registration error in the co-localisation of left atrium electroanatomic and imaging data. 2015 , 2015, 1989-92	5

1339	Analysis of in vivo single cell behavior by high throughput, human-in-the-loop segmentation of three-dimensional images. 2015 , 16, 397	8
1338	Respiratory motion correction of PET using MR-constrained PET-PET registration. 2015 , 14, 85	10
1337	Rapid automatic segmentation of abnormal tissue in late gadolinium enhancement cardiovascular magnetic resonance images for improved management of long-standing persistent atrial fibrillation. 2015 , 14, 88	9
1336	User-initialized active contour segmentation and golden-angle real-time cardiovascular magnetic resonance enable accurate assessment of LV function in patients with sinus rhythm and arrhythmias. 2015 , 17, 37	14
1335	Single breath-hold 3D measurement of left atrial volume using compressed sensing cardiovascular magnetic resonance and a non-model-based reconstruction approach. 2015 , 17, 47	15
1334	Biomass accessibility analysis using electron tomography. 2015 , 8, 212	11
1333	Two Realistic Beagle Models for Dose Assessment. 2015 , 109, 198-204	4
1332	A Surrogate Measure of Cortical Bone Matrix Density by Long T2 -Suppressed MRI. 2015 , 30, 2229-38	11
1331	Volumetric arterial wall shear stress calculation based on cine phase contrast MRI. 2015 , 41, 505-16	104
1330	Interactive segmentation and visualization system for medical images on mobile devices. 2015 , 2, 96-107	3
1329	Revisiting diagenesis on the Ontong Java Plateau: Evidence for authigenic crust precipitation in Globorotalia tumida. 2015 , 30, 1490-1502	12
1328	White Matter and Hippocampal Volume Predict the Risk of Dementia in Patients with Cerebral Small Vessel Disease: The RUN DMC Study. 2016 , 49, 863-73	31
1327	Successful Scene Encoding in Presymptomatic Early-Onset Alzheimer's Disease. 2015 , 47, 955-64	5
1326	Post-exercise cold water immersion attenuates acute anabolic signalling and long-term adaptations in muscle to strength training. 2015 , 593, 4285-301	115
1325	The orbital volume measurement in patients with ventriculoperitoneal shunt. 2015 , 26, 255-8	5
1324	Influence of Intracranial Electrode Density and Spatial Configuration on Interictal Spike Localization: A Case Study. 2015 , 32, e30-40	1
1323	Bi-component T2 * analysis of bound and pore bone water fractions fails at high field strengths. 2015 , 28, 861-72	30
1322	Simultaneous Estimation of Elasticity for Multiple Deformable Bodies. 2015 , 26, 197-206	1

1321	Cd11b(+) myeloid cells support hepatic metastasis through down-regulation of angiopoietin-like 7 in cancer cells. 2015 , 62, 521-33	33
1320	Normative biometrics for fetal ocular growth using volumetric MRI reconstruction. 2015 , 35, 400-8	13
1319	Automatic iceball segmentation with adapted shape priors for MRI-guided cryoablation. 2015 , 41, 517-24	6
1318	The effects of anatomic variations on stereotactic laser amygdalohippocampectomy and a proposed protocol for trajectory planning. 2015 , 11 Suppl 2, 345-56; discussion 356-7	23
1317	A Comparison of Different Methods to Generate Tooth Surface Models Without Applying Ionizing Radiation for Digital 3-Dimensional Image Fusion With Magnetic Resonance Imaging-Based Data of the Head and Neck Region. 2015 , 39, 882-9	6
1316	Diffusion kurtosis imaging can efficiently assess the glioma grade and cellular proliferation. 2015 , 6, 42380-93	83
1315	Dissociating Statistically-Determined Alzheimer's Disease/Vascular Dementia Neuropsychological Syndromes Using White and Gray Neuroradiological Parameters. 2015 , 48, 833-47	9
1314	Semi-Automatic Image Labelling Using Depth Information. 2015 , 4, 142-154	3
1313	Hippocampal subfield and medial temporal cortical persistent activity during working memory reflects ongoing encoding. 2015 , 9, 30	17
1312	Default mode network, motor network, dorsal and ventral basal ganglia networks in the rat brain: comparison to human networks using resting state-fMRI. 2015 , 10, e0120345	42
1311	Evaluating the accuracy of diffusion MRI models in white matter. 2015 , 10, e0123272	42
1310	Fully automated whole-head segmentation with improved smoothness and continuity, with theory reviewed. 2015 , 10, e0125477	30
1309	In vivo high angular resolution diffusion-weighted imaging of mouse brain at 16.4 Tesla. 2015 , 10, e0130133	20
1308	In Vivo Detection of Perinatal Brain Metabolite Changes in a Rabbit Model of Intrauterine Growth Restriction (IUGR). 2015 , 10, e0131310	14
1307	Temporal Lobe and Frontal-Subcortical Dissociations in Non-Demented Parkinson's Disease with Verbal Memory Impairment. 2015 , 10, e0133792	16
1306	Improved Framework for Tractography Reconstruction of the Optic Radiation. 2015 , 10, e0137064	24
1305	Three-Dimensional Histology Volume Reconstruction of Axonal Tract Tracing Data: Exploring Topographical Organization in Subcortical Projections from Rat Barrel Cortex. 2015 , 10, e0137571	6
1304	Does Long-Term High Fat Diet Always Lead to Smaller Hippocampi Volumes, Metabolite Concentrations, and Worse Learning and Memory? A Magnetic Resonance and Behavioral Study in Wistar Rats. 2015 , 10, e0139987	11

1303	Lateral pterygoid muscle volume and migraine in patients with temporomandibular disorders. 2015 , 45, 1-5	25
1302	Molecular magnetic resonance imaging of angiogenesis in vivo using polyvalent cyclic RGD-iron oxide microparticle conjugates. 2015 , 5, 515-29	48
1301	Automated Delineation of Vessel Wall and Thrombus Boundaries of Abdominal Aortic Aneurysms Using Multispectral MR Images. 2015 , 2015, 202539	1
1300	MRI segmentation of the human brain: challenges, methods, and applications. 2015 , 2015, 450341	285
1299	Computer-aided assessment of tumor grade for breast cancer in ultrasound images. 2015 , 2015, 914091	5
1298	Implantation of 3D-Printed Patient-Specific Aneurysm Models into Cadaveric Specimens: A New Training Paradigm to Allow for Improvements in Cerebrovascular Surgery and Research. 2015 , 2015, 939387	26
1297	Automated Segmentation of Cerebellum Using Brain Mask and Partial Volume Estimation Map. 2015 , 2015, 167489	6
1296	Automatic segmentation of colon in 3D CT images and removal of opacified fluid using cascade feed forward neural network. 2015 , 2015, 670739	10
1295	Method for 3D airway topology extraction. 2015 , 2015, 127010	3
1294	Creating 3D visualizations of MRI data: A brief guide. 2015 , 4, 466	34
1293	Hippocampal morphology in a rat model of depression: the effects of physical activity. 2014 , 9, 1-6	15
1292	Corpus callosum area in patients with bipolar disorder with and without psychotic features: an international multicentre study. 2015 , 40, 352-9	44
1291	Obesity Correlates With Glomerulomegaly But Is Not Associated With Kidney Dysfunction Early After Donation. 2015 , 1, 1-6	9
1290	Electric Field Model of Transcranial Electric Stimulation in Nonhuman Primates: Correspondence to Individual Motor Threshold. 2015 , 62, 2095-105	22
1289	Emission-based estimation of lung attenuation coefficients for attenuation correction in time-of-flight PET/MR. 2015 , 60, 4813-33	26
1288	Corpus callosum area and brain volume in autism spectrum disorder: quantitative analysis of structural MRI from the ABIDE database. 2015 , 45, 3107-14	26
1287	Bayesian Statistics from Methods to Models and Applications. 2015 ,	
1286	Dosimetry of a (90)Y-hydroxide liquid brachytherapy treatment approach to canine osteosarcoma using PET/CT. 2015 , 97, 193-200	1

1285	How Does the Accuracy of Intracranial Volume Measurements Affect Normalized Brain Volumes? Sample Size Estimates Based on 966 Subjects from the HUNT MRI Cohort. 2015 , 36, 1450-6	57
1284	Cytoarchitectonic mapping of the human brain cerebellar nuclei in stereotaxic space and delineation of their co-activation patterns. 2015 , 9, 54	26
1283	Fast three-dimensional superimposition of cone beam computed tomography for orthopaedics and orthognathic surgery evaluation. 2015 , 44, 1188-96	58
1282	The effect of head rotation on the geometry and hemodynamics of healthy vertebral arteries. 2015 , 43, 1287-97	12
1281	Volume and shape analysis of subcortical brain structures and ventricles in euthymic bipolar I disorder. 2015 , 233, 324-30	24
1280	Thalamic volume as a biomarker for disorders of consciousness. 2015 ,	3
1279	Texture analysis of automatic graph cuts segmentations for detection of lung cancer recurrence after stereotactic radiotherapy. 2015 ,	1
1278	Fetal MRI detects early alterations of brain development in Tetralogy of Fallot. 2015 , 213, 392.e1-7	47
1277	Influence of left atrial geometry on rotor core trajectories in a model of atrial fibrillation. 2015 ,	2
1276	3D/2D image registration using weighted histogram of gradient directions. 2015 ,	3
1275	Minimum slice spacing required to reconstruct 3D shape for serial sections of breast tissue for comparison with medical imaging. 2015 ,	2
1274	Parametric ultrasound and fluoroscopy image fusion for guidance of left ventricle lead placement in cardiac resynchronization therapy. 2015 , 2, 025001	3
1273	Evaluating MRI based vascular wall motion as a biomarker of Fontan hemodynamic performance. 2015 ,	
1272	Investigating the geometry of pig airways using computed tomography. 2015 ,	1
1271	Validation of Osteoarthritis synthetic defect database via non-rigid registration. 2015 , 9417,	0
1270	A technique for visualising three-dimensional left atrial cardiac activation data in two dimensions with minimal distance distortion. 2015 , 2015, 7296-9	8
1269	Personalized mathematical modeling of cerebral arterial aneurysms. 2015 ,	
1268	High-Pressure Transvenous Perfusion of the Upper Extremity in Human Muscular Dystrophy: A Safety Study with 0.9% Saline. 2015 , 26, 614-21	13

1267	A superpixel-based framework for automatic tumor segmentation on breast DCE-MRI. 2015,	4
1266	Minimally invasive cone beam CT-guided evacuation of parenchymal and ventricular hemorrhage using the Apollo system: proof of concept in a cadaver model. 2015, 7, 569-73	13
1265	Costello syndrome: Analysis of the posterior cranial fossa in children with posterior fossa crowding. 2015, 28, 254-8	8
1264	There and Back Again: Hippocampus and Retrosplenial Cortex Track Homing Distance during Human Path Integration. 2015, 35, 15442-52	66
1263	Spatial distribution of adipose compartments size, shape and orientation in a CT breast image of a mastectomy specimen. 2015,	3
1262	Variability and accuracy of different software packages for dynamic susceptibility contrast magnetic resonance imaging for distinguishing glioblastoma progression from pseudoprogression. 2015, 2, 026001	17
1261	The car washing control method using 3D contour segmentation. 2015,	
1260	Automatic classification framework for ventricular septal defects: a pilot study on high-throughput mouse embryo cardiac phenotyping. 2015, 2, 041003	2
1259	Influence of the flow rate on dissolution and precipitation features during percolation of CO ₂ -rich sulfate solutions through fractured limestone samples. 2015, 414, 95-108	56
1258	Characterising the grey matter correlates of leukoaraiosis in cerebral small vessel disease. 2015, 9, 194-205	51
1257	Mooney-Rivlin biomechanical modeling of lung with Inhomogeneous material. 2015, 2015, 7897-900	5
1256	Medially constrained deformable modeling for segmentation of branching medial structures: Application to aortic valve segmentation and morphometry. 2015, 26, 217-31	21
1255	Matching of postcontraction perfusion to oxygen consumption across submaximal contraction intensities in exercising humans. 2015, 119, 280-9	5
1254	Imaging texture analysis for automated prediction of lung cancer recurrence after stereotactic radiotherapy. 2015, 2, 041010	19
1253	Investigating the functions of subregions within anterior hippocampus. 2015, 73, 240-56	61
1252	Spatial and spatio-temporal feature extraction from 4D echocardiography images. 2015, 64, 138-47	3
1251	Automated generation of directed graphs from vascular segmentations. 2015, 56, 395-405	5
1250	A robust comparison approach of velocity data between MRI and CFD based on divergence-free space projection. 2015,	1

1249	Simulation of Transcatheter Aortic Valve Replacement in patient-specific aortic roots: Effect of crimping and positioning on device performance. 2015 , 2015, 282-5	8
1248	Multiscale Modeling of Cardiovascular Flows for Clinical Decision Support. 2015 , 67,	52
1247	A hierarchical model for automated breast lesion detection from ultrasound 3D data. 2015 , 2015, 145-8	
1246	Patch-Based Techniques in Medical Imaging. 2015 ,	4
1245	A 3D sparse motion field filtering for quantitative analysis of fascial layers mobility based on 3D ultrasound scans. 2015 , 2015, 775-80	1
1244	The influence of intraluminal thrombus on noninvasive abdominal aortic aneurysm wall distensibility measurement. 2015 , 53, 299-308	10
1243	The role of automatic computer-aided surgical trajectory planning in improving the expected safety of stereotactic neurosurgery. 2015 , 10, 1127-40	12
1242	Comparison of explicit finite element and mechanical simulation of the proximal femur during dynamic drop-tower testing. 2015 , 48, 224-32	28
1241	A clinically applicable stochastic approach for noninvasive estimation of aortic stiffness using computed tomography data. 2015 , 62, 176-87	13
1240	3-dimensional analysis of regenerative endodontic treatment outcome. 2015 , 41, 317-24	45
1239	Quantitative Monitoring of Bone Formation in Ankylosing Spondylitis Using Computed Tomography. 2015 , 131-158	
1238	Magnetic resonance imaging and histology correlation in the neocortex in temporal lobe epilepsy. 2015 , 77, 237-50	21
1237	Automatic bone segmentation and bone-cartilage interface extraction for the shoulder joint from magnetic resonance images. 2015 , 60, 1441-59	15
1236	Neurophysiological correlates of dysregulated emotional arousal in severe traumatic brain injury. 2015 , 126, 314-24	12
1235	Benchmark for Algorithms Segmenting the Left Atrium From 3D CT and MRI Datasets. 2015 , 34, 1460-1473	96
1234	Pharmacokinetic Tumor Heterogeneity as a Prognostic Biomarker for Classifying Breast Cancer Recurrence Risk. 2015 , 62, 1585-94	34
1233	VIDA: a voxel-based dosimetry method for targeted radionuclide therapy using Geant4. 2015 , 30, 16-26	34
1232	Impact of Early and Late Visual Deprivation on the Structure of the Corpus Callosum: A Study Combining Thickness Profile with Surface Tensor-Based Morphometry. 2015 , 13, 321-336	14

1231	Predictors of longitudinal outcome and recovery of pragmatic language and its relation to externalizing behaviour after pediatric traumatic brain injury. 2015 , 142, 86-95			27
1230	Injectable microsphere gel progressively improves global ventricular function, regional contractile strain, and mitral regurgitation after myocardial infarction. 2015 , 99, 597-603			9
1229	Functional mapping of face-selective regions in the extrastriate visual cortex of the marmoset. 2015 , 35, 1160-72			100
1228	Navigated pelvic osteotomy and tumor resection: a study assessing the accuracy and reproducibility of resection planes in Sawbones and cadavers. 2015 , 97, 40-6			45
1227	Localized intraoperative virtual endoscopy (LIVE) for surgical guidance in 16 skull base patients. 2015 , 152, 165-71			12
1226	A pilot evaluation of a 4-dimensional cone-beam computed tomographic scheme based on simultaneous motion estimation and image reconstruction. 2015 , 91, 410-8			15
1225	Distinct midbrain and habenula pathways are involved in processing aversive events in humans. 2015 , 35, 198-208			75
1224	LINKS: learning-based multi-source Integration framework for Segmentation of infant brain images. <i>NeuroImage</i> , 2015 , 108, 160-72	7.9		168
1223	Deep convolutional neural networks for multi-modality isointense infant brain image segmentation. <i>NeuroImage</i> , 2015 , 108, 214-24	7.9		519
1222	User-guided segmentation of preterm neonate ventricular system from 3-D ultrasound images using convex optimization. 2015 , 41, 542-56			21
1221	Regulatory T cells are not a strong predictor of survival for patients with glioblastoma. 2015 , 17, 801-9			34
1220	Efficient Lattice Boltzmann Solver for Patient-Specific Radiofrequency Ablation of Hepatic Tumors. 2015 , 34, 1576-1589			29
1219	Delineation of hippocampal subregions using T1-weighted magnetic resonance images at 3 Tesla. 2015 , 220, 3259-72			24
1218	Clinical assessment of MR-guided 3-class and 4-class attenuation correction in PET/MR. 2015 , 17, 264-76			42
1217	Assessment of Volume and Height of the Coronoid Process in Patients With Different Facial Types and Skeletal Classes: A Cone-Beam Computed Tomography Study. 2015 , 73, 1395.e1-5			8
1216	Proof of principle: Transformation approach alters caudate nucleus volume and structure-function associations. 2015 , 9, 744-53			7
1215	Encephalization and diversification of the cranial base in platyrrhine primates. 2015 , 81, 29-40			15
1214	Injectable Colloidal Gold for Use in Intrafractional 2D Image-Guided Radiation Therapy. 2015 , 4, 856-63			26

1213	Impact of time-of-flight PET on quantification errors in MR imaging-based attenuation correction. 2015 , 56, 635-41	77
1212	NABS: non-local automatic brain hemisphere segmentation. 2015 , 33, 474-84	20
1211	Expression of progerin in aging mouse brains reveals structural nuclear abnormalities without detectable significant alterations in gene expression, hippocampal stem cells or behavior. 2015 , 24, 1305-21	26
1210	Image Analysis. 2015 ,	1
1209	Automatic SWI Venography Segmentation Using Conditional Random Fields. 2015 , 34, 2478-91	11
1208	Multiatlas whole heart segmentation of CT data using conditional entropy for atlas ranking and selection. 2015 , 42, 3822-33	53
1207	T1 Relaxation Rate (R1) Indicates Nonlinear Mn Accumulation in Brain Tissue of Welders With Low-Level Exposure. 2015 , 146, 281-9	32
1206	Structural and diffusion weighted MRI registration for biomarker fusion in Crohn's disease diagnosis. 2015 ,	0
1205	Automatic segmentation of occluded vasculature via pulsatile motion analysis in endoscopic robot-assisted partial nephrectomy video. 2015 , 25, 103-10	16
1204	Adaptive image inversion of contrast 3D echocardiography for enabling automated analysis. 2015 , 63, 99-107	1
1203	Effect of intraluminal thrombus asymmetrical deposition on abdominal aortic aneurysm growth rate. 2015 , 22, 406-12	19
1202	Assessment of MRI-Based Automated Fetal Cerebral Cortical Folding Measures in Prediction of Gestational Age in the Third Trimester. 2015 , 36, 1369-74	14
1201	In vivo 3-dimensional analysis of scapular and glenohumeral kinematics: comparison of symptomatic or asymptomatic shoulders with rotator cuff tears and healthy shoulders. 2015 , 24, 1817-26	47
1200	3D MR ventricle segmentation in pre-term infants with post-hemorrhagic ventricle dilatation (PHVD) using multi-phase geodesic level-sets. <i>NeuroImage</i> , 2015 , 118, 13-25	7.9 16
1199	Orientation anisotropies in human primary visual cortex depend on contrast. <i>NeuroImage</i> , 2015 , 119, 129-45	7.9 24
1198	Development of a Spinal Fusion Cage by Multiscale Modelling: Application to the Human Cervical Spine. 2015 , 110, 183-190	2
1197	Structural mouthpart interaction evolved already in the earliest lineages of insects. 2015 , 282, 20151033	11
1196	Defining the ischemic penumbra using magnetic resonance oxygen metabolic index. 2015 , 46, 982-8	39

1195	Waxholm Space atlas of the rat brain hippocampal region: three-dimensional delineations based on magnetic resonance and diffusion tensor imaging. <i>NeuroImage</i> , 2015 , 108, 441-9	7.9	55
1194	High-field magnetic resonance imaging of the human temporal lobe. 2015 , 9, 58-68		15
1193	Computer-Aided Prostate Cancer Detection Using Ultrasound RF Time Series: In Vivo Feasibility Study. 2015 , 34, 2248-57		29
1192	The role of the posterior fossa in developing Chiari I malformation in children with craniosynostosis syndromes. 2015 , 43, 813-9		21
1191	Interpreting support vector machine models for multivariate group wise analysis in neuroimaging. 2015 , 24, 190-204		35
1190	Functional MRI of visual responses in the awake, behaving marmoset. <i>NeuroImage</i> , 2015 , 120, 1-11	7.9	47
1189	Visualization and Processing of Higher Order Descriptors for Multi-Valued Data. 2015 ,		4
1188	Personalized Anatomical Meshing of the Human Body with Applications. 2015 , 221-236		2
1187	Realization of a biomechanical model-assisted image guidance system for breast cancer surgery using supine MRI. 2015 , 10, 1985-96		16
1186	A Comprehensive Atlas of the Adult Mouse Penis. 2015 , 9, 162-72		34
1185	Patient-specific anatomical models in human physiology. 2015 , 30,		14
1184	Effect of anticoagulant treatment in deep vein thrombosis: A patient-specific computational fluid dynamics study. 2015 , 48, 2047-53		9
1183	Synthesis of intensity gradient and texture information for efficient three-dimensional segmentation of medical volumes. 2015 , 2, 024003		1
1182	Multi-atlas segmentation of biomedical images: A survey. 2015 , 24, 205-219		402
1181	Age estimation based on pulp chamber volume of first molars from cone-beam computed tomography images. 2015 , 253, 133.e1-7		50
1180	Accurate Vessel Segmentation with Progressive Contrast Enhancement and Canny Refinement. 2015 , 1-16		3
1179	Deep learning for automatic localization, identification, and segmentation of vertebral bodies in volumetric MR images. 2015 ,		11
1178	Computing Brain Change over Time. 2015 , 417-428		1

1177	Finite element analysis predicts experimental failure patterns in vertebral bodies loaded via intervertebral discs up to large deformation. 2015 , 37, 599-604	18
1176	Aortic blood pressure measured via EIT: investigation of different measurement settings. 2015 , 36, 1147-59	10
1175	Computational Models for Predicting Outcomes of Neuroprosthesis Implantation: the Case of Cochlear Implants. 2015 , 52, 934-41	15
1174	The direct incorporation of perfusion defect information to define ischemia and infarction in a finite element model of the left ventricle. 2015 , 137, 051004	5
1173	A new algorithm to diagnose atrial ectopic origin from multi lead ECG systems--insights from 3D virtual human atria and torso. 2015 , 11, e1004026	11
1172	Fracture bone healing and biodegradation of AZ31 implant in rats. 2015 , 10, 025008	16
1171	Evaluating the impact of a Canadian national anatomy and radiology contouring boot camp for radiation oncology residents. 2015 , 91, 701-7	21
1170	Reduced thalamic volume in preterm infants is associated with abnormal white matter metabolism independent of injury. 2015 , 57, 515-25	9
1169	Clinical Assessment of Emission- and Segmentation-Based MR-Guided Attenuation Correction in Whole-Body Time-of-Flight PET/MR Imaging. 2015 , 56, 877-83	28
1168	Transcranial direct current stimulation (tDCS) of frontal cortex decreases performance on the WAIS-IV intelligence test. 2015 , 290, 32-44	45
1167	Precision of robotic guided instrumentation for acetabular component positioning. 2015 , 30, 392-7	53
1166	Automated CT-based segmentation and quantification of total intracranial volume. 2015 , 25, 3151-60	14
1165	Comparison of semi-automated scar quantification techniques using high-resolution, 3-dimensional late-gadolinium-enhancement magnetic resonance imaging. 2015 , 31, 349-57	18
1164	Morphometry-based measurements of the structural response to whole-brain radiation. 2015 , 10, 393-401	10
1163	Remapping of digital subtraction angiography on a standard fluoroscopy system using 2D-3D registration. 2015 ,	
1162	The evaluation of multi-structure, multi-atlas pelvic anatomy features in a prostate MR lymphography CAD system. 2015 ,	2
1161	Segmentation methods for breast vasculature in dual-energy contrast-enhanced digital breast tomosynthesis. 2015 ,	
1160	Real-time 2D spatially selective MRI experiments: Comparative analysis of optimal control design methods. 2015 , 254, 110-20	12

1159	Modeling the Heart and the Circulatory System. 2015,	5
1158	Delay Period Activity of the Substantia Nigra during Proactive Control of Response Selection as Determined by a Novel fMRI Localization Method. 2015, 27, 1238-48	3
1157	Tumor growth prediction with reaction-diffusion and hyperelastic biomechanical model by physiological data fusion. 2015, 25, 72-85	24
1156	Juvenile Swine Surgical Alveolar Cleft Model to Test Novel Autologous Stem Cell Therapies. 2015, 21, 898-908	17
1155	Isotropic reconstruction of a 4-D MRI thoracic sequence using super-resolution. 2015, 73, 784-93	22
1154	Introduction of an automated user-independent quantitative volumetric magnetic resonance imaging breast density measurement system using the Dixon sequence: comparison with mammographic breast density assessment. 2015, 50, 73-80	26
1153	Assessment of DICOM Viewers Capable of Loading Patient-specific 3D Models Obtained by Different Segmentation Platforms in the Operating Room. 2015, 28, 518-27	14
1152	A semiautomatic method for in vivo three-dimensional quantitative analysis of fascial layers mobility based on 3D ultrasound scans. 2015, 10, 1721-35	8
1151	Creation of a 3D printed temporal bone model from clinical CT data. 2015, 36, 619-24	48
1150	Specific wiring of distinct amacrine cells in the directionally selective retinal circuit permits independent coding of direction and size. 2015, 86, 276-91	50
1149	Age and sex effects on corpus callosum morphology across the lifespan. 2015, 36, 2691-702	29
1148	Surgical widening of a stress fracture decreases local strains sufficiently to enable healing in a computational model. 2015, 2, 12-21	2
1147	Immediate cerebral metabolic changes induced by discontinuation of deep brain stimulation of subcallosal cingulate gyrus in treatment-resistant depression. 2015, 173, 159-62	17
1146	A framework for automated contour quality assurance in radiation therapy including adaptive techniques. 2015, 60, 5199-209	24
1145	Patient-specific dose calculations for pediatric CT of the chest, abdomen and pelvis. 2015, 45, 1771-80	13
1144	Increased hippocampal volumes in adults with high functioning autism spectrum disorder and an IQ>100: A manual morphometric study. 2015, 234, 152-5	10
1143	Augmented reality and cone beam CT guidance for transoral robotic surgery. 2015, 9, 223-33	21
1142	Quantification of experimental venous thrombus resolution by longitudinal nanogold-enhanced micro-computed tomography. 2015, 136, 1285-90	8

1141	Microdosimetric and Biological Effects of Photon Irradiation at Different Energies in Bone Marrow. 2015 , 184, 378-91	8
1140	. 2015 ,	1
1139	Hemodynamic Differences in Intracranial Aneurysms before and after Rupture. 2015 , 36, 1927-33	19
1138	Color vision impairment in multiple sclerosis points to retinal ganglion cell damage. 2015 , 262, 2491-7	24
1137	Spatially constrained incoherent motion method improves diffusion-weighted MRI signal decay analysis in the liver and spleen. 2015 , 42, 1895-903	17
1136	Automated segmentation of the lateral ventricle in MR images of human brain. 2015 ,	3
1135	3D dento-maxillary osteolytic lesion and active contour segmentation pilot study in CBCT: semi-automatic vs manual methods. 2015 , 44, 20150079	32
1134	Reproducibility of quantitative susceptibility mapping in the brain at two field strengths from two vendors. 2015 , 42, 1592-600	69
1133	Advanced CUBIC protocols for whole-brain and whole-body clearing and imaging. 2015 , 10, 1709-27	371
1132	Volumetric magnetic resonance imaging correlates of the National Institute of Neurological Disorders and Stroke-Canadian Stroke Network vascular cognitive impairment neuropsychology protocols. 2015 , 37, 1004-12	2
1131	The emergence of age-dependent social cognitive deficits after generalized insult to the developing brain: a longitudinal prospective analysis using susceptibility-weighted imaging. 2015 , 36, 1677-91	43
1130	Automatic white matter lesion segmentation using contrast enhanced FLAIR intensity and Markov Random Field. 2015 , 45, 102-11	19
1129	Discriminating dysplasia: Optical tomographic texture analysis of colorectal polyps. 2015 , 26, 57-69	6
1128	Aspm sustains postnatal cerebellar neurogenesis and medulloblastoma growth in mice. 2015 , 142, 3921-32	44
1127	The role of early intra-operative MRI in partial resection of optic pathway/hypothalamic gliomas in children. 2015 , 31, 2055-62	11
1126	Comparative effectiveness and safety of image guidance systems in neurosurgery: a preclinical randomized study. 2015 , 123, 307-13	24
1125	Cortical Folding of the Primate Brain: An Interdisciplinary Examination of the Genetic Architecture, Modularity, and Evolvability of a Significant Neurological Trait in Pedigreed Baboons (Genus Papio). 2015 , 200, 651-65	40
1124	Computational fluid-structure interaction simulation of airflow in the human upper airway. 2015 , 48, 3685-91	32

1123	Standard chemoradiation for glioblastoma results in progressive brain volume loss. 2015 , 85, 683-91		56
1122	Aqueductal Stroke Volume: Comparisons with Intracranial Pressure Scores in Idiopathic Normal Pressure Hydrocephalus. 2015 , 36, 1623-30		32
1121	Monocular 3D Reconstruction and Augmentation of Elastic Surfaces with Self-Occlusion Handling. 2015 , 21, 1363-76		16
1120	The effect of resolution on viscous dissipation measured with 4D flow MRI in patients with Fontan circulation: Evaluation using computational fluid dynamics. 2015 , 48, 2984-9		38
1119	Validation of CBCT for the computation of textural biomarkers. 2015 , 9417,		6
1118	The Generalized Log-Ratio Transformation: Learning Shape and Adjacency Priors for Simultaneous Thigh Muscle Segmentation. 2015 , 34, 1773-87		26
1117	ERadioluminescence Imaging: A Comparative Evaluation with Cerenkov Luminescence Imaging. 2015 , 56, 1458-64		14
1116	Image-based reconstruction of three-dimensional myocardial infarct geometry for patient-specific modeling of cardiac electrophysiology. 2015 , 42, 4579-90		34
1115	Acute vascular response to cediranib treatment in human non-small-cell lung cancer xenografts with different tumour stromal architecture. 2015 , 90, 191-8		11
1114	Mapping the mouse brain with rs-fMRI: An optimized pipeline for functional network identification. <i>NeuroImage</i> , 2015 , 123, 11-21	7.9	105
1113	Scoring system for periventricular leukomalacia in infants with congenital heart disease. 2015 , 78, 304-9		9
1112	Robust ultrasound probe tracking: initial clinical experiences during robot-assisted partial nephrectomy. 2015 , 10, 1905-13		22
1111	3-D Ultrasound Segmentation of the Placenta Using the Random Walker Algorithm: Reliability and Agreement. 2015 , 41, 3182-93		31
1110	Geometric validation of self-gating k-space-sorted 4D-MRI vs 4D-CT using a respiratory motion phantom. 2015 , 42, 5787-97		10
1109	Bayesian Estimation of the Aortic Stiffness based on Non-invasive Computed Tomography Images. 2015 , 133-142		
1108	MRI evaluation of injectable hyaluronic acid-based hydrogel therapy to limit ventricular remodeling after myocardial infarction. 2015 , 69, 65-75		75
1107	Cardiac CT image enhancement for 3D heart registration and visualization. 2015 ,		
1106	Joint Estimation of Activity and Attenuation in Whole-Body TOF PET/MRI Using Constrained Gaussian Mixture Models. 2015 , 34, 1808-21		75

1105	A survey of medical image processing tools. 2015 ,	7
1104	Environmental Contributions to Social and Mental Health Outcomes Following Pediatric Stroke. 2015 , 40, 348-62	33
1103	Virtual positioning of ventricular assist device for implantation planning. 2015 , 36, 317-323	1
1102	3-D volumetric MRI evaluation of the placenta in fetuses with complex congenital heart disease. 2015 , 36, 1024-30	49
1101	Methodology for fast interactive segmentation of the peritoneum and diaphragm in multi-modal 3D medical image. 2015 , 2,	
1100	Developmental synergy between thalamic structure and interhemispheric connectivity in the visual system of preterm infants. 2015 , 8, 462-72	10
1099	Sensitivity of tumor motion simulation accuracy to lung biomechanical modeling approaches and parameters. 2015 , 60, 8833-49	19
1098	An MRI-compatible loading device to assess knee joint cartilage deformation: Effect of preloading and inter-test repeatability. 2015 , 48, 2934-40	19
1097	Joint 3-D vessel segmentation and centerline extraction using oblique Hough forests with steerable filters. 2015 , 19, 220-49	55
1096	In vivo strain assessment of the abdominal aortic aneurysm. 2015 , 48, 354-60	26
1095	Compressive strength of elderly vertebrae is reduced by disc degeneration and additional flexion. 2015 , 42, 54-66	18
1094	Condylar resorption of the temporomandibular joint: how do we treat it?. 2015 , 27, 47-67	47
1093	Using dynamic contrast-enhanced MRI to quantitatively characterize maternal vascular organization in the primate placenta. 2015 , 73, 1570-8	40
1092	Scent of the familiar: an fMRI study of canine brain responses to familiar and unfamiliar human and dog odors. 2015 , 110, 37-46	64
1091	Volumetric alterations in the nucleus accumbens and caudate nucleus in bulimia nervosa: a structural magnetic resonance imaging study. 2015 , 48, 206-14	21
1090	B-mode and acoustic radiation force impulse (ARFI) imaging of prostate zonal anatomy: comparison with 3T T2-weighted MR imaging. 2015 , 37, 22-41	14
1089	Application of micro-computed tomography to microstructure studies of the medicinal fungus <i>Hericium coralloides</i> . 2015 , 107, 227-38	2
1088	Three-Dimensional Blood Vessel Segmentation and Centerline Extraction based on Two-Dimensional Cross-Section Analysis. 2015 , 43, 1223-34	17

1087	4D MR phase and magnitude segmentations with GPU parallel computing. 2015 , 33, 134-45	2
1086	Brain organization of gorillas reflects species differences in ecology. 2015 , 156, 252-62	25
1085	Interventional digital tomosynthesis from a standard fluoroscopy system using 2D-3D registration. 2015 , 19, 137-48	2
1084	Target visibility enhancement for C-arm cone beam CT-fluoroscopy-guided hepatic needle placement: implementation and accuracy evaluation. 2015 , 10, 263-73	1
1083	Surgical navigation in paediatric orthopaedics. 2016 , 1, 152-159	10
1082	Segmentation of Brain Regions by Integrating Meta Heuristic Multilevel Threshold with Markov Random Field. 2016 , 12, 4-12	34
1081	A Multi-facetted Visual Analytics Tool for Exploratory Analysis of Human Brain and Function Datasets. 2016 , 10, 36	14
1080	Fast and accurate semiautomatic haptic segmentation of brain tumor in 3D MRI images. 2016 , 24, 1397-1411	
1079	Population reference range for developmental lumbar spinal canal size. 2016 , 6, 671-679	11
1078	Construction and investigation of 3D vessels net of the brain according to MRI data using the method of variation of scanning plane. 2016 , 722, 012029	
1077	Ultra-High Field MRI Post Mortem Structural Connectivity of the Human Subthalamic Nucleus, Substantia Nigra, and Globus Pallidus. 2016 , 10, 66	31
1076	Neonatal Brain Tissue Classification with Morphological Adaptation and Unified Segmentation. 2016 , 10, 12	61
1075	Parcellation of the Healthy Neonatal Brain into 107 Regions Using Atlas Propagation through Intermediate Time Points in Childhood. 2016 , 10, 220	25
1074	Inter-Method Discrepancies in Brain Volume Estimation May Drive Inconsistent Findings in Autism. 2016 , 10, 439	22
1073	Image Segmentation for Cardiovascular Biomedical Applications at Different Scales. 2016 , 4, 35	7
1072	Brain morphometry in Pontocerebellar Hypoplasia type 2. 2016 , 11, 100	6
1071	A bioimage informatics platform for high-throughput embryo phenotyping. 2018 , 19, 41-51	6
1070	Application of Diffusion Tensor Imaging Parameters to Detect Change in Longitudinal Studies in Cerebral Small Vessel Disease. 2016 , 11, e0147836	31

1069	Development and Implementation of a Corriedale Ovine Brain Atlas for Use in Atlas-Based Segmentation. 2016 , 11, e0155974	8
1068	Ensemble Tractography. 2016 , 12, e1004692	72
1067	Airflow in the Human Nasal Passage and Sinuses of Chronic Rhinosinusitis Subjects. 2016 , 11, e0156379	19
1066	Three-Dimensional Printing: Basic Principles and Applications in Medicine and Radiology. 2016 , 17, 182-97	136
1065	3D printing: clinical applications in orthopaedics and traumatology. 2016 , 1, 121-127	89
1064	INTRAVITREAL VERSUS SUBRETINAL ADMINISTRATION OF RECOMBINANT TISSUE PLASMINOGEN ACTIVATOR COMBINED WITH GAS FOR ACUTE SUBMACULAR HEMORRHAGES DUE TO AGE-RELATED MACULAR DEGENERATION: An Exploratory Prospective Study. 2016 , 36, 914-25	26
1063	Improved noninvasive prostate cancer assessment using multiparametric magnetic resonance imaging. 2016 ,	1
1062	Which way and how far? Tracking of translation and rotation information for human path integration. 2016 , 37, 3636-55	14
1061	Anhedonia and individual differences in orbitofrontal cortex sulcogyral morphology. 2016 , 37, 3873-3881	15
1060	Image-based quantification of 3D morphology for bifurcations in the left coronary artery: Application to stent design. 2016 , 87, 1244-55	10
1059	Computerized 3D morphological analysis of glenoid orientation. 2016 , 34, 692-8	19
1058	Peri-implant bone adaptations to overloading in rat tibiae: experimental investigations and numerical predictions. 2016 , 27, 1444-1453	8
1057	Short-term white matter alterations in Alzheimer's disease characterized by diffusion tensor imaging. 2016 , 43, 627-34	7
1056	Three-dimensional regional displacement after surgical-orthodontic correction of Class III malocclusion. 2016 , 19, 65-73	6
1055	Lung vessel segmentation in CT images using graph-cuts. 2016 ,	3
1054	Using preoperative imaging for intraoperative guidance: a case of mistaken identity. 2016 , 12, 262-7	4
1053	Lesions to right posterior parietal cortex impair visual depth perception from disparity but not motion cues. 2016 , 371,	5
1052	In vivo MRI signatures of hippocampal subfield pathology in intractable epilepsy. 2016 , 37, 1103-19	45

1051	Novel human intervertebral disc strain template to quantify regional three-dimensional strains in a population and compare to internal strains predicted by a finite element model. 2016 , 34, 1264-73	11
1050	Differences in the vascular tree of the femoral trochlear growth cartilage at osteochondrosis-susceptible sites in foals revealed by SWI 3T MRI. 2016 , 34, 1539-46	20
1049	Three-Dimensional buccal bone anatomy and aesthetic outcome of single dental implants replacing maxillary incisors. 2016 , 27, 956-63	14
1048	Estimation of aortic valve leaflets from 3D CT images using local shape dictionaries and linear coding. 2016 ,	
1047	Clinical Feasibility of Synthetic MRI in Multiple Sclerosis: A Diagnostic and Volumetric Validation Study. 2016 , 37, 1023-9	74
1046	Performance of an efficient image-registration algorithm in processing MR renography data. 2016 , 43, 391-7	6
1045	Automatic pose correction for image-guided nonhuman primate brain surgery planning. 2016 ,	
1044	Morphometric differences between central vs. surface acini in A/J mice using high-resolution micro-computed tomography. 2016 , 121, 115-22	15
1043	Multi-purpose VHP-female version 3.0 cross-platform computational human model. 2016 ,	11
1042	Risk factor analysis of cerebral white matter hyperintensities in children with sickle cell disease. 2016 , 172, 274-84	21
1041	Cerebrospinal Fluid and Parenchymal Brain Development and Growth in the Healthy Fetus. 2016 , 38, 420-429	8
1040	Additive Manufacturing of Subject-Specific Spine Model for In-Vitro Intrathecal Drug Delivery Study. 2016 ,	
1039	Dual active contours model for HR-pQCT cortical bone segmentation. 2016 ,	1
1038	Computational human model VHP-FEMALE derived from datasets of the national library of medicine. 2016 , 2016, 3350-3353	11
1037	Effect of Balloon-Expandable Transcatheter Aortic Valve Replacement Positioning: A Patient-Specific Numerical Model. 2016 , 40, E292-E304	27
1036	Hippocampal Damage Increases Deontological Responses during Moral Decision Making. 2016 , 36, 12157-12167	4
1035	MRI texture features as biomarkers to predict MGMT methylation status in glioblastomas. 2016 , 43, 2835-2844	97
1034	Structural and functional changes during epileptogenesis in the mouse model of medial temporal lobe epilepsy. 2016 , 2016, 4005-4008	2

1033	The Impact of Cardiac Motion on Aortic Valve Flow Used in Computational Simulations of the Thoracic Aorta. 2016 , 138,	3
1032	Design Optimization of a Magnetic Field-Based Localization Device for Enhanced Ventriculostomy. 2016 , 10,	10
1031	Automated choroid segmentation in three-dimensional 1- μ m wide-view OCT images with gradient and regional costs. 2016 , 21, 126017	5
1030	Anatomical pulmonary magnetic resonance imaging segmentation for regional structure-function measurements of asthma. 2016 , 43, 2911-2926	12
1029	3D-SIFT-Flow for atlas-based CT liver image segmentation. 2016 , 43, 2229	17
1028	Impact of SPECT corrections on 3D-dosimetry for liver transarterial radioembolization using the patient relative calibration methodology. 2016 , 43, 4053	14
1027	Interactive Volume Segmentation with Threshold Field Painting. 2016 ,	6
1026	Mitral valve annulus localization in 3D echocardiography. 2016 , 2016, 1087-1090	3
1025	Orthodontic and Orthognathic Surgery Planning Using CBCT. 2016 , 221-234	1
1024	Comparison of 3D reconstruction of mandible for pre-operative planning using commercial and open-source software. 2016 ,	6
1023	Simultaneous 4D-CBCT reconstruction with sliding motion constraint. 2016 , 43, 5453	5
1022	Automated multistructure atlas-assisted detection of lymph nodes using pelvic MR lymphography in prostate cancer patients. 2016 , 43, 3132-3142	2
1021	Automatic segmentation of the glenohumeral cartilages from magnetic resonance images. 2016 , 43, 5370	7
1020	Automated brain extraction and associated 3D inspection layers for the Rhesus macaque MRI datasets. 2016 ,	1
1019	Marker-free motion correction in weight-bearing cone-beam CT of the knee joint. 2016 , 43, 1235-48	36
1018	Technical Note: Cortical thickness and density estimation from clinical CT using a prior thickness-density relationship. 2016 , 43, 1945	22
1017	Learning-based 3T brain MRI segmentation with guidance from 7T MRI labeling. 2016 , 43, 6588	4
1016	Chronic exposure to haloperidol and olanzapine leads to common and divergent shape changes in the rat hippocampus in the absence of grey-matter volume loss. 2016 , 46, 3081-3093	14

1015	Quantitative assessment of biliary stent artifacts on MR images: Potential implications for target delineation in radiotherapy. 2016 , 43, 5603	6
1014	Lung surface deformation prediction from spirometry measurement and chest wall surface motion. 2016 , 43, 5493	4
1013	Comparison of distribution of lung aeration measured with EIT and CT in spontaneously breathing, awake patients1. 2016 , 27, 315-325	1
1012	Endoscopic Versus Microscopic Transsphenoidal Surgery for Pituitary Tumors. 2016 , 27, e648-e655	13
1011	Stability and sensitivity of water T obtained with IDEAL-CPMG in healthy and fat-infiltrated skeletal muscle. 2016 , 29, 1800-1812	7
1010	Technical Note: Development of a 3D printed subresolution sandwich phantom for validation of brain SPECT analysis. 2016 , 43, 5020	14
1009	Texture analysis of 2D spatial distribution of blood pharmacokinetic model parameters for endometrial carcinoma classification. 2016 ,	
1008	Flexible radioluminescence imaging for FDG-guided surgery. 2016 , 43, 5298	5
1007	Development of representative magnetic resonance imaging-based atlases of the canine brain and evaluation of three methods for atlas-based segmentation. 2016 , 77, 395-403	9
1006	Soft tissue deformation for surgical simulation: a position-based dynamics approach. 2016 , 11, 919-28	30
1005	Cortical pattern separation and item-specific memory encoding. 2016 , 85, 256-71	39
1004	Mapping of Brain Activity by Automated Volume Analysis of Immediate Early Genes. 2016 , 165, 1789-1802	391
1003	Anatomy and surgical approach of rat's vestibular sensors and nerves. 2016 , 270, 1-8	12
1002	In silico investigation of vertebroplasty as a stand-alone treatment for vertebral burst fractures. 2016 , 34, 53-61	2
1001	The influence of the modulus-density relationship and the material mapping method on the simulated mechanical response of the proximal femur in side-ways fall loading configuration. 2016 , 38, 679-689	28
1000	Three-Dimensional Measurement of Hepatocellular Carcinoma Ablation Zones and Margins for Predicting Local Tumor Progression. 2016 , 27, 1038-1045.e2	26
999	Fast generation of digitally reconstructed radiograph through an efficient preprocessing of ray attenuation values. 2016 ,	2
998	Age estimation based on pulp cavity/chamber volume of 13 types of tooth from cone beam computed tomography images. 2016 , 130, 1159-1167	49

997	Multi-modality image-based computational analysis of haemodynamics in aortic dissection. 2016 , 15, 857-76	79
996	Seeing Is Believing: Quantifying Is Convincing: Computational Image Analysis in Biology. 2016 , 219, 1-39	21
995	MRI pallidal signal in children exposed to manganese in drinking water. 2016 , 53, 124-131	21
994	Correction: Evaluation of autologous bone marrow-derived mesenchymal stem cells on renal regeneration after experimentally induced acute kidney injury in dogs. 2016 , 77, 403	1
993	Accuracy of 4D Flow Measurement of Cerebrospinal Fluid Dynamics in the Cervical Spine: An In Vitro Verification Against Numerical Simulation. 2016 , 44, 3202-3214	14
992	Objective and subjective image evaluation of maxillary alveolar bone based on cone beam computed tomography exposure parameters. 2016 , 121, 557-65	8
991	Differences in glenohumeral translations calculated with three methods: Comparison of relative positions and contact point. 2016 , 49, 1944-1947	2
990	High-resolution in vivo Wistar rodent brain atlas based on T1 weighted image. 2016 ,	
989	Tissue segmentation: a crucial tool for quantitative MRI and visualization of anatomical structures. 2016 , 29, 89-93	10
988	A Novel Approach for Patellofemoral Tracking Using a Knee Model Reconstructed with a Three-Dimensional Printer. 2016 , 3, 32-38	3
987	Development of a realistic, dynamic digital brain phantom for CT perfusion validation. 2016 ,	0
986	Semi-automated registration-based anatomical labelling, voxel based morphometry and cortical thickness mapping of the mouse brain. 2016 , 267, 62-73	30
985	Combining interpolation and 3D level set method (I+3DLSM) for medical image segmentation. 2016 , 52, 592-594	2
984	Time-dependent parameter of perfusion imaging as independent predictor of clinical outcome in symptomatic carotid artery stenosis. 2016 , 16, 50	2
983	Slic-Seg: A minimally interactive segmentation of the placenta from sparse and motion-corrupted fetal MRI in multiple views. 2016 , 34, 137-147	33
982	Breast segmentation in MRI using Poisson surface reconstruction initialized with random forest edge detection. 2016 ,	
981	Carotid artery hemodynamics before and after stenting: A patient specific CFD study. 2016 , 141, 62-74	11
980	A patient-specific follow up study of the impact of thoracic endovascular repair (TEVAR) on aortic anatomy and on post-operative hemodynamics.. 2016 , 141, 54-61	13

979	A robust statistics driven volume-scalable active contour for segmenting anatomical structures in volumetric medical images with complex conditions. 2016 , 15, 39	5
978	Morphological and Volumetric Assessment of Cerebral Ventricular System with 3D Slicer Software. 2016 , 40, 154	14
977	Strains caused by daily loading might be responsible for delayed healing of an incomplete atypical femoral fracture. 2016 , 88, 125-130	13
976	Bi-directional changes in fractional anisotropy after experiment TBI: Disorganization and reorganization?. <i>NeuroImage</i> , 2016 , 133, 129-143	7.9 44
975	Association of Automatically Quantified Total Blood Volume after Aneurysmal Subarachnoid Hemorrhage with Delayed Cerebral Ischemia. 2016 , 37, 1588-93	12
974	Common 3-dimensional coordinate system for assessment of directional changes. 2016 , 149, 645-56	52
973	Relationship of craniofacial morphology in 3-dimensional analysis of the pharynx. 2016 , 149, 683-691.e1	14
972	Automated assessment of thigh composition using machine learning for Dixon magnetic resonance images. 2016 , 29, 723-31	26
971	Toward Prostate Cancer Contouring Guidelines on Magnetic Resonance Imaging: Dominant Lesion Gross and Clinical Target Volume Coverage Via Accurate Histology Fusion. 2016 , 96, 188-96	19
970	A semi-automated workflow solution for multimodal neuroimaging: application to patients with traumatic brain injury. 2016 , 3, 1-15	17
969	Invited Commentary. 2016 , 102, 710-711	
968	Cortical folding of the preterm brain: a longitudinal analysis of extremely preterm born neonates using spectral matching. 2016 , 6, e00488	13
967	Dopamine Release in the Nonhuman Primate Caudate and Putamen Depends upon Site of Stimulation in the Subthalamic Nucleus. 2016 , 36, 6022-9	29
966	An innovative strategy for the identification and 3D reconstruction of pancreatic cancer from CT images. 2016 , 68, 273-278	8
965	Involuntary movements and coma as the prognostic marker for acute encephalopathy with biphasic seizures and late reduced diffusion. 2016 , 370, 39-43	16
964	Building the basis for patient-specific meniscal scaffolds: From human knee MRI to fabrication of 3D printed scaffolds. 2016 , 1-2, 1-10	43
963	Transmural distribution and connectivity of coronary collaterals within the human heart. 2016 , 25, 405-12	5
962	Modeling 4D Pathological Changes by Leveraging Normative Models. 2016 , 151, 3-13	2

961	Comparison of In Vivo and Ex Vivo MRI of the Human Hippocampal Formation in the Same Subjects. 2017 , 27, 5185-5196	13
960	Augmented Reality Imaging for Robot-Assisted Partial Nephrectomy Surgery. 2016 , 139-150	8
959	Surface reconstruction for planning and navigation of liver resections. 2016 , 53, 30-42	21
958	Fast diffusion kurtosis imaging of fibrotic mouse kidneys. 2016 , 29, 1709-1719	24
957	Musculoskeletal modelling under an evolutionary perspective: deciphering the role of single muscle regions in closely related insects. 2016 , 13,	10
956	Deep Learning and Data Labeling for Medical Applications. 2016 ,	26
955	Influence of the volume of soft tissue herniation on clinical symptoms of patients with orbital floor fractures. 2016 , 44, 1929-1934	25
954	In vivo delineation of subdivisions of the human amygdaloid complex in a high-resolution group template. 2016 , 37, 3979-3998	80
953	Exercise loading history and femoral neck strength in a sideways fall: A three-dimensional finite element modeling study. 2016 , 92, 9-17	14
952	Maternal choline supplementation in a sheep model of first trimester binge alcohol fails to protect against brain volume reductions in peripubertal lambs. 2016 , 55, 1-8	8
951	Medical Imaging and Augmented Reality. 2016 ,	1
950	Near-infrared light is neuroprotective in a monkey model of Parkinson disease. 2016 , 79, 59-75	57
949	Scaling and Accommodation of Jaw Adductor Muscles in Canidae. 2016 , 299, 951-66	12
948	Towards a comprehensive atlas of cortical connections in a primate brain: Mapping tracer injection studies of the common marmoset into a reference digital template. 2016 , 524, 2161-81	73
947	Patient specific modeling of palpation-based prostate cancer diagnosis: effects of pelvic cavity anatomy and intrabladder pressure. 2016 , 32, e02734	5
946	Automated analysis of hip joint cartilage combining MR T2 and three-dimensional fast-spin-echo images. 2016 , 75, 403-13	11
945	Factors associated with recurrent stroke and recanalization in patients presenting with isolated symptomatic carotid occlusion. 2016 , 23, 127-32	6
944	Traumatic Brain Injury Results in Cellular, Structural and Functional Changes Resembling Motor Neuron Disease. 2017 , 27, 4503-4515	40

943	Identification, visualization and clonal analysis of intestinal stem cells in fish. 2016 , 143, 3470-3480	31
942	Modeling the Myxomatous Mitral Valve With Three-Dimensional Echocardiography. 2016 , 102, 703-710	8
941	Late-onset depressive symptoms increase the risk of dementia in small vessel disease. 2016 , 87, 1102-9	11
940	Atlas-guided generation of pseudo-CT images for MRI-only and hybrid PET-MRI-guided radiotherapy treatment planning. 2016 , 61, 6531-52	54
939	An efficient similarity-based level set model for medical image segmentation. 2016 , 10, JAMDSM0100-JAMDSM0100	10
938	Evaluation of the HeartWare ventricular assist device Lavare cycle in a particle image velocimetry model and in clinical practice. 2016 , 50, 839-848	34
937	Role of mTOR Inhibitors in Growth Hormone-Producing Pituitary Adenomas Harboring Different FGFR4 Genotypes. 2016 , 157, 3577-87	7
936	Fuzzy energy based active contours model for HR-PQCT cortical bone segmentation. 2016 ,	2
935	Routine use of an aortic balloon to resolve possible inflow stenosis induced by the inflatable ring fixation mechanism of the Ovation endograft. 2016 , 121, 882-889	3
934	Quantitative Classification of Cerebellar Foliation in Cartilaginous Fishes (Class: Chondrichthyes) Using Three-Dimensional Shape Analysis and Its Implications for Evolutionary Biology. 2016 , 87, 252-64	4
933	Estimation of adipose compartment volumes in CT images of a mastectomy specimen. 2016 ,	3
932	Clearance of Subarachnoid Hemorrhage from the Cerebrospinal Fluid in Computational and In Vitro Models. 2016 , 44, 3478-3494	17
931	Large-scale Radiomic Profiling of Recurrent Glioblastoma Identifies an Imaging Predictor for Stratifying Anti-Angiogenic Treatment Response. 2016 , 22, 5765-5771	173
930	High-field magnetic resonance imaging of structural alterations in first-episode, drug-naïve patients with major depressive disorder. 2016 , 6, e942	31
929	Automatic Three-dimensional Detection of Photoreceptor Ellipsoid Zone Disruption Caused by Trauma in the OCT. 2016 , 6, 25433	11
928	N-terminal pro-brain natriuretic peptide and subclinical brain small vessel disease. 2016 , 87, 2533-2539	11
927	Transient effects of tumor location on the functional architecture at rest in glioblastoma patients: three longitudinal case studies. 2016 , 11, 107	11
926	Supervised learning technique for the automated identification of white matter hyperintensities in traumatic brain injury. 2016 , 30, 1458-1468	16

925	Improving assessment of congenital heart disease through rapid patient specific modeling. 2016 , 2016, 1228-1231	
924	Multi-modal Brain Tumor Segmentation Based on Self-organizing Active Contour Model. 2016 , 486-498	1
923	Magnetic resonance imaging reveals functional anatomy and biomechanics of a living dragon tree. 2016 , 6, 32685	13
922	A fossil biting midge (Diptera: Ceratopogonidae) from early Eocene Indian amber with a complex pheromone evaporator. 2016 , 6, 34352	9
921	Deep Learning of Brain Lesion Patterns for Predicting Future Disease Activity in Patients with Early Symptoms of Multiple Sclerosis. 2016 , 86-94	15
920	Virtual Simulation. 2016 , 137-149	
919	Multimodal Correlative Preclinical Whole Body Imaging and Segmentation. 2016 , 6, 27940	12
918	ITK-SNAP: An interactive tool for semi-automatic segmentation of multi-modality biomedical images. 2016 , 2016, 3342-3345	121
917	A skeleton-tree-based approach to acinar morphometric analysis using microcomputed tomography with comparison of acini in young and old C57BL/6 mice. 2016 , 120, 1402-9	6
916	Third Trimester Brain Growth in Preterm Infants Compared With In Utero Healthy Fetuses. 2016 , 138,	69
915	Complex Trajectories of Brain Development in the Healthy Human Fetus. 2017 , 27, 5274-5283	53
914	Postediting prostate magnetic resonance imaging segmentation consistency and operator time using manual and computer-assisted segmentation: multiobserver study. 2016 , 3, 046002	1
913	Decoding the view expectation during learned maze navigation from human fronto-parietal network. 2015 , 5, 17648	4
912	Geometric features of pig airways using computed tomography. 2016 , 4, e12995	10
911	Ultrasound image analysis for myopathy detection. 2016 ,	2
910	Haemodynamics of giant cerebral aneurysm: A comparison between the rigid-wall, one-way and two-way FSI models. 2016 , 722, 012042	3
909	Computer-Assisted Transcatheter Heart Valve Implantation in Valve-in-Valve Procedures. 2016 , 11, 193-200	8
908	Transcranial ultrasound of cerebral vessels in silico: proof of concept. 2016 , 31,	8

907	Technical note: Performance of semi and fully automated approaches for registration of 3D surface coordinates in geometric morphometric studies. 2016 , 160, 169-78		17
906	Bayesian estimation of non-rigid mechanical parameters using temporal sequences of deformation samples. 2016 ,		1
905	The 100 most-cited articles in neuroimaging: A bibliometric analysis. <i>NeuroImage</i> , 2016 , 139, 149-156	7.9	46
904	Comparison of electric field strength and spatial distribution of electroconvulsive therapy and magnetic seizure therapy in a realistic human head model. 2016 , 36, 55-64		43
903	Radiomic Profiling of Glioblastoma: Identifying an Imaging Predictor of Patient Survival with Improved Performance over Established Clinical and Radiologic Risk Models. 2016 , 280, 880-9		247
902	The spatiotemporal hemodynamic response function for depth-dependent functional imaging of human cortex. <i>NeuroImage</i> , 2016 , 139, 240-248	7.9	30
901	Robust preprocessing for stimulus-based functional MRI of the moving fetus. 2016 , 3, 026001		11
900	Real-time pose estimation of devices from x-ray images: Application to x-ray/echo registration for cardiac interventions. 2016 , 34, 101-108		11
899	STGP: Spatio-temporal Gaussian process models for longitudinal neuroimaging data. <i>NeuroImage</i> , 2016 , 134, 550-562	7.9	19
898	Dentatorubrothalamic tract localization with postmortem MR diffusion tractography compared to histological 3D reconstruction. 2016 , 221, 3487-501		31
897	Possum-A Framework for Three-Dimensional Reconstruction of Brain Images from Serial Sections. 2016 , 14, 265-78		23
896	Renal compartment segmentation in DCE-MRI images. 2016 , 32, 269-80		15
895	Bingham-NODDI: Mapping anisotropic orientation dispersion of neurites using diffusion MRI. <i>NeuroImage</i> , 2016 , 133, 207-223	7.9	97
894	A brain stress test: Cerebral perfusion during memory encoding in mild cognitive impairment. 2016 , 11, 388-397		20
893	Registration of Real-Time 3-D Ultrasound to Tomographic Images of the Abdominal Aorta. 2016 , 42, 2026-32		2
892	In-vivo heterogeneous functional and residual strains in human aortic valve leaflets. 2016 , 49, 2481-90		22
891	Segmentation of perivascular spaces in 7T MR image using auto-context model with orientation-normalized features. <i>NeuroImage</i> , 2016 , 134, 223-235	7.9	19
890	Implications of newborn amygdala connectivity for fear and cognitive development at 6-months-of-age. 2016 , 18, 12-25		70

889	Free-form image registration of human cochlear μ CT data using skeleton similarity as anatomical prior. 2016 , 76, 76-82		10
888	Comparaç� de 2 disjuntores na expans� maxilar em pacientes com fenda labiopalatina: relato de 2 casos. 2016 , 57, 116-124		
887	fMRI mapping of the visual system in the mouse brain with interleaved snapshot GE-EPI. <i>NeuroImage</i> , 2016 , 139, 337-345	7.9	19
886	One registration multi-atlas-based pseudo-CT generation for attenuation correction in PET/MRI. 2016 , 43, 2021-35		26
885	Three-dimensional lateral pterygoid muscle volume: MRI analyses with insertion patterns correlation. 2016 , 208, 9-18		5
884	Clinical parameters outweigh diffusion- and perfusion-derived MRI parameters in predicting survival in newly diagnosed glioblastoma. 2016 , 18, 1673-1679		27
883	Safety and Efficacy of Gamma Knife Radiosurgery for the Management of Koos Grade 4 Vestibular Schwannomas. 2016 , 78, 521-30		22
882	Impact of end-diastolic and end-systolic phase selection in the volumetric evaluation of cardiac MRI. 2016 , 43, 585-93		3
881	Three-dimensional virtual navigation versus conventional image guidance: A randomized controlled trial. 2016 , 126, 1510-5		11
880	Simultaneous quantitative mapping of conductivity and susceptibility using a double-echo ultrashort echo time sequence: Example using a hematoma evolution study. 2016 , 76, 214-21		13
879	Reconstruction of unbroken vasculature of mouse by varying the slope of the scan plane in MRI. 2016 , 677, 012003		
878	Automatic thalamus and hippocampus segmentation from MP2RAGE: comparison of publicly available methods and implications for DTI quantification. 2016 , 11, 1979-1991		31
877	Data integration: Combined imaging and electrophysiology data in the cloud. <i>NeuroImage</i> , 2016 , 124, 1175-1181	7.9	28
876	Data and feature mixed ensemble based extreme learning machine for medical object detection and segmentation. 2016 , 75, 2815-2837		17
875	A method for the automatic segmentation of brown adipose tissue. 2016 , 29, 287-99		11
874	A Conjugate Fluid-Porous Approach for Simulating Airflow in Realistic Geometric Representations of the Human Respiratory System. 2016 , 138, 4032113		1
873	Altered white matter and cortical structure in neonates with antenatally diagnosed isolated ventriculomegaly. 2016 , 11, 139-148		13
872	Bilateral Transcranial Direct Current Stimulation Language Treatment Enhances Functional Connectivity in the Left Hemisphere: Preliminary Data from Aphasia. 2016 , 28, 724-38		64

871	4D cone-beam CT reconstruction using multi-organ meshes for sliding motion modeling. 2016 , 61, 996-1020	13
870	Papillary Muscle Segmentation from a Multi-atlas Database: A Feasibility Study. 2016 , 80-89	
869	Characterization of Breast Implant Surfaces, Shapes, and Biomechanics: A Comparison of High Cohesive Anatomically Shaped Textured Silicone, Breast Implants from Three Different Manufacturers. 2016 , 40, 89-97	24
868	Statistical Atlases and Computational Models of the Heart. Imaging and Modelling Challenges. 2016 ,	3
867	Hemodynamic impact of abdominal aortic aneurysm stent-graft implantation-induced stenosis. 2016 , 54, 1523-32	11
866	Geometrical aspects of patient-specific modelling of the intervertebral disc: collagen fibre orientation and residual stress distribution. 2016 , 15, 543-60	15
865	Comparison of cortical folding measures for evaluation of developing human brain. <i>NeuroImage</i> , 2016 , 125, 780-790	7.9 56
864	Visual motion transforms visual space representations similarly throughout the human visual hierarchy. <i>NeuroImage</i> , 2016 , 127, 173-185	7.9 21
863	Role of "major" and "minor" lambdoid arch sutures in posterior cranial fossa changes: mechanism of cerebellar tonsillar herniation in infants with multisutural craniosynostosis. 2016 , 32, 451-9	10
862	Automated Assessment of Right Ventricular Volumes and Function Using Three-Dimensional Transesophageal Echocardiography. 2016 , 42, 596-606	5
861	Bayesian segmentation of human facial tissue using 3D MR-CT information fusion, resolution enhancement and partial volume modelling. 2016 , 124, 31-44	3
860	The homology of cephalic muscles and endoskeletal elements between Diplura and Ectognatha (Insecta). 2016 , 16, 241-257	4
859	The average baboon brain: MRI templates and tissue probability maps from 89 individuals. <i>NeuroImage</i> , 2016 , 132, 526-533	7.9 34
858	MaterialCloning: Acquiring Elasticity Parameters from Images for Medical Applications. 2016 , 22, 2122-35	8
857	Clinical correlates of lung ventilation defects in asthmatic children. 2016 , 137, 789-96.e7	32
856	Bildverarbeitung für die Medizin 2016. 2016 ,	1
855	Diffusion tensor imaging of the hippocampus predicts the risk of dementia; the RUN DMC study. 2016 , 37, 327-37	17
854	Optimizing the 3D-reconstruction technique for serial block-face scanning electron microscopy. 2016 , 264, 16-24	6

853	CT thermometry for cone-beam CT guided ablation. 2016 ,	2
852	SCEM+: Real-Time Robust Simultaneous Catheter and Environment Modeling for Endovascular Navigation. 2016 , 1, 961-968	6
851	Comparison and reproducibility of 2 regions of reference for maxillary regional registration with cone-beam computed tomography. 2016 , 149, 533-42	37
850	Relation between wall shear stress and carotid artery wall thickening MRI versus CFD. 2016 , 49, 735-741	33
849	Anatomic Mesenchymal Stem Cell-Based Engineered Cartilage Constructs for Biologic Total Joint Replacement. 2016 , 22, 386-95	21
848	Fixation of a split fracture of the lateral tibial plateau with a locking screw plate instead of cannulated screws would allow early weight bearing: a computational exploration. 2016 , 40, 2163-2169	24
847	Magnetic resonance imaging-guided attenuation correction in whole-body PET/MRI using a sorted atlas approach. 2016 , 31, 1-15	32
846	Radiological signs of the syndrome of the trephined. 2016 , 58, 557-568	20
845	Segmentation and characterization of interscapular brown adipose tissue in rats by multi-parametric magnetic resonance imaging. 2016 , 29, 277-86	17
844	The Role of Dopamine in Value-Based Attentional Orienting. 2016 , 26, 550-5	78
843	Quantification of Porcine Vocal Fold Geometry. 2016 , 30, 416-26	8
842	Visualization of perivascular spaces in the human brain at 7T: sequence optimization and morphology characterization. <i>NeuroImage</i> , 2016 , 125, 895-902	7.9 36
841	Whole-body and Whole-Organ Clearing and Imaging Techniques with Single-Cell Resolution: Toward Organism-Level Systems Biology in Mammals. 2016 , 23, 137-157	201
840	Voxelized Model of Brain Infusion That Accounts for Small Feature Fissures: Comparison With Magnetic Resonance Tracer Studies. 2016 , 138, 051007	11
839	Facing the Time Window in Acute Ischemic Stroke: The Infarct Core. 2016 , 26, 153-8	8
838	Image-Based Personalization of Cardiac Anatomy for Coupled Electromechanical Modeling. 2016 , 44, 58-70	41
837	MR Perfusion-derived Hemodynamic Parametric Response Mapping of Bevacizumab Efficacy in Recurrent Glioblastoma. 2016 , 279, 542-52	43
836	Longitudinal patterns of leukoaraiosis and brain atrophy in symptomatic small vessel disease. 2016 , 139, 1136-51	75

835	Musculoskeletal modelling of the dragonfly mandible system as an aid to understanding the role of single muscles in an evolutionary context. 2016 , 219, 1041-9		13
834	Visual field impairment captures disease burden in multiple sclerosis. 2016 , 263, 695-702		13
833	Registration of dynamic multiview 2D ultrasound and late gadolinium enhanced images of the heart: Application to hypertrophic cardiomyopathy characterization. 2016 , 28, 13-21		7
832	Detection and Clinical Patterns of Nephron Hypertrophy and Nephrosclerosis Among Apparently Healthy Adults. 2016 , 68, 58-67		49
831	X-ray and magnetic resonance imaging fusion for cardiac resynchronization therapy. 2016 , 31, 98-107		8
830	Amygdala subnuclei response and connectivity during emotional processing. <i>NeuroImage</i> , 2016 , 133, 98-110	7.9	45
829	MR image bias field harmonic approximation with histogram statistical analysis. 2016 , 83, 91-98		3
828	Pituitary Medicine From Discovery to Patient-Focused Outcomes. 2016 , 101, 769-77		30
827	Motor deficits associated with Huntington's disease occur in the absence of striatal degeneration in BACHD transgenic mice. 2016 , 25, 1780-91		20
826	Multi-scale patch and multi-modality atlases for whole heart segmentation of MRI. 2016 , 31, 77-87		165
825	Correlation between hyoid bone position and airway dimensions in Chinese adolescents by cone beam computed tomography analysis. 2016 , 45, 914-21		18
824	Quantifying fracture geometry with X-ray tomography: Technique of Iterative Local Thresholding (TILT) for 3D image segmentation. 2016 , 20, 231-244		42
823	Common Variation in the DOPA Decarboxylase (DDC) Gene and Human Striatal DDC Activity In Vivo. 2016 , 41, 2303-8		15
822	Kernel regression estimation of fiber orientation mixtures in diffusion MRI. <i>NeuroImage</i> , 2016 , 127, 158-172	17.2	27
821	Disconnection and hyper-connectivity underlie reorganization after TBI: A rodent functional connectomic analysis. 2016 , 277, 124-138		51
820	Surgically resected skull base meningiomas demonstrate a divergent postoperative recurrence pattern compared with non-skull base meningiomas. 2016 , 125, 431-40		34
819	Comparative Local Quality Assessment of 3D Medical Image Segmentations with Focus on Statistical Shape Model-Based Algorithms. 2016 , 22, 2537-2549		10
818	Development and validation of real-time simulation of X-ray imaging with respiratory motion. 2016 , 49, 1-15		18

817	Prediction of patient-specific post-operative outcomes of TAVI procedure: The impact of the positioning strategy on valve performance. 2016 , 49, 2513-9	48
816	Cortical vessel sign on susceptibility weighted imaging reveals clinically relevant hypoperfusion in internal carotid artery stenosis. 2016 , 85, 534-9	18
815	The nasal septum deviation index (NSDI) based on CBCT data. 2016 , 45, 20150327	16
814	Association of body mass index and the depletion of nigrostriatal dopamine in Parkinson's disease. 2016 , 38, 197-204	26
813	Entorhinal volume, aerobic fitness, and recognition memory in healthy young adults: A voxel-based morphometry study. <i>NeuroImage</i> , 2016 , 126, 229-38	7.9 42
812	MRI biomarker assessment of neuromuscular disease progression: a prospective observational cohort study. 2016 , 15, 65-77	172
811	Apolipoprotein E ?4 is positively related to spatial performance but unrelated to hippocampal volume in healthy young adults. 2016 , 299, 11-8	11
810	Computational modeling of cardiac hemodynamics: Current status and future outlook. 2016 , 305, 1065-1082	97
809	In Vitro Determination of Respimat Dose Delivery in Children: An Evaluation Based on Inhalation Flow Profiles and Mouth-Throat Models. 2016 , 29, 76-85	9
808	A New MRI-Based Pediatric Subcortical Segmentation Technique (PSST). 2016 , 14, 69-81	16
807	A probabilistic atlas of the cerebellar white matter. <i>NeuroImage</i> , 2016 , 124, 724-732	7.9 54
806	CustusX: an open-source research platform for image-guided therapy. 2016 , 11, 505-19	49
805	Effects of Vessel Tortuosity on Coronary Hemodynamics: An Idealized and Patient-Specific Computational Study. 2016 , 44, 2228-39	36
804	Cone beam computed tomography-based models versus multislice spiral computed tomography-based models for assessing condylar morphology. 2016 , 121, 96-105	5
803	Model-based segmentation in orbital volume measurement with cone beam computed tomography and evaluation against current concepts. 2016 , 11, 1-9	35
802	Sound transmission in porcine thorax through airway insonification. 2016 , 54, 675-89	11
801	Computer-assisted liver tumor surgery using a novel semiautomatic and a hybrid semiautomatic segmentation algorithm. 2016 , 54, 711-21	11
800	Preparation of Ga-labelled DOTA-peptides using a manual labelling approach for small-animal PET imaging. 2016 , 107, 113-120	6

799	Extra-ocular muscle MRI in genetically-defined mitochondrial disease. 2016 , 26, 130-7	17
798	Patient-Specific Biomechanical Modeling for Guidance During Minimally-Invasive Hepatic Surgery. 2016 , 44, 139-53	74
797	Planar dGEMRIC Maps May Aid Imaging Assessment of Cartilage Damage in Femoroacetabular Impingement. 2016 , 474, 467-78	18
796	Reconstruction of Complex Vasculature by Varying the Slope of the Scan Plane in High-Field Magnetic Resonance Imaging. 2016 , 47, 23-39	4
795	Toward Quantitative Assessment of Rheumatoid Arthritis Using Volumetric Ultrasound. 2016 , 63, 449-58	8
794	Numerical investigation of fluid-particle interactions for embolic stroke. 2016 , 30, 23-39	27
793	From CT scanning to 3-D printing technology for the preoperative planning in laparoscopic splenectomy. 2016 , 30, 366-71	47
792	Poro-elastic modeling of Syringomyelia - a systematic study of the effects of pia mater, central canal, median fissure, white and gray matter on pressure wave propagation and fluid movement within the cervical spinal cord. 2016 , 19, 686-98	24
791	A mechanostatistical approach to cortical bone remodelling: an equine model. 2016 , 15, 29-42	13
790	A Major Human White Matter Pathway Between Dorsal and Ventral Visual Cortex. 2016 , 26, 2205-2214	97
789	Assessment of the ABC/2 Method of Epidural Hematoma Volume Measurement as Compared to Computer-Assisted Planimetric Analysis. 2016 , 18, 5-11	21
788	SmartPaint: a tool for interactive segmentation of medical volume images. 2017 , 5, 36-44	14
787	The Corticocortical Structural Connectivity of the Human Insula. 2017 , 27, 1216-1228	122
786	Speckle Patch Similarity for Echogenicity-Based Multiorgan Segmentation in Ultrasound Images of the Thyroid Gland. 2017 , 21, 172-183	14
785	Assessment of tumor oxygenation and its impact on treatment response in bevacizumab-treated recurrent glioblastoma. 2017 , 37, 485-494	28
784	Quantitative susceptibility mapping detects abnormalities in cartilage canals in a goat model of preclinical osteochondritis dissecans. 2017 , 77, 1276-1283	20
783	Estimation of an image derived input function with MR-defined carotid arteries in FDG-PET human studies using a novel partial volume correction method. 2017 , 37, 1398-1409	27
782	Patient-specific finite element analysis of popliteal stenting. 2017 , 52, 633-644	15

781	Intrinsic functional connectivity in late-life depression: trajectories over the course of pharmacotherapy in remitters and non-remitters. 2017 , 22, 450-457	40
780	Habenula volume increases with disease severity in unmedicated major depressive disorder as revealed by 7T MRI. 2017 , 267, 107-115	30
779	Development of cloud services for patient-specific simulations of blood flows through aortic valves. 2017 , 103, 57-64	10
778	Estimation of conditions evoking fracture in finger bones under pinch loading based on finite element analysis. 2017 , 20, 35-44	2
777	Soft tissue coverage on the segmentation accuracy of the 3D surface-rendered model from cone-beam CT. 2017 , 21, 921-930	3
776	Toward translating near-infrared spectroscopy oxygen saturation data for the non-invasive prediction of spatial and temporal hemodynamics during exercise. 2017 , 16, 75-96	6
775	Multimodal Imaging for In Vivo Evaluation of Induced Pluripotent Stem Cells in a Murine Model of Heart Failure. 2017 , 41, 192-199	8
774	Estimation of Penetrated Bone Layers During Craniotomy via Bioimpedance Measurement. 2017 , 64, 765-774	6
773	Depth-dependence of visual signals in the human superior colliculus at 9.4 T. 2017 , 38, 574-587	6
772	Investigating magnetic susceptibility of human knee joint at 7 Tesla. 2017 , 78, 1933-1943	45
771	Amyloid-Beta Deposition is Associated with Increased Medial Temporal Lobe Activation during Memory Encoding in the Cognitively Normal Elderly. 2017 , 25, 551-560	9
770	9.4 T MR microscopy of the substantia nigra with pathological validation in controls and disease. 2017 , 13, 154-163	36
769	Impresi3 tridimensional de modelos cardiacos: aplicaciones en el campo de la educaci3 m3dica, la cirug3 cardiaca y el intervencionismo estructural. 2017 , 70, 282-291	50
768	Benefits and Limitations of Entry-Level 3-Dimensional Printing of Maxillofacial Skeletal Models. 2017 , 143, 389-394	17
767	Evaluation of a laminin-alginate biomaterial, adipocytes, and adipocyte-derived stem cells interaction in animal autologous fat grafting model using 7-Tesla magnetic resonance imaging. 2017 , 28, 18	8
766	Sleep Apnea in Multiple System Atrophy of Cerebellar Type: A 3.0 T MRS/Volumetry Pilot Study. 2017 , 6, 6-8	1
765	Reducing uncertainty when using knee-specific finite element models by assessing the effect of input parameters. 2017 , 35, 2233-2242	5
764	Qualitative Evaluation of a Novel 3D Volumetric Radiotherapy Segmentation Tool. 2017 , 48, 178-183	1

763	Lesion-symptom mapping in the study of spoken language understanding. 2017 , 32, 891-899	19
762	Magnetic resonance fingerprinting based on realistic vasculature in mice. <i>NeuroImage</i> , 2017 , 149, 436-445	14
761	Exploring the origins of echo-time-dependent quantitative susceptibility mapping (QSM) measurements in healthy tissue and cerebral microbleeds. <i>NeuroImage</i> , 2017 , 149, 98-113	7.9 49
760	Putamen Development in Children 12 to 21 Months Old. 2016 , 10160,	
759	Measuring neuroplasticity associated with cerebral palsy rehabilitation: An MRI based power analysis. 2017 , 58, 17-25	19
758	Folding, But Not Surface Area Expansion, Is Associated with Cellular Morphological Maturation in the Fetal Cerebral Cortex. 2017 , 37, 1971-1983	34
757	Correlations of atrial diameter and frontooccipital horn ratio with ventricle size in fetal ventriculomegaly. 2017 , 19, 300-306	7
756	Routine clinical application of virtual reality in abdominal surgery. 2017 , 26, 135-143	18
755	Structural and congenital heart disease interventions: the role of three-dimensional printing. 2017 , 25, 65-75	40
754	Sex-related difference in human white matter volumes studied: Inspection of the corpus callosum and other white matter by VBM. 2017 , 7, 39818	16
753	BoneSplit - A 3D Painting Tool for Interactive Bone Segmentation in CT Images. 2017 , 3-13	
752	Asymmetric dopaminergic degeneration and levodopa alter functional corticostriatal connectivity bilaterally in experimental parkinsonism. 2017 , 292, 11-20	12
751	Impact of Thoracic Endovascular Aortic Repair on Pulsatile Circumferential and Longitudinal Strain in Patients With Aneurysm. 2017 , 24, 281-289	12
750	Flow mixing during peripheral veno-arterial extra corporeal membrane oxygenation - A simulation study. 2017 , 55, 64-70	28
749	3D Printing Technology in Craniofacial Surgery and Salivary Gland Regeneration. 2017 , 173-191	
748	Thoracic CT-MRI coregistration for regional pulmonary structure-function measurements of obstructive lung disease. 2017 , 44, 1718-1733	11
747	Hippocampal subregion volume changes associated with antipsychotic treatment in first-episode psychosis. 2017 , 47, 1706-1718	17
746	Localized-atlas-based segmentation of breast MRI in a decision-making framework. 2017 , 40, 69-84	7

745	Three-dimensional Printed Cardiac Models: Applications in the Field of Medical Education, Cardiovascular Surgery, and Structural Heart Interventions. 2017 , 70, 282-291	27
744	Evaluation of deformable image registration between external beam radiotherapy and HDR brachytherapy for cervical cancer with a 3D-printed deformable pelvis phantom. 2017 , 44, 1445-1455	26
743	Brain tumor classification from multi-modality MRI using wavelets and machine learning. 2017 , 20, 871-881	94
742	Minimally invasive, multi-port approach to the lateral skull base: a first in vitro evaluation. 2017 , 12, 889-895	4
741	Detecting Clinically Meaningful Shape Clusters in Medical Image Data: Metrics Analysis for Hierarchical Clustering Applied to Healthy and Pathological Aortic Arches. 2017 , 64, 2373-2383	48
740	Quantifying the reproducibility of lung ventilation images between 4-Dimensional Cone Beam CT and 4-Dimensional CT. 2017 , 44, 1771-1781	6
739	Optimization of the simulation parameters for improving realism in anthropomorphic breast phantoms. 2017 ,	1
738	Continuous measurement of aortic dimensions in Turner syndrome: a cardiovascular magnetic resonance study. 2017 , 19, 20	9
737	Spatiotemporal alignment of in utero BOLD-MRI series. 2017 , 46, 403-412	20
736	Prediction of malignancy by a radiomic signature from contrast agent-free diffusion MRI in suspicious breast lesions found on screening mammography. 2017 , 46, 604-616	87
735	Can responses to basic non-numerical visual features explain neural numerosity responses?. <i>NeuroImage</i> , 2017 , 149, 200-209	7.9 26
734	Computational biomechanics changes our view on insect head evolution. 2017 , 284,	13
733	The relationship between loading history and proximal femoral diaphysis cross-sectional geometry. 2017 , 29, e22965	18
732	Morphology and physiology of antennal lobe projection neurons in the hawkmoth <i>Agrius convolvuli</i> . 2017 , 98, 214-222	9
731	Hippocampal subfields at ultra high field MRI: An overview of segmentation and measurement methods. 2017 , 27, 481-494	39
730	Mapping of pain circuitry in early post-natal development using manganese-enhanced MRI in rats. 2017 , 352, 180-189	14
729	Fully automated segmentation of whole breast using dynamic programming in dynamic contrast enhanced MR images. 2017 , 44, 2400-2414	18
728	Segmentation of left ventricle on dynamic MRI sequences for blood flow cancellation in ThermoTherapy. 2017 , 59, 37-49	4

727	Temporal slice registration and robust diffusion-tensor reconstruction for improved fetal brain structural connectivity analysis. <i>NeuroImage</i> , 2017 , 156, 475-488	7.9	44
726	A Method for In Vitro TCPC Compliance Verification. 2017 , 139,		8
725	The human amygdala parametrically encodes the intensity of specific facial emotions and their categorical ambiguity. 2017 , 8, 14821		67
724	Deformation behavior of nano-porous polycrystalline silver. Part II: Simulations. 2017 , 131, 564-573		11
723	Intra-arterial verapamil post-thrombectomy is feasible, safe, and neuroprotective in stroke. 2017 , 37, 3531-3543		31
722	Multi-stage 3D-2D registration for correction of anatomical deformation in image-guided spine surgery. 2017 , 62, 4604-4622		18
721	MRI assessment of tissue effects after 180-W XPS greenlight laser vaporization of the prostate. 2017 , 49, 577-581		3
720	Smoothing the Undersampled Carpal Bone Model with Small Volume and Large Curvature: A Feasibility Study. 2022 , 12, 770		0
719	Characterization of microparticles of iron oxide for magnetic resonance imaging. 2022 ,		
718	CT-Based Radiomics and Deep Learning for BRCA Mutation and Progression-Free Survival Prediction in Ovarian Cancer Using a Multicentric Dataset. 2022 , 14, 2739		0
717	Tissue Sampling and Homogenization with NIRL Enables Spatially Resolved Cell Layer Specific Proteomic Analysis of the Murine Intestine. 2022 , 23, 6132		
716	Comparison of loupes versus microscope-enhanced CAD-CAM crown preparations: A microcomputed tomography analysis of marginal gaps. 2022 ,		
715	Spontaneous neuronal oscillations in the human insula are hierarchically organized traveling waves. 11,		0
714	Association of cerebral microvascular dysfunction and white matter injury in Alzheimer's disease.		0
713	Topological Data Analysis of Thoracic Radiographic Images shows Improved Radiomics-based Lung Tumor Histology Prediction.		
712	ID-Seg: an infant deep learning-based segmentation framework to improve limbic structure estimates. 2022 , 9,		1
711	How Egg Storage Duration Prior to Incubation Impairs Egg Quality and Chicken Embryonic Development: Contribution of Imaging Technologies. 2022 , 13,		0
710	Coexistence of Cue-specific and Cue-independent Spatial Representations for Landmarks and Self-motion Cues in Human Retrosplenial Cortex.		

- 709 A Nomogram Combined Radiomics and Clinical Features as Imaging Biomarkers for Prediction of Visceral Pleural Invasion in Lung Adenocarcinoma. 12, 0
- 708 Brain Iron and Mental Health Symptoms in Youth with and without Prenatal Alcohol Exposure. **2022**, 14, 2213 0
- 707 Quantitative T2 and T1 mapping are sensitive to ischemic injury to the epiphyseal cartilage in an in vivo piglet model of Legg-Calvé-Perthes disease. **2022**, 1
- 706 Maternal psychological distress during the COVID-19 pandemic and structural changes of the human fetal brain. **2022**, 2, 1
- 705 A Fast Method for Whole Liver- and Colorectal Liver Metastasis Segmentations from MRI Using 3D FCNN Networks. **2022**, 12, 5145
- 704 Spatial signatures of anesthesia-induced burst-suppression differ between primates and rodents. 11, 0
- 703 Deep Learning Super-resolution MR Spectroscopic Imaging of Brain Metabolism and Mutant IDH Glioma. 1
- 702 A Fetal Brain magnetic resonance Acquisition Numerical phantom (FaBiAN). **2022**, 12,
- 701 Quantification of epicardial adipose tissue in obese patients using an open-bore MR scanner. **2022**, 6,
- 700 Distinguishing Tumor Admixed in a Radiation Necrosis (RN) Background: 1H and 2H MR With a Novel Mouse Brain-Tumor/RN Model. 12, 0
- 699 Improved Joint Health Following Oral Administration of Glycosaminoglycans with Native Type II Collagen in a Rabbit Model of Osteoarthritis. **2022**, 12, 1401 0
- 698 T staging with functional and radiomics parameters of computed tomography in colorectal cancer patients. **2022**, 101, e29244 1
- 697 Framework to Segment and Evaluate Multiple Sclerosis Lesion in MRI Slices Using VGG-UNet. **2022**, 2022, 1-10 2
- 696 BRAIN ANOMALIES IN EARLY PSYCHOSIS: FROM SECONDARY TO PRIMARY PSYCHOSIS. **2022**, 104716
- 695 Microvascular imaging of the unstained human superior colliculus using synchrotron-radiation phase-contrast microtomography. **2022**, 12, 0
- 694 Feasibility of 3T layer-dependent fMRI with GE-BOLD using NORDIC and phase regression. 0
- 693 Longitudinal Brain Changes After Stroke and the Association With Cognitive Decline. 13, 0
- 692 Incubation of palatable food craving is associated with brain-wide neuronal activation in mice.

- 691 CAU-Net: A Deep Learning Method for Deep Gray Matter Nuclei Segmentation. **2022**, 16,
- 690 Hidden brain atrophy in ultra-high field MR images in a transgenic rat model of Huntington's disease. **2022**, 6, 100039
- 689 Modeling spatial, developmental, physiological, and topological constraints on human brain connectivity. **2022**, 8, 1
- 688 Application of digital processing methods for automated cardiac segmentation from computed tomography data. **2022**, 41, 49-54
- 687 Metaphyseal sleeves in revision total knee arthroplasties: Computational analysis of bone remodeling. **2022**, 37, 10-19 0
- 686 VoxelMorph++: a convolutional neural network architecture for unsupervised CBCT to CT deformable image registration. **2022**, 47, 02014
- 685 The Brain Structure and the Neural Network Features of the Cuttlefish, <i>Sepia plangon</i>: A Comparative Study With Cuttlefish, Octopus and Squid.
- 684 External root resorption evaluated by CBCT 3D models superimposition. **2022**, 27,
- 683 Computational Fluid Dynamics Applications in Cardiovascular MedicineFrom Medical Image-Based Modeling to Simulation: Numerical Analysis of Blood Flow in Abdominal Aorta. **2022**, 1-42 0
- 682 Knee Bone and Cartilage Segmentation Based on a 3D Deep Neural Network Using Adversarial Loss for Prior Shape Constraint. 9, 0
- 681 Voxel-wise intermodal coupling analysis of two or more modalities using local covariance decomposition. 0
- 680 Impact of surgically assisted rapid mandibular expansion on the temporomandibular joint. **2022**,
- 679 A Machine Learning and Radiomics Approach in Lung Cancer for Predicting Histological Subtype. **2022**, 12, 5829 2
- 678 Automated analysis of low-field brain MRI in cerebral malaria.
- 677 Usefulness of Hospital Admission Chest X-ray Score for Predicting Mortality and ICU Admission in COVID-19 Patients. **2022**, 11, 3548
- 676 A new advanced MRI biomarker for remyelinated lesions in Multiple Sclerosis. 1
- 675 NISNet3D: Three-Dimensional Nuclear Synthesis and Instance Segmentation for Fluorescence Microscopy Images. 0
- 674 Comparative study of radiologists vs machine learning in differentiating biopsy-proven pseudoprogression and true progression in diffuse gliomas. **2022**, 100088

- 673 Application of a TEG-Platelet Mapping Algorithm to Guide Reversal of Antiplatelet Agents in Adults with Mild-to-Moderate Traumatic Brain Injury: An Observational Pilot Study.
- 672 Prediction of abdominal aortic aneurysm growth by artificial intelligence taking into account clinical, biologic, morphologic, and biomechanical variables. 170853812210778 ○
- 671 Segmentation Only Uses Sparse Annotations: Unified Weakly and Semi-Supervised Learning in Medical Images. **2022**, 102515 ○
- 670 Limited utility of structural MRI to identify the epileptogenic zone in young children with tuberous sclerosis. ○
- 669 Paramagnetic rim lesions are associated with pathogenic CSF profiles and worse clinical status in multiple sclerosis: A retrospective cross-sectional study. 135245852211029 3
- 668 Enhancing the REMBRANDT MRI collection with expert segmentation labels and quantitative radiomic features. **2022**, 9,
- 667 Combining High-Resolution Hard X-ray Tomography and Histology for Stem Cell-Mediated Distraction Osteogenesis. **2022**, 12, 6286 ○
- 666 Chronic clomipramine treatment increases hippocampal volume in rats exposed to chronic unpredictable mild stress. **2022**, 12, ○
- 665 Role of diffusion-weighted MRI in recurrent rectal cancer treated with carbon ion radiotherapy.
- 664 Volumetric Analysis of the Piriform Cortex in Temporal Lobe Epilepsy. **2022**, 106971 ○
- 663 Brain disconnectome mapping derived from white matter lesions and serum neurofilament light levels in multiple sclerosis: A longitudinal multicenter study. **2022**, 103099 ○
- 662 FetalGAN: Automated Segmentation of Fetal Functional Brain MRI Using Deep Generative Adversarial Learning and Multi-Scale 3D U-Net. 16, ○
- 661 Evidence for grid-cell-related activity in the time domain.
- 660 Diffusion-weighted imaging as an imaging biomarker for assessing survival of patients with intrahepatic mass-forming cholangiocarcinoma.
- 659 High-resolution hippocampal DTI of Mesial Temporal Sclerosis in Refractory Epilepsy. ○
- 658 A large, curated, open-source stroke neuroimaging dataset to improve lesion segmentation algorithms. **2022**, 9, 1
- 657 Image Downsampling Expedited Adaptive Least-squares (IDEAL) fitting improves intravoxel incoherent motion (IVIM) analysis in the human kidney.
- 656 Initial Displacement and Stress Distribution of Upper Central Incisor Extrusion with Clear Aligners and Various Shapes of Composite Attachments Using the Finite Element Method. **2022**, 10, 114 1

- 655 Increased brain volumetric measurement precision from multi-site 3D T1-weighted 3 T magnetic resonance imaging by correcting geometric distortions. **2022**,
- 654 Lorentzian-Corrected Apparent Exchange-Dependent Relaxation (LAREX) fPlot Analysis: An Adaptation for qCEST in a Multi-Pool System: Comprehensive In Silico, In Situ, and In Vivo Studies. **2022**, 23, 6920 1
- 653 Characterizing the neurological phenotype of the hyperinsulinism hyperammonemia syndrome. **2022**, 17, 0
- 652 Multilevel atlas comparisons reveal divergent evolution of the primate brain. **2022**, 119, 0
- 651 Multisite Reproducibility of QSM and R^2 * in Deep Gray Matter at 3T Using Locally-Optimized Sequences in 24 Traveling Heads.
- 650 Validation of a new coil array tailored for dog functional magnetic resonance imaging (fMRI) studies.
- 649 Multicenter assessment of augmented reality registration methods for image-guided interventions. 5
- 648 Flank pain has a significant adverse impact on quality of life in ADPKD: the CYSTic-QoL study. 0
- 647 From Seeing to Simulating: A Survey of Imaging Techniques and Spatially-Resolved Data for Developing Multiscale Computational Models of Liver Regeneration. 2, 0
- 646 Regional left ventricular endocardial strains estimated from low-dose 4DCT: comparison with cardiac magnetic resonance feature tracking. 0
- 645 Altered Coupling Between Cerebral Blood Flow and Voxel-Mirrored Homotopic Connectivity Affects Stroke-Induced Speech Comprehension Deficits. 14,
- 644 Usefulness of Noncontrast MRI-Based Radiomics Combined Clinic Biomarkers in Stratification of Liver Fibrosis. **2022**, 2022, 1-9 0
- 643 Worse Tibiofemoral Cartilage Composition is Associated with Insufficient Gait Kinetics Following ACL Reconstruction. Publish Ahead of Print, 0
- 642 Modality-Specific Segmentation Network for Lung Tumor Segmentation in PET-CT Images. **2022**, 1-12 0
- 641 Neuroimaging, Neural Population Models for. **2022**, 2256-2281
- 640 Deep Liver Lesion AI System: A Liver Lesion Diagnostic System Using Deep Learning in Multiphase CT. **2022**, 237-246
- 639 A Real-Time Porosity Prediction Model for Laser Powder Bed Fusion Builds.
- 638 Pattern of Recurrence of Glioblastoma Versus Grade 4 IDH-Mutant Astrocytoma Following Chemoradiation: A Retrospective Matched-Cohort Analysis. **2022**, 21, 153303382211096 0

- 637 Prophylactic evaluation of verubecestat on disease- and symptom-modifying effects in 5XFAD mice. **2022**, 8,
- 636 Sensitivity of portable low-field magnetic resonance imaging for multiple sclerosis lesions. **2022**, 35, 103101 o
- 635 Image-guided in-Vivo Needle-Based Confocal Laser Endomicroscopy in the Prostate: Safety and Feasibility Study in 2 Patients. **2022**, 21, 153303382210931
- 634 Three-Dimensional Atlas of the Human Amygdala Subnuclei Constructed Using Immunohistochemical and Ultrahigh-Field Magnetic Resonance Imaging Data. **2022**, 227-236 1
- 633 Integration of 3-D Nuclear Imaging in 3-D Mapping System for Ventricular Tachycardia Ablation in Patients with Implanted Devices: Perfusion/Voltage Retrospective Assessment of Scar Location. **2022**,
- 632 3D modeling and comparative analysis of the double arcus aorta case. o
- 631 Altered excitability of motor neuron pathways after stroke: more than upper motor neuron impairments. svn-2022-001568
- 630 The design and application of a diffusion tensor informed finite-element model for exploration of uniaxially prestressed muscle architecture in magnetic resonance imaging. 1
- 629 Multi-echo quantitative susceptibility mapping: how to combine echoes for accuracy and precision at 3 Tesla.
- 628 Attention drives human numerosity-selective responses. **2022**, 39, 111005 o
- 627 Establish a New Diagnosis of Sarcopenia Based on Extracted Radiomic Features to Predict Prognosis of Patients With Gastric Cancer. 9, o
- 626 PhiPipe: a multi-modal MRI data processing pipeline with test-retest reliability and predictive validity assessments.
- 625 FECC-Net: A Novel Feature Enhancement and Context Capture Network Based on Brain MRI Images for Lesion Segmentation. **2022**, 12, 765 o
- 624 Are We There Yet? The Value of Deep Learning in a Multicenter Setting for Response Prediction of Locally Advanced Rectal Cancer to Neoadjuvant Chemoradiotherapy. **2022**, 12, 1601
- 623 Varus stress MRI in the refined assessment of the posterolateral corner of the knee joint. **2022**, 12,
- 622 Retrospective motion correction in fetal MRI for clinical applications: existing methods, applications and integration into clinical practice. o
- 621 Mouse model of selective cryolipolysis.
- 620 Morphology and phylogenetic significance of the thoracic muscles in Psocodea (Insecta: Paraneoptera).

- 619 A groupwise registration and tractography framework for cardiac myofiber architecture description by diffusion MRI: An application to the ventricular junctions. **2022**, 17, e0271279
- 618 Morphological changes of Intervertebral Disc detectable by T2-weighted MRI and its correlation with curve severity in Adolescent Idiopathic Scoliosis. **2022**, 23, o
- 617 Integrated analysis of Wnt signalling system component gene expression.
- 616 A Hitchhiker's Guide through the Bio-image Analysis Software Universe. 1
- 615 CDFRegNet: A Cross-domain Fusion Registration Network for CT-to-CBCT Image Registration. **2022**, 107025 o
- 614 Design and validation of a finite element model of the aponeurotic and free Achilles tendon.
- 613 Alterations of NK Cell Phenotype During Pregnancy in Multiple Sclerosis. 13,
- 612 Combined whole-lesion radiomic and iodine analysis for differentiation of pulmonary tumors. **2022**, 12, o
- 611 Intracranial Vessel Wall Segmentation with Deep Learning using a Novel Tiered Loss Function Incorporating Class Inclusion. o
- 610 Factors Affecting the Success of Endodontic Microsurgery: A Cone-Beam Computed Tomography Study. **2022**, 11, 3991 o
- 609 Biomechanics of Transcatheter Aortic Valve Implant. **2022**, 9, 299
- 608 Exploiting the Dixon Method for a Robust Breast and Fibro-Glandular Tissue Segmentation in Breast MRI. **2022**, 12, 1690
- 607 Assessing the inflammatory severity of the terminal ileum in Crohn disease using radiomics based on MRI. **2022**, 22, o
- 606 Preoperative Prediction of Lymph Node Metastasis of Pancreatic Ductal Adenocarcinoma Based on a Radiomics Nomogram of Dual-Parametric MRI Imaging. 12, o
- 605 Development and Validation of a CT-Based Radiomics Nomogram in Patients With Anterior Mediastinal Mass: Individualized Options for Preoperative Patients. 12,
- 604 Diagnosis of Marginal Infiltration in Soft Tissue Sarcoma by Radiomics Approach Using T2-Weighted Dixon Sequence.
- 603 Three-Dimensional Volume Calculation of Intrachoroidal Cavitation Using Deep-Learning-Based Noise Reduction of Optical Coherence Tomography. **2022**, 11, 1
- 602 DBB - A Distorted Brain Benchmark for Automatic Tissue Segmentation in Paediatric Patients. *NeuroImage*, **2022**, 119486 7.9 o

601 The Necessity of Magnetic Resonance Imaging in Congenital Diaphragmatic Hernia. **2022**, 12, 1733

600 Dosing Transcranial Magnetic Stimulation of the Primary Motor and Dorsolateral Prefrontal Cortices With Multi-Scale Modeling. 16, o

599 Through a Dog's Eyes: fMRI Decoding of Naturalistic Videos from Dog Cortex.

598 Thrombus imaging characteristics within acute ischemic stroke: similarities and interdependence. *neurintsurg*-2022-01 1

597 Combining advanced magnetic resonance imaging (MRI) with finite element (FE) analysis for characterising subject-specific injury patterns in the brain after traumatic brain injury. o

596 The neuronal logic of how internal states control food choice. o

595 Ventricular volume in relation to lumbar CSF levels of amyloid- β 42, tau and phosphorylated tau in iNPH, is there a dilution effect?. **2022**, 19, 1

594 Toward deep observation: A systematic survey on artificial intelligence techniques to monitor fetus via ultrasound images. **2022**, 25, 104713 1

593 Real-time neurofeedback to alter interpretations of a naturalistic narrative. **2022**, 2, 100111

592 Statistical asymmetry analysis of volumetric MRI and FDG PET in temporal lobe epilepsy. **2022**, 134, 108810 o

591 Inconsistencies in atlas-based volumetric measures of the human nucleus basalis of Meynert: A need for high-resolution alternatives. *NeuroImage*, **2022**, 259, 119421 7.9 o

590 Cardiac segmentation on late gadolinium enhancement MRI: A benchmark study from multi-sequence cardiac MR segmentation challenge. **2022**, 81, 102528 1

589 Early brainstem hemorrhage progression: multi-sequence magnetic resonance imaging and histopathology. **2023**, 18, 170

588 Tandem Mass Tag-based proteomics analysis reveals the vital role of inflammation in traumatic brain injury in a mouse model. **2023**, 18, 155 o

587 3D Centroidnet: Nuclei Centroid Detection with Vector Flow Voting. o

586 Outcome Prediction Based on Automatically Extracted Infarct Core Image Features in Patients with Acute Ischemic Stroke. **2022**, 12, 1786 o

585 Transformer based tooth classification from cone-beam computed tomography for dental charting. **2022**, 105880

584 Endothelial cell death after ionizing radiation does not impair vascular structure in mouse tumor models. o

- 583 p53 restoration in small cell lung cancer identifies a latent Cyclophilin-dependent necrosis mechanism.
- 582 Virtual high-count PET image generation using a deep-learning method. ○
- 581 Task Relevance Driven Adversarial Learning for Simultaneous Detection, Size Grading, and Quantification of Hepatocellular Carcinoma via Integrating Multi-modality MRI. **2022**, 102554 ○
- 580 Gadolinium-free Magnetic Resonance Imaging of the Liver via an Oatp1-Targeted Manganese(III) Porphyrin. **2022**, 65, 9846-9857 ○
- 579 Delta-Radiomics Based on Dynamic Contrast-Enhanced MRI Predicts Pathologic Complete Response in Breast Cancer Patients Treated with Neoadjuvant Chemotherapy. **2022**, 14, 3515 ○
- 578 Regional brain volume prior to treatment is linked to outcome after cognitive rehabilitation in traumatic brain injury. **2022**, 103126
- 577 Optimization of Deep Learning Based Brain Extraction in MRI for Low Resource Environments. **2022**, 151-167
- 576 Deep Learning Assisted Segmentation and Detection for Intracranial Aneurysms Magnetic Resonance T1 Imaging: Development and Validation.
- 575 Deep learning-based automated segmentation of resection cavities on postsurgical epilepsy MRI. **2022**, 36, 103154
- 574 Forensic Anthropology. **2022**, 1561-1573
- 573 Automated needle localisation for electric field computation during an electroporation ablation. **2022**,
- 572 An Ensemble Learning and Slice Fusion Strategy for Three-Dimensional Nuclei Instance Segmentation. **2022**, ○
- 571 The University of Pennsylvania glioblastoma (UPenn-GBM) cohort: advanced MRI, clinical, genomics, & radiomics. **2022**, 9, ○
- 570 Skeletomuscular Atlas and Deep Homology of a Metamorphosing Genitalic Appendage in a Flat-Backed Millipede (Polydesmida: Polydesmidae: Pseudopolydesmus). **2022**, 6, ○
- 569 Loss of aquaporin-4 results in glymphatic system dysfunction via brain-wide interstitial fluid stagnation.
- 568 Automatic segmentation of white matter hyperintensities in routine clinical brain MRI by 2D VB-Net: A large-scale study. 14, ○
- 567 Detection of left ventricular wall motion abnormalities from volume rendering of 4DCT cardiac angiograms using deep learning. 9, ○
- 566 Comparative Multicentric Evaluation of Inter-Observer Variability in Manual and Automatic Segmentation of Neuroblastic Tumors in Magnetic Resonance Images. **2022**, 14, 3648 2

565 Development of a vendor neutral MRI distortion quality assurance workflow.

564 Expert tumor annotations and radiomics for locally advanced breast cancer in DCE-MRI for ACRIN 6657/I-SPY1. **2022**, 9,

1

563 Loading of the Spine in Low Back Pain Patients Does Not Induce MRI Changes in Modic Lesions: A Prospective Clinical Study. **2022**, 12, 1815

562 Is intracranial volume a risk factor for IDH-mutant low-grade glioma? A case-control study.

561 Long-term three-dimensional condylar remodeling during presurgical orthodontics and after orthognathic surgery of mandibular retrognathia with high mandibular plane angle.

560 80 Hz but not 40 Hz, transcranial alternating current stimulation of 80 Hz over right intraparietal sulcus increases visuospatial working memory capacity. **2022**, 12,

0

559 Longitudinal clinical study of patients with iron rim lesions in multiple sclerosis. 135245852211147

3

558 Evaluation of a hybrid pipeline for automated segmentation of solid lesions based on mathematical algorithms and deep learning. **2022**, 12,

557 The association between lumbar paraspinal muscle functional cross-sectional area on MRI and regional volumetric bone mineral density measured by quantitative computed tomography.

556 Evaluation of a novel 8-channel RX coil for speech production MRI at 0.55 T.

555 Early Visual Areas are Activated during Object Recognition in Emerging Images.

554 Relation between retina, cognition and brain volumes in MS: a consequence of asymptomatic optic nerve lesions.

553 Trimethylamine N-oxide promotes demyelination in spontaneous hypertension rats through enhancing pyroptosis of oligodendrocytes. 14,

0

552 Phantom-based evaluation of yttrium-90 datasets using Biograph Vision Quadra.

551 Qualitative and quantitative detectability of hypertrophic olivary degeneration in T2, FLAIR, PD, and DTI: A prospective MRI study. 13,

550 Identification of high-risk intracranial plaques with 3D high-resolution magnetic resonance imaging-based radiomics and machine learning.

0

549 Competition between Associations in Memory. 1-24

548 Brain Differences in Adolescents Living With Perinatally Acquired HIV Compared to Adoption Status Match Controls: A Cross-Sectional Study. 10.1212/WNL.0000000000200946

- 547 A companion to the preclinical common data elements and case report forms for in vivo rodent Neuroimaging. A report of the TASK3-WG3 Neuroimaging Working Group of the ILAE/AES Joint Translational Task Force.
- 546 The effect of age on psoas and paraspinal muscle morphology in patients undergoing posterior lumbar fusion surgery.
- 545 Machine learning for the automatic assessment of aortic rotational flow and wall shear stress from 4D flow cardiac magnetic resonance imaging. o
- 544 DENND5A epileptic encephalopathy features global developmental delay, seizures and ventriculomegaly.
- 543 Accuracy of CT perfusion ischemic core volume and location estimation: A comparison between four ischemic core estimation approaches using syngo.via. **2022**, 17, e0272276 o
- 542 Application of A U-Net for Map-like Segmentation and Classification of Discontinuous Fibrosis Distribution in Gd-EOB-DTPA-Enhanced Liver MRI. **2022**, 12, 1938
- 541 Rib Fracture Detection with Dual-Attention Enhanced U-Net. **2022**, 2022, 1-13
- 540 Modeling the early stages of Alzheimer's disease by administering intracerebroventricular injections of human native A β oligomers to rats. **2022**, 10, o
- 539 Multimodal imaging shows fibrosis architecture and action potential dispersion are predictors of arrhythmic risk in spontaneous hypertensive rats. o
- 538 Cumulative Exposure to Oxidized Low-Density Lipoprotein is a Potential Predictor for Prognosis in Acute Ischemic Stroke: A Cohort Study.
- 537 Automatic Detection of Periapical Osteolytic Lesions on CBCT Using Deep CNNs. **2022**, o
- 536 Monitoring longitudinal disease progression in a novel murine Kit tumor model using high-field MRI. **2022**, 12, o
- 535 Artificial intelligence in the radiomic analysis of glioblastomas: A review, taxonomy, and perspective. 12, o
- 534 Volumetric measurement of intracranial meningiomas: a comparison between linear, planimetric, and machine learning with multiparametric voxel-based morphometry methods.
- 533 Effect of GBCA Use on Detection and Diagnostic Performance of the Central Vein Sign: Evaluation Using a 3T FLAIR* Sequence in Patients With Suspected Multiple Sclerosis. 1
- 532 Computer-aided diagnostic models to classify lymph node metastasis and lymphoma involvement in enlarged cervical lymph nodes using PET/CT. o
- 531 Ultrasound Radiomics-Based Logistic Regression Model to Differentiate Between Benign and Malignant Breast Nodules.
- 530 Ablation of Tmem65 Causes Lethal Mitochondrial Encephalomyopathy in Mouse.

- 529 Acquisition and processing methods of whole-brain layer-fMRI VASO and BOLD: The Kenshu dataset. ○
- 528 Combine unlabeled with labeled MR images to measure acute ischemic stroke lesion by stepwise learning.
- 527 Biallelic PAX5 mutations cause hypogammaglobulinemia, sensorimotor deficits, and autism spectrum disorder. **2022**, 219, ○
- 526 Automatic Segmentation and Quantitative Assessment of Stroke Lesions on MR Images. **2022**, 12, 2055 ○
- 525 Validation of SART 3.5D algorithm for cerebrovascular dynamics and artery vs vein classification in presurgical 3D digital subtraction angiographies.
- 524 Validating the accuracy of multispectral metal artifact suppressed diffusion-weighted imaging. ○
- 523 Evaluation of KRASG12C Inhibitor Responses in Novel Murine KRASG12C Lung Cancer Cell Line Models. ○
- 522 Internal calibration for opportunistic computed tomography muscle density analysis.
- 521 A general biomechanical model for the relation between bite force and mandibular opening angle in arthropods. 1
- 520 Towards Automated Brain Aneurysm Detection in TOF-MRA: Open Data, Weak Labels, and Anatomical Knowledge.
- 519 Imaging the columnar functional organization of human area MT+ to axis-of-motion stimuli using VASO at 7 Tesla.
- 518 Integrated 3d flow-based multi-atlas brain structure segmentation. **2022**, 17, e0270339
- 517 Assessing mild cognitive impairment using object-location memory in immersive virtual environments. **2022**, 32, 660-678 ○
- 516 Mitigating Bias in Radiology Machine Learning: 1. Data Handling. **2022**, 4, 1
- 515 Validation of perihematoma edema expansion as a new imaging biomarker to predict clinical outcome in patients with intracerebral hemorrhage. **2022**, 31, 106692
- 514 Automated quantification of airway wall thickness on chest CT using retina U-Nets [Performance evaluation and application to a large cohort of chest CTs of COPD patients. **2022**, 155, 110460 ○
- 513 Sensory system-specific associations between brain structure and balance. **2022**, 119, 102-116
- 512 Lysophosphatidic acid as a CSF lipid in posthemorrhagic hydrocephalus that drives CSF accumulation via TRPV4-induced hyperactivation of NKCC1. **2022**, 19, 2

511	CLAIRE: Parallelized Diffeomorphic Image Registration for Large-Scale Biomedical Imaging Applications. 2022 , 8, 251	0
510	Change in T2* measurements of placenta and fetal organs during Braxton Hicks contractions. 2022 , 128, 69-71	0
509	Rapid artificial intelligence solutions in a pandemic: The COVID-19-20 Lung CT Lesion Segmentation Challenge. 2022 , 82, 102605	2
508	Predicting treatment-specific lesion outcomes in acute ischemic stroke from 4D CT perfusion imaging using spatio-temporal convolutional neural networks. 2022 , 82, 102610	0
507	Biomechanics optimisation of the laminoplasty groove size and position: A numerical study. 2022 , 105, 45-50	0
506	Computational assessment of upper airway muscular activity in obstructive sleep apnea [In vitro validation. 2022 , 144, 111304	0
505	Fast and Low-GPU-memory abdomen CT organ segmentation: The FLARE challenge. 2022 , 82, 102616	17
504	Associations between locus coeruleus MRI contrast and physiological responses to acute stress in younger and older adults. 2022 , 1796, 148070	0
503	Multi-scale multi-hierarchy attention convolutional neural network for fetal brain extraction. 2023 , 133, 109029	0
502	CTooth+: A Large-Scale Dental Cone Beam Computed Tomography Dataset and Benchmark for Tooth Volume Segmentation. 2022 , 64-73	0
501	Forward Model of Rat Electroencephalogram: Comparative Study of Numerical Simulations With Measurements on Rat Head Phantoms. 2022 , 10, 92023-92035	0
500	DeepCRC: Colorectum and Colorectal Cancer Segmentation in CT Scans via Deep Colorectal Coordinate Transform. 2022 , 564-573	0
499	Precontouring Plates for MIS Bilateral Femur Osteosynthesis Using a Patient-Specific 3D Printed Model. 2022 , 12,	0
498	Hybrid Spatio-Temporal Transformer Network for Predicting Ischemic Stroke Lesion Outcomes from 4D CT Perfusion Imaging. 2022 , 644-654	0
497	Deep Reinforcement Learning for Detection of Inner Ear Abnormal Anatomy in Computed Tomography. 2022 , 697-706	0
496	Automated Multi-class Fetal Cardiac Vessel Segmentation in Aortic Arch Anomalies Using T2-Weighted 3D Fetal MRI. 2022 , 82-93	0
495	DeepEdit: Deep Editable Learning for Interactive Segmentation of 3D Medical Images. 2022 , 11-21	1
494	Building a Bioimage Analysis Workflow Using Deep Learning. 2022 , 59-88	1

493	Early volumetric, perfusion, and diffusion MRI changes after mutant isocitrate dehydrogenase (IDH) inhibitor treatment in IDH1-mutant gliomas. 2022 , 4,	0
492	Numerical assessment of aortic valve coaptation after neo-cuspidation procedure. 2022 , 15, 369	0
491	Automatic Quality Assessment of First Trimester Crown-Rump-Length Ultrasound Images. 2022 , 172-182	0
490	Software for Building an Office-Based 3D Printing Lab. 2022 , 23-32	0
489	CTooth: A Fully Annotated 3D Dataset and Benchmark for Tooth Volume Segmentation on Cone Beam Computed Tomography Images. 2022 , 191-200	1
488	MRI predictors of pharmacotherapy response in major depressive disorder. 2022 , 36, 103157	1
487	References. 2022 , 13-14	0
486	A Deep-Learning Lesion Segmentation Model that Addresses Class Imbalance and Expected Low Probability Tissue Abnormalities in Pre and Postoperative Liver MRI. 2022 , 398-411	0
485	Hippocampal Growth is Altered from Term Equivalence to One Year of Age in Preterm Born Infants.	0
484	Scribble-Supervised Medical Image Segmentation via Dual-Branch Network and Dynamically Mixed Pseudo Labels Supervision. 2022 , 528-538	3
483	Presurgical predictors of early cognitive outcome after brain tumor resection in glioma patients. 2022 , 36, 103219	0
482	Interactive Segmentation and Visualization for Tiny Objects in Multi-megapixel Images. 2022 ,	0
481	An Optimized U-Net for Unbalanced Multi-Organ Segmentation. 2022 ,	0
480	Associations of maternal and foetoplacental factors with prehypertension/hypertension in early childhood. 2022 , 40, 2171-2179	0
479	Structural Changes in the Arcuate Fasciculus and Recovery of Post-stroke Aphasia: A 6-Month Follow-up Study using Diffusion Tensor Imaging. 2022 , 36, 633-644	0
478	Quantitative susceptibility atlas construction in Montreal Neurological Institute space: towards histological-consistent iron-rich deep brain nucleus subregion identification.	0
477	The Holistic Perspective of the INCISIVE Project Artificial Intelligence in Screening Mammography. 2022 , 12, 8755	1
476	Multimodal integration of radiology, pathology and genomics for prediction of response to PD-(L)1 blockade in patients with non-small cell lung cancer.	2

- 475 T2-weighted MRI-based radiomics for discriminating between benign and borderline epithelial ovarian tumors: a multicenter study. **2022**, 13, ○
- 474 A Comparison of MRI Quantitative Susceptibility Mapping and TRUST-Based Measures of Brain Venous Oxygen Saturation in Sickle Cell Anaemia. 13, ○
- 473 Single-cell brain organoid screening identifies developmental defects in autism. ○
- 472 Fully automated detection and localization of clinically significant prostate cancer on MR images using a cascaded convolutional neural network. 12, ○
- 471 SlicerHeart: An open-source computing platform for cardiac image analysis and modeling. 9, 1
- 470 Volumetric measurement of intracranial meningiomas: a comparison between linear, planimetric, and machine learning with multiparametric voxel-based morphometry methods. ○
- 469 Use of 3D ultrasound to characterise temporal changes in thyroid nodules: an in vitro study. ○
- 468 Hybrid imaging with [68Ga]PSMA-11 PET-CT and PET-MRI in biochemically recurrent prostate cancer. **2022**, 22, ○
- 467 Volumetric Pancreas Segmentation on Computed Tomography: Accuracy and Efficiency of a Convolutional Neural Network Versus Manual Segmentation in 3D Slicer in the Context of Interreader Variability of Expert Radiologists. Publish Ahead of Print, ○
- 466 A comparative study of the superior longitudinal fasciculus subdivisions between neonates and young adults. ○
- 465 Use of Magnetic Resonance Imaging to Quantify Fat and Steatosis in the Pancreas in Patients after Bariatric Surgery: a Retrospective Study. ○
- 464 In vivo 2-Hydroxyglutarate Monitoring With Edited MR Spectroscopy for the Follow-up of IDH-Mutant Diffuse Gliomas: The IDASPE Prospective Study. 10.1212/WNL.0000000000201137 ○
- 463 Active Contour Extension Basing on Haralick Texture Features, Multi-gene Genetic Programming, and Block Matching to Segment Thyroid in 3D Ultrasound Images. ○
- 462 Semantic Segmentation of Spontaneous Intracerebral Hemorrhage, Intraventricular Hemorrhage, and Associated Edema on CT Images Using Deep Learning. ○
- 461 3D Ground Truth Annotations of Nuclei in 3D Microscopy Volumes. ○
- 460 Developing a Predictive Grading Model for Children with Gliomas Based on Diffusion Kurtosis Imaging Metrics: Accuracy and Clinical Correlations with Patient Survival. **2022**, 14, 4778 ○
- 459 Estimating external tissue support parameters with fluid-structure interaction models from 4D ultrasound of murine thoracic aortae. ○
- 458 Radiomics-Based Machine Learning to Predict Recurrence in Glioma Patients Using Magnetic Resonance Imaging. Publish Ahead of Print, ○

- 457 Image-guided pelvic exenteration-preoperative and intraoperative strategies. **2022**, 0
- 456 Evaluation of Sodium Relaxation Times and Concentrations in the Achilles Tendon Using MRI. **2022**, 23, 10890 1
- 455 Wrist Bone Motion during Flexion-Extension and Radial-Ulnar Deviation: An MRI Study. **2022**, 12, 1458 0
- 454 Usefulness of deep learning-based noise reduction for 1.5 T MRI brain images. **2022**, 0
- 453 Pulsatile lavage systems and their potential to penetrate soft tissue. 0
- 452 Reorganization in the macaque interoceptive-allostatic network following anterior cingulate cortex damage. 0
- 451 The potential risk factors of early-onset post-stroke depression from immuno-inflammatory perspective. 13, 0
- 450 Tumor Treating Fields (TTFields) Reversibly Permeabilize the BloodBrain Barrier In Vitro and In Vivo. **2022**, 12, 1348 1
- 449 Masseter muscle volume as a disease marker in adult-onset myotonic dystrophy type 1. **2022**, 0
- 448 CSM-net: Automatic joint segmentation of and lumen in carotid artery ultrasound images. **2022**, 106119 1
- 447 A Steerable and Electromagnetically Tracked Catheter: Navigation Performance Compared With Image Fusion in a Swine Model. 152660282211234 0
- 446 Radiomics Models Based on Magnetic Resonance Imaging for Prediction of the Response to Bortezomib-Based Therapy in Patients with Multiple Myeloma. **2022**, 2022, 1-9 0
- 445 Ability of Radiomics Versus Humans in Predicting First-Pass Effect After Endovascular Treatment in the ESCAPE-NA1 Trial. 1
- 444 Lesion-Specific Metabolic Alterations in Relapsing-Remitting Multiple Sclerosis Via 7 T Magnetic Resonance Spectroscopic Imaging. Publish Ahead of Print, 0
- 443 Heterogeneous migration of neuronal progenitors to the insula shapes the human brain. 0
- 442 The federated tumor segmentation (FeTS) tool: an open-source solution to further solid tumor research. 0
- 441 An Introductory Module in Medical Image Segmentation for BME Students. 0
- 440 SPECT/CT imaging reveals CNS-wide modulation of glymphatic cerebrospinal fluid flow by systemic hypertonic saline. **2022**, 105250 0

- 439 Automated detection and analysis of subdural hematomas using a machine learning algorithm. **2022**, 1-8 ○
- 438 Mapping hippocampal glutamate in mesial temporal lobe epilepsy with glutamate weighted CEST (GluCEST) imaging. ○
- 437 Evidence of nerve hypertrophy in patients with inclusion body myositis on lower limb magnetic resonance imaging. ○
- 436 WORD: A large scale dataset, benchmark and clinical applicable study for abdominal organ segmentation from CT image. **2022**, 102642 ○
- 435 Radiomic study on preoperative multi-modal magnetic resonance images identifies IDH -mutant TERT promoter-mutant gliomas. ○
- 434 Serum neurofilament light chain levels are correlated with the infarct volume in patients with acute ischemic stroke. **2022**, 101, e30849 ○
- 433 Risk factors of late lesion growth after acute ischemic stroke treatment. 13, ○
- 432 Predicting tracheal work of breathing in neonates based on radiological and pulmonary measurements. **2022**, 133, 893-901 ○
- 431 Development and model form assessment of an automatic subject-specific vertebra reconstruction method. **2022**, 106158 ○
- 430 Modeling the musculoskeletal system of an insect thorax for flapping flight. **2022**, 17, 066010 ○
- 429 Ablation of Apparent Diffusion Coefficient Hyperintensity Clusters in Mesial Temporal Lobe Epilepsy Improves Seizure Outcomes after Laser Interstitial Thermal Therapy. ○
- 428 Independent effects of emotional arousal and reward anticipation on episodic memory formation. ○
- 427 Four-dimensional fetal cardiac imaging in a cohort of fetuses with suspected congenital heart disease. ○
- 426 Müller cell degeneration and microglial dysfunction in the Alzheimer's retina. **2022**, 10, 1
- 425 Machine learning evaluation of LV outflow obstruction in hypertrophic cardiomyopathy using three-chamber cardiovascular magnetic resonance. ○
- 424 Whole-lung finite-element models for mechanical ventilation and respiratory research applications. 13, ○
- 423 A Hybrid Catheter Localisation Framework in Echocardiography Based on Electromagnetic Tracking and Deep Learning Segmentation. **2022**, 2022, 1-9 ○
- 422 Quantitative vs Qualitative Muscle MRI: Imaging Biomarker in Patients with Oculopharyngeal Muscular Dystrophy (OPMD). **2022**, ○

421	Analysis of Stress Distribution of Custom Fitted Femoral Component Knee Implant for Asian Anatomy. 2023 , 585-592	0
420	Comprehensive volumetric phenotyping of the neonatal brain in Down syndrome.	0
419	The human splenic microcirculation is entirely open as shown by 3D models in virtual reality. 2022 , 12,	0
418	Use of Visual Information by Ant Species Occurring in Similar Urban Anthropogenic Environments. 2022 , 39,	0
417	Mechanics-informed snakes isogeometric analysis (MISIGA): an image-based method for the estimation of local deformation and strain in blood vessels.	0
416	Maternal adverse childhood experiences and infant subcortical brain volume. 2022 , 21, 100487	0
415	Deep Learning-Based Segmentation of Pleural Effusion from Ultrasound Using Coordinate Convolutions. 2022 , 168-177	0
414	Learning-Based Detection of MYCN Amplification in Clinical Neuroblastoma Patients: A Pilot Study. 2022 , 89-97	0
413	Intrasubject subcortical quantitative referencing to boost MRI sensitivity to Parkinson's disease. 2022 , 36, 103231	0
412	Validation and comparison of volume measurements using 1 multidetector computed tomography and 5 cone-beam computed tomography protocols: An in vitro study. 52,	0
411	HDR Brachytherapy Planning using Active Needles - Preliminary Investigation on Dose Planning. 2022 ,	0
410	Assessment of Morphologic Change of Mandibular Condyle in Temporomandibular Joint Osteoarthritis Patients with Stabilization Splint Therapy: A Pilot Study. 2022 , 10, 1939	0
409	Internal calibration for opportunistic computed tomography muscle density analysis. 2022 , 17, e0273203	0
408	Application of a Deep Learning Approach to Analyze Large-Scale MRI Data of the Spine. 2022 , 10, 2132	0
407	Radiomics in PI-RADS 3 Multiparametric MRI for Prostate Cancer Identification: Literature Models Re-Implementation and Proposal of a Clinical Radiological Model. 2022 , 11, 6304	0
406	Automatic multi-anatomical skull structure segmentation of cone-beam computed tomography scans using 3D UNETR. 2022 , 17, e0275033	2
405	Imaging Characteristics of Choroid Plexuses in Presymptomatic Multiple Sclerosis. 2022 , 9, e200026	1
404	Feasibility of awake brain surgery in glioblastoma patients with severe aphasia: Five case illustrations. 1-20	0

403	Non-invasive measurement of tumor immune microenvironment and prediction of survival and chemotherapeutic benefits from 18F fluorodeoxyglucose PET/CT images in gastric cancer. 13,	0
402	Preoperative computed tomography volumetry and graft weight estimation of left lateral segment in pediatric living donor liver transplantation.	0
401	Characterization of the blood oxygen level dependent hemodynamic response function in human subcortical regions with high spatiotemporal resolution. 16,	1
400	Development and validation of subject-specific 3D human head models based on a nonlinear visco-hyperelastic constitutive framework. 2022, 19,	0
399	In silico modeling for personalized stenting in aortic coarctation. 2022, 16, 2056-2073	0
398	Transversal functional connectivity and scene-specific processing in the human entorhinal-hippocampal circuitry. 11,	1
397	Entorhinal grid-like codes and time-locked network dynamics track others navigating through space.	0
396	3D Single-Breath Chemical Shift Imaging Hyperpolarized Xe-129 MRI of Healthy, CF, IPF, and COPD Subjects. 2022, 8, 2574-2587	0
395	Novel EGFR-Mutant Mouse Models of Lung Adenocarcinoma Reveal Adaptive Immunity Requirement for Durable Osimertinib Response.	0
394	Longitudinal brain age prediction and cognitive function after stroke. 2022,	0
393	Structural Changes in the Cervicomedullary Junction in Adult Chiari Patients. 2022,	0
392	Segmentation techniques of brain arteriovenous malformations for 3D visualization: a systematic review.	2
391	Molecular imaging of the brainHeart axis provides insights into cardiac dysfunction after cerebral ischemia. 2022, 117,	0
390	3D synchrotron imaging of muscle tissues at different atrophic stages in stroke and spinal cord injury: a proof-of-concept study. 2022, 12,	0
389	Post Traumatic Seizure Classification with Missing Data using Multimodal Machine Learning on dMRI, EEG, and fMRI.	0
388	Computational Study of Magnetic Particle Motion inside the Nasal Cavity under the Impact of an External Magnetic Field for Biomedical Applications. 2022, 13, 1816	0
387	Cross modality fusion for modality-specific lung tumor segmentation in PET-CT images.	0
386	Dissecting the functional contributions of different neuronal subtypes in the dorsal striatum to perseverative behaviour in ephrin-A2/A5-/-mice.	0

- 385 Semisupervised white matter hyperintensities segmentation on MRI. o
- 384 Effects of a targeted resistance intervention compared to a sham intervention on gluteal muscle hypertrophy, fatty infiltration and strength in people with hip osteoarthritis: analysis of secondary outcomes from a randomised clinical trial. **2022**, 23, o
- 383 Learning the Hidden Signature of Fetal Arch Anatomy: a Three-Dimensional Shape Analysis in Suspected Coarctation of the Aorta. 1
- 382 Brainnetome atlas of preadolescent children based on anatomical connectivity profiles. o
- 381 DBSegment: Fast and robust segmentation of deep brain structures considering domain generalization. o
- 380 Heliox simulations for initial management of congenital laryngotracheal stenosis. o
- 379 Correlation analysis between unenhanced and enhanced CT radiomic features of lung cancers presenting as solid nodules and their efficacy for predicting hilar and mediastinal lymph node metastases. 2, o
- 378 A multi-reader comparison of normal-appearing white matter normalization techniques for perfusion and diffusion MRI in brain tumors. o
- 377 MAVRIC based T2 mapping assessment of infrapatellar fat pad scarring in patients with total knee arthroplasty. o
- 376 Anterior connectivity critical for recovery of connected speech after stroke. o
- 375 ¹²⁹Xe and Free-Breathing ¹H Ventilation MRI in Patients With Cystic Fibrosis: A Dual-Center Study. o
- 374 In Vivo 7-Tesla MRI Investigation of Brain Iron and Its Metabolic Correlates in Chronic Schizophrenia. **2022**, 8, o
- 373 Intersession Repeatability of Diffusion-Tensor Imaging in the Supraspinatus and the Infraspinatus Muscles of Volunteers. o
- 372 Individual electric field predicts functional connectivity changes after anodal transcranial direct-current stimulation in chronic stroke. **2022**, o
- 371 Evaluation of the Relationship Between Sphenoid Sinus Morphology and Area and Volume by Computed Tomography. o
- 370 Magnetization Transfer weighted laminar fMRI with multi-echo FLASH. **2022**, 119725 1
- 369 Magnetic resonance imaging reveals possible cause of diplopia after Baerveldt glaucoma implantation. **2022**, 17, e0276527 o
- 368 Prognostic value of multi b-value DWI in patients with locally advanced rectal cancer. o

- 367 3D Centroidnet: Nuclei Centroid Detection with Vector Flow Voting. **2022**, 103252 o
- 366 Developing an automated skeletal phenotyping pipeline to leverage biobank-level medical imaging databases. o
- 365 Lung diffusing capacities for nitric oxide and carbon monoxide at rest and post-walking in long COVID. 00363-2022 o
- 364 Age-Related Changes in the Spatial Variation of Magnetic Susceptibility of Human Articular Cartilage. o
- 363 BMAT: an open-source BIDS Managing and Analysis Tool. **2022**, 103252 o
- 362 Fusion of quantitative susceptibility maps and T1-weighted images improve brain tissue contrast in primates. **2022**, 264, 119730 o
- 361 Feasibility of deconvolution-based multiphase CT angiography perfusion maps in acute ischemic stroke: Simulation and concordance with CT perfusion. **2022**, 31, 106844 o
- 360 Liver lesion changes analysis in longitudinal CECT scans by simultaneous deep learning voxel classification with SimU-Net. **2023**, 83, 102675 o
- 359 Exploring (peri-) lesional and structural connectivity tissue damage through T1/T2-weighted ratio in iron rim multiple sclerosis lesions. **2023**, 95, 12-18 o
- 358 A Framework for Simulating Cardiac MR Images with Varying Anatomy and Contrast. **2022**, 1-1 o
- 357 Progressive Perception Learning for Main Coronary Segmentation in X-ray Angiography. **2022**, 1-1 o
- 356 Low-cost 3D-printed anthropomorphic cardiac phantom, for computed tomography automatic left ventricle segmentation and volumetry IA pilot study. **2023**, 29, 131-138 o
- 355 Gradient-based edge detection with skeletonization (GES) segmentation for magnetic resonance optic nerve images. **2023**, 80, 104342 o
- 354 Digital twin as a tool for evaluating and optimizing flow behavior in encapsulating processes. **2022**, 1-1 o
- 353 An MR-based brain template and atlas for optical projection tomography and light sheet fluorescence microscopy. o
- 352 Assessment of Internal Nasal Dimensions of Individuals With Cleft Lip and Palate and Obstructive Sleep Apnea Syndrome by Computed Tomography. 105566562211336 o
- 351 A pairwise radiomics algorithm - lesion pair relation estimation (PRE) model for distinguishing multiple primary lung cancer (MPLC) from intrapulmonary metastasis (IPM). o
- 350 Evaluation of a radiomics nomogram derived from Fluoride-18 PSMA-1007 PET/CT for risk stratification in newly diagnosed prostate cancer. 12, o

- 349 Applying MAP-MRI to Identify the WHO Grade and Main Genetic Features of Adult-type Diffuse Gliomas: A Comparison of Three Diffusion-weighted MRI Models. **2022**, 0
- 348 Risk prediction of pancreatic cancer using AI analysis of pancreatic subregions in computed tomography images. 12, 1
- 347 Assessing pupil size as an index of activation of subcortical ascending arousal system nuclei during rest. 0
- 346 Strain estimation in aortic roots from 4D echocardiographic images using medial modeling and deformable registration. 0
- 345 Reproducibility and repeatability of a semi-automated pipeline to quantify trapeziometacarpal joint angles using dynamic computed tomography. **2022**, 22, 0
- 344 Anterior pelvic plane estimation for total hip arthroplasty using a joint ultrasound and statistical shape model based approach. 0
- 343 New insights into anatomical connectivity along the anterior-posterior axis of the human hippocampus using in vivo quantitative fibre tracking. 11, 1
- 342 Impaired in vivo fetoplacental development is associated with neonatal neurobehavioral outcomes. 0
- 341 Assessment of Thigh MRI Radiomics and Clinical Characteristics for Assisting in Discrimination of Juvenile Dermatomyositis. **2022**, 11, 6712 0
- 340 An Optimized Methodology for Patient-Specific Therapeutic Activity Administration in Liver Radioembolization. **2022**, 12, 11669 0
- 339 Tubers affecting the fusiform face area are associated with autism diagnosis. 0
- 338 Predicting the tissue outcome of acute ischemic stroke from acute 4D computed tomography perfusion imaging using temporal features and deep learning. 16, 0
- 337 A Web-Based Automated Image Processing Research Platform for Cochlear Implantation-Related Studies. **2022**, 11, 6640 0
- 336 Segmentation of human aorta using 3D nnU-net-oriented deep learning. **2022**, 93, 114103 0
- 335 Improved generalized ComBat methods for harmonization of radiomic features. **2022**, 12, 0
- 334 High-resolution cortical parcellation based on conserved brain landmarks for localization of multimodal data to the nearest centimeter. **2022**, 12, 0
- 333 Medial temporal lobe structure, mnemonic and perceptual discrimination in healthy older adults and those at risk for mild cognitive impairment. **2022**, 1
- 332 Mesoscopic in vivo human T2* dataset acquired using quantitative MRI at 7 Tesla. **2022**, 264, 119733 0

331	Longitudinal and prospective assessment of prenatal maternal sleep quality and associations with newborn hippocampal and amygdala volume. 2022 , 58, 101174	0
330	The Liver Tumor Segmentation Benchmark (LiTS). 2022 , 102680	9
329	Automated segmentation of craniopharyngioma on MR images using U-Net-based deep convolutional neural network.	1
328	HRU-Net: A Transfer Learning Method for Carotid Artery Plaque Segmentation in Ultrasound Images. 2022 , 12, 2852	0
327	Skeletal Muscle Segmentation at the Third Lumbar Vertebral Level in Radiotherapy CT Images. 2023 , 77-88	0
326	A compact breast shape acquisition system for improving diffuse optical tomography image reconstructions.	0
325	Cardiac Digital Twin Modeling. 2022 , 111-134	0
324	Morphometric analysis of Corpus Callosum in autistic and typically developing Indian children. 2023 , 328, 111580	0
323	A comprehensive machine-learning model applied to MRI to classify germinomas of the pineal region. 2023 , 152, 106366	0
322	Detecting liver cirrhosis in computed tomography scans using clinically-inspired and radiomic features. 2023 , 152, 106378	2
321	Automated liver tissues delineation techniques: A systematic survey on machine learning current trends and future orientations. 2023 , 117, 105532	1
320	Aberrant claustrum structure in preterm-born neonates: an MRI study. 2023 , 37, 103286	0
319	Anatomical attention-based prediction of postoperative pulmonary venous obstruction via CTA images. 2023 , 103, 102163	0
318	Automated CT pancreas segmentation for acute pancreatitis patients by combining a novel object detection approach and U-Net. 2023 , 81, 104430	0
317	Combined Radiomics Clinical Model to Predict Radiotherapy Response in Inoperable Stage III and IV Non-Small-Cell Lung Cancer. 2022 , 21, 153303382211424	0
316	Coevolution of language and tools in the human brain: An ALE meta-analysis of neural activation during syntactic processing and tool use. 2022 ,	0
315	Development of Implicit Representation Method for Freehand 3D Ultrasound Image Reconstruction of Carotid Vessel. 2022 ,	0
314	Radiomics for Discriminating Benign and Malignant Salivary Gland Tumors; Which Radiomic Feature Categories and MRI Sequences Should Be Used?. 2022 , 14, 5804	1

- 313 Impact of BloodBrain Barrier to Delivering a Vascular-Disrupting Agent: Predictive Role of Multiparametric MRI in Rodent Craniofacial Metastasis Models. **2022**, 14, 5826 ○
- 312 Preoperative SPECT/CT + intraoperative CT fusion enabling surgical augmented reality to target sentinel lymph node in endometrial cancer. **2022**, 9, ○
- 311 Image downsampling expedited adaptive least-squares (IDEAL) fitting improves intravoxel incoherent motion (IVIM) analysis in the human kidney. **2023**, 89, 1055-1067 ○
- 310 Decoding molecular programs in melanoma brain metastases. **2022**, 13, ○
- 309 Human Brainstem and Cerebellum Atlas- Chemoarchitecture and Cytoarchitecture Paired to MRI. JN-RM-0587-22
- 308 Evaluating Upstaging in Ductal Carcinoma In Situ Using Preoperative MRI-Based Radiomics. ○
- 307 Optimal radiological gallbladder lesion characterization by combining visual assessment with CT-based radiomics. 1
- 306 Deep learning model based on contrast-enhanced ultrasound for predicting early recurrence after thermal ablation of colorectal cancer liver metastasis. ○
- 305 Accuracy, repeatability, and reproducibility of T1 and T2 relaxation times measurement by 3D magnetic resonance fingerprinting with different dictionary resolutions. ○
- 304 Predicting muscle invasion in bladder cancer by deep learning analysis of MRI: comparison with vesical imagingReporting and data system. 1
- 303 Igneous: Distributed dense 3D segmentation meshing, neuron skeletonization, and hierarchical downsampling. 16, ○
- 302 The spatial relationship between the MRI lesion and intraoperative electrocorticography in focal epilepsy surgery. **2022**, 4, ○
- 301 Impact of bruxism on craniomandibular morphology: A cone-beam computed tomographic study. 1-11 ○
- 300 Fully automated condyle segmentation using 3D convolutional neural networks. **2022**, 12, ○
- 299 Latent class analysis of imaging and clinical respiratory parameters from patients with COVID-19-related ARDS identifies recruitment subphenotypes. **2022**, 26, ○
- 298 Quantitative susceptibility mapping using plug-and-play alternating direction method of multipliers. **2022**, 12, ○
- 297 The retrocolic fascial system revisited for right hemicolectomy with complete mesocolic excision based on anatomical terminology: do we need the eponyms Toldt, Gerota, Fredet and Treitz?. ○
- 296 Spatial and Spectral Components of the BOLD Global Signal in Rat Resting-State Functional MRI. ○

- 295 Visualization of human optic nerve by diffusion tensor mapping and degree of neuropathy. **2022**, 17, e0278987 o
- 294 Neuroplasticity of the Lateral Geniculate Nucleus in Response to Retinal Gene Therapy in a Group of Patients with RPE65 Mutations. Volume 14, 137-147 o
- 293 Survival Rate Prediction of Nasopharyngeal Carcinoma Patients based on MRI and Gene Expression using Deep Neural Network. o
- 292 Artificial neural network applied to fragile X-associated tremor/ataxia syndrome stage diagnosis based on peripheral mitochondrial bioenergetics and brain imaging outcomes. **2022**, 12, o
- 291 A Modified Fuzzy Inference Rule-Based Model for 3D Speckle Tracking. o
- 290 Reciprocal Assistance of Intravascular Imaging in Three-dimensional Stent Reconstruction: Using Cross-Modal Translation Based on Disentanglement Representation. **2022**, 102166 o
- 289 The brain structure and the neural network features of the diurnal cuttlefish *Sepia plangon*. **2022**, 105846 o
- 288 3D Ultrasound versus Computed Tomography for Tumor Volume Measurement Compared to Gross Pathology: A Pilot Study on an Animal Model. **2022**, 8, 329 o
- 287 Genetic Variants of Phospholipase C- α Confer Altered Microglial Phenotypes and Differential Risk for Alzheimer's Disease. o
- 286 Neuroimaging markers of dual impairment in cognition and physical performance following stroke: The Nor-COAST study. 14, o
- 285 Systematic evaluation of anatomical details on transcranial electric stimulation and transcranial magnetic stimulation induced electric fields in a non-human primate model. o
- 284 Assessing breast density using the chemical-shift encoding-based proton density fat fraction in 3-T MRI. o
- 283 Isotopic Radiolabeling of Crizotinib with Fluorine-18 for In Vivo Pet Imaging. **2022**, 15, 1568 o
- 282 An Integrated Clinical-MR Radiomics Model to Estimate Survival Time in Patients With Endometrial Cancer. 2
- 281 A Genetically Encoded Magnetic Resonance Imaging Reporter Enables Sensitive Detection and Tracking of Spontaneous Metastases in Deep Tissues. o
- 280 Mammillary body and hypothalamic volumes in mood disorders. **2022**, o
- 279 Associations of phosphorylated tau pathology with whole-hemisphere ex vivo morphometry in 7 tesla MRI. o
- 278 Task Demands Differentiate Regional Depth-Dependent Activity Profiles Within the Ventral Visual Pathway. o

277	3D-MASNet : 3D mixed-scale asymmetric convolutional segmentation network for 6-month-old infant brain MR images.	0
276	DLL1 haploinsufficiency causes brain abnormalities with functional relevance. 16,	0
275	Convolutional neural network for automated segmentation of the liver and its vessels on non-contrast T1 vibe Dixon acquisitions. 2022 , 12,	0
274	Comparison of epicardial adipose tissue volume quantification between ECG-gated cardiac and non-ECG-gated chest computed tomography scans. 2022 , 22,	0
273	Gut microbial dysbiosis correlates with stroke severity markers in aged rats. 1,	0
272	Artificial Intelligence (AI) for Detection and Localization of Unobturated Second Mesial Buccal (MB2) Canals in Cone-Beam Computed Tomography (CBCT). 2022 , 12, 3214	1
271	Rare but persistent asexual reproduction explains the success of planktonic foraminifera in polar oceans.	1
270	A radiomic model to classify response to neoadjuvant chemotherapy in breast cancer. 2022 , 22,	1
269	Comparative Assessment of Biomechanical Parameters in Subjects With Multiple Cerebral Aneurysms Using Fluid-Structure Interaction Simulations. 2023 , 145,	0
268	Effect of two eccentric hamstring exercises on muscle architectural characteristics assessed with diffusion tensor MRI.	0
267	Acidovorax temperans polarizes T17 cells and skews neutrophil maturation to promote lung adenocarcinoma development.	0
266	Radiomics based on preoperative rectal cancer MRI to predict the metachronous liver metastasis.	0
265	Effect of deep gray matter atrophy on information processing speed in early relapsing- remitting multiple sclerosis.	0
264	Value of T2-weighted-based radiomics model in distinguishing Warthin tumor from pleomorphic adenoma of the parotid.	0
263	Deep Learning Radiomics Nomogram Based on Multiphase Computed Tomography for Predicting Axillary Lymph Node Metastasis in Breast Cancer.	0
262	Phantom-based evaluation of yttrium-90 datasets using biograph vision quadra.	0
261	Tractography-based navigated TMS language mapping protocol. 12,	0
260	A critical guide to the automated quantification of perivascular spaces in magnetic resonance imaging. 16,	0

259	The association between paraspinal muscle parameters and vertebral pedicle microstructure in patients undergoing lumbar fusion surgery.	0
258	Evaluation of lesion and overlying articular cartilage in patients with juvenile osteochondritis dissecans of the knee using quantitative diffusion MRI.	0
257	Topological data analysis of thoracic radiographic images shows improved radiomics-based lung tumor histology prediction. 2022 , 100657	0
256	Computed Tomographic Radiomics in Differentiating Histologic Subtypes of Epithelial Ovarian Carcinoma. 2022 , 5, e2245141	0
255	Federated learning enables big data for rare cancer boundary detection. 2022 , 13,	1
254	3D vs. 2D MRI radiomics in skeletal Ewing sarcoma: Feature reproducibility and preliminary machine learning analysis on neoadjuvant chemotherapy response prediction. 12,	0
253	Diagnostic Accuracy and Reliability of Noncontrast Computed Tomography Markers for Acute Hematoma Expansion among Radiologists. 2022 , 8, 2893-2901	0
252	A machine learning approach for predicting perihematoma edema expansion in patients with intracerebral hemorrhage.	0
251	Airway Detection in COPD at Low-Dose CT Using Deep Learning and Multiparametric Freeze and Grow. 2022 , 4,	0
250	Postmortem quantitative MRI disentangles histological lesion types in multiple sclerosis.	0
249	Prognostic Value of Combined Radiomic Features from Follow-Up DWI and T2-FLAIR in Acute Ischemic Stroke. 2022 , 9, 468	0
248	Predicting Hypoperfusion Lesion and Target Mismatch in Stroke from Diffusion-weighted MRI Using Deep Learning.	1
247	Voxel-S-value methods adapted to heterogeneous media for quantitative Y-90 microsphere radioembolization dosimetry. 2022 ,	0
246	Voice efficiency for different voice qualities combining experimentally derived sound signals and numerical modeling of the vocal tract. 13,	0
245	The impact of etiology in lesion-symptom mapping [A direct comparison between tumor and stroke. 2022 , 103305	0
244	ISLES 2022: A multi-center magnetic resonance imaging stroke lesion segmentation dataset. 2022 , 9,	0
243	The sinuous, wave-like intratumoral-wall sign is a sensitive and specific radiological biomarker for oligodendrogliomas.	0
242	Quantifying intrafractional gastric motion using auto-segmentation on MRI: Deformation and respiratory-induced displacement compared.	0

- 241 Multimodal Assessment of Bottlenose Dolphin Auditory Nuclei Using 7-Tesla MRI, Immunohistochemistry and Stereology. **2022**, 9, 692 1
- 240 A computational method for estimating trunk muscle activations during gait using lower extremity muscle synergies. 10, 0
- 239 Longitudinal hippocampal diffusion-weighted imaging and T2 relaxometry demonstrate regional abnormalities which are stable and predict subfield pathology in temporal lobe epilepsy. 0
- 238 Quantitative magnetic resonance imaging assessment of muscle composition in myotonic dystrophy mice. **2023**, 13, 0
- 237 Novel EGFR-mutant mouse models of lung adenocarcinoma reveal adaptive immunity requirement for durable osimertinib response. **2023**, 216062 0
- 236 Distinguishing common renal cell carcinomas from benign renal tumors based on machine learning: comparing various CT imaging phases, slices, tumor sizes, and ROI segmentation strategies. 0
- 235 Preoperative visualization of congenital lung abnormalities: hybridizing artificial intelligence and virtual reality. 0
- 234 Acquisition of novel muscles enabled protruding and retracting mechanisms of female penis in sex-role reversed cave insects. **2023**, 10, 0
- 233 Cartesian three-dimensional method to quantify displacements between cone beam computed tomography models. **2022**, 27, 0
- 232 Multilesion Segmentations in Patients with Intracerebral Hemorrhage: Reliability of ICH, IVH and PHE Masks. **2023**, 9, 89-97 0
- 231 Lesion location across diagnostic regions in multiple sclerosis. **2023**, 37, 103311 0
- 230 AI-based MRI auto-segmentation of brain tumor in rodents, a multicenter study. **2023**, 11, 0
- 229 Automatic segmentation of human knee anatomy by a convolutional neural network applying a 3D MRI protocol. **2023**, 24, 0
- 228 Autonomous robotic system for breast biopsy with deformation compensation. **2023**, 1-8 0
- 227 Patient-specific Finite Element simulation of peripheral artery Percutaneous Transluminal Angioplasty to evaluate the procedure outcome without stent implantation. 0
- 226 Histological E-data registration in rodent brain spaces. 12, 0
- 225 Preoperative functional connectivity by magnetic resonance imaging for refractory neocortical epilepsy. 0
- 224 Combining in vivo proton exchange rate (kex) MRI with quantitative susceptibility mapping to further stratify the gadolinium-negative multiple sclerosis lesions. 16, 0

223	Association between hypertension and neurovascular inflammation in both normal-appearing white matter and white matter hyperintensities. 2023 , 11,	1
222	Quantitative and Qualitative Analysis of 18 Deep Convolutional Neural Network (CNN) Models with Transfer Learning to Diagnose COVID-19 on Chest X-Ray (CXR) Images. 2023 , 4,	0
221	Using Deep Learning to Predict Treatment Response in Patients with Hepatocellular Carcinoma Treated with Y90 Radiation Segmentectomy.	0
220	Age-Related Changes in Risky Decision Making and Associated Neural Circuitry in a Rat Model. 2023 , 10, ENEURO.0385-22.2022	0
219	4D segmentation of the thoracic aorta from 4D flow MRI using deep learning. 2023 ,	0
218	A preconception lifestyle intervention in women with obesity and cardiovascular health in their children.	0
217	A postmortem MRI study of cerebrovascular disease and iron content at end-stage of fragile X-associated tremor/ataxia syndrome.	0
216	Machine learning in 3D auto-filling alveolar cleft of CT images to assess the influence of alveolar bone grafting on the development of maxilla. 2023 , 23,	0
215	Impact of sedation, body position change and continuous positive airway pressure on distribution of ventilation in healthy foals. 9,	0
214	Diversity Learning Based on Multi-Latent Space for Medical Image Visual Question Generation. 2023 , 23, 1057	0
213	MRI -based measurement of in vivo disc mechanics in a young population due to flexion, extension, and diurnal loading.	0
212	Multimodality annotated hepatocellular carcinoma data set including pre- and post-TACE with imaging segmentation. 2023 , 10,	0
211	Lesion-symptom mapping of language impairments in people with brain tumours: The influence of linguistic stimuli.	0
210	Development and validation of an interpretable radiomic nomogram for severe radiation proctitis prediction in postoperative cervical cancer patients. 13,	0
209	A standardized protocol for manually segmenting stroke lesions on high-resolution T1-weighted MR images. 1,	0
208	AI-BRAF V600E : A deep convolutional neural network for BRAF V600E mutation status prediction of thyroid nodules using ultrasound images. 20220057	0
207	Fetal MRI radiomics: non-invasive and reproducible quantification of human lung maturity.	0
206	3D carotid artery segmentation using shape-constrained active contours. 2023 , 153, 106530	0

- 205 Lumbar intervertebral disc segmentation for computer modeling and simulation. **2023**, 230, 107337 ○
- 204 Multimodal fusion model for classifying placenta ultrasound imaging in pregnancies with hypertension disorders. **2023**, 31, 46-53 ○
- 203 Automatic delineation of hippocampus in CT images based on deep learning and dosimetry study in whole brain radiotherapy. **2023**, 16, 100517 ○
- 202 Three-Dimensional Quantitative Assessment of Condylar Displacement and Adaptive Remodeling in Asymmetrical Mandibular Prognathism Patients After Sagittal Split Ramus Osteotomy. **2023**, 34, 240-246 ○
- 201 Pipeline for Automated Processing of Clinical Cone-Beam Computed Tomography for Patient-Specific Temporal Bone Simulation: Validation and Clinical Feasibility. **2023**, 44, e88-e94 ○
- 200 A predictive model for early therapeutic efficacy of colorectal liver metastases using multimodal MRI data. **2022**, 1-16 ○
- 199 Specific features of designing a database for neuro-oncological 3D MRI images to be used in training artificial intelligence. **2022**, 42, 51-59 ○
- 198 Assessment of different regions of interest-based methods for [99mTc]Tc DAT-SPECT quantification using an anthropomorphic striatal phantom. **2022**, 9, ○
- 197 A Novel Two-Stage Framework for 2D/3D Registration in Neurological Interventions. **2022**, ○
- 196 3D-3D Superimposition of Pubic Bones: Expanding the Anthropological Toolkit for the Pair-Matching of Commingled Skeletal Remains. **2023**, 12, 30 ○
- 195 Robustness of Radiomics in Pre-Surgical Computer Tomography of Non-Small-Cell Lung Cancer. **2023**, 13, 83 ○
- 194 Plant Root Phenotyping Using Deep Conditional GANs and Binary Semantic Segmentation. **2023**, 23, 309 ○
- 193 PhiPipe : A multi-modal MRI data processing pipeline with test-retest reliability and predicative validity assessments. ○
- 192 Framework to Detect Schizophrenia in Brain MRI Slices with Mayfly Algorithm-Selected Deep and Handcrafted Features. **2023**, 23, 280 ○
- 191 3D-CNN Method over Shifted Patch Tokenization for MRI-Based Diagnosis of Alzheimer's Disease Using Segmented Hippocampus. **2022**, 9, 245-252 ○
- 190 Co-administration of prism adaptation and methylphenidate needs striatal integrity to alleviate spatial neglect. ○
- 189 HoloLens in breast reconstruction: what is the future? Publish Ahead of Print, ○
- 188 Radiomic features derived from pretherapeutic MRI predict chemoradiation response in locally advanced rectal cancer. Publish Ahead of Print, ○

- 187 Development and Validation of a Deep Learning Algorithm to Differentiate Colon Carcinoma From Acute Diverticulitis in Computed Tomography Images. **2023**, 6, e2253370 ○
- 186 Prenatal depressive symptoms and childhood development of brain limbic and default mode network structure. ○
- 185 Entorhinal grid-like codes and time-locked network dynamics track others navigating through space. **2023**, 14, ○
- 184 Weakly supervised perivascular spaces segmentation with salient guidance of Frangi filter. ○
- 183 Regional age-related changes of neuromelanin and iron in the substantia nigra based on neuromelanin accumulation and iron deposition. ○
- 182 Presurgical Executive Functioning in Low-Grade Glioma Patients Cannot Be Topographically Mapped. **2023**, 15, 807 ○
- 181 Evaluation of the HD-GLIO Deep Learning Algorithm for Brain Tumour Segmentation on Postoperative MRI. **2023**, 13, 363 ○
- 180 Automatic detection of lung nodule in CT scan slices using CNN segmentation schemes: A study. **2023**, 218, 2786-2794 ○
- 179 C. elegans molting requires rhythmic accumulation of the Grainyhead/ LSF transcription factor GRH -1. ○
- 178 Automated prostate multi-regional segmentation in magnetic resonance using fully convolutional neural networks. ○
- 177 Age- and sex-related differences in baboon (Papio anubis) gray matter covariation. **2023**, ○
- 176 Predicting vasospasm risk using first presentation aneurysmal subarachnoid haemorrhage volume: a semi-automated CT image segmentation analysis in ITK-SNAP. ○
- 175 Analysis of the alveolar shape in 3D. ○
- 174 A radiomic biomarker for prognosis of resected colorectal cancer liver metastases generalizes across MRI contrast agents. 13, ○
- 173 Deep learning for improving ZTE MRI images in free breathing. **2023**, 98, 97-104 ○
- 172 Automatic Individual Tooth Segmentation in Cone-Beam Computed Tomography Based on Multi-Task CNN and Watershed Transform. **2022**, ○
- 171 Temporal dynamics of cerebral blood flow during the first year after moderate-severe traumatic brain injury: A longitudinal perfusion MRI study. **2023**, 37, 103344 ○
- 170 Curing profile and marginal gap formation using a liner containing long-wavelength-absorbing photoinitiator: an in vitro study. **2023**, 38, ○

- 169 Marmoset Brain Mapping V5: an Anatomical and Connectivity Atlas of the Cerebellum. o
- 168 Acute repair of meniscus root tear partially restores joint displacements as measured with MRI and loading in a porcine knee. o
- 167 Stattic alleviates pulmonary fibrosis in a mouse model of rheumatoid arthritis. Relevant interstitial lung disease. 153537022311579 o
- 166 Bite force transmission and mandible shape in grasshoppers, crickets, and allies is largely dependent on phylogeny, not diet. o
- 165 A model of fluid structure and biochemical interactions for applications to subclinical leaflet thrombosis. o
- 164 Impaired Maternal-Fetal Environment and Risk for Preoperative Focal White Matter Injury in Neonates With Complex Congenital Heart Disease. **2023**, 12, o
- 163 A potentially fatal cranial pathology in a specimen of *Tarchia*. o
- 162 Thigh muscles are more susceptible to age-related muscle loss when compared to lower leg and pelvic muscles. **2023**, 175, 112159 o
- 161 Improved sensitivity and microvascular weighting of 3T laminar fMRI with GE-BOLD using NORDIC and phase regression. **2023**, 271, 120011 o
- 160 Benchmark dataset for clot detection in ischemic stroke vessel-based imaging: CODEC-IV. **2023**, 271, 119985 o
- 159 LIVE-Net: Comprehensive 3D vessel extraction framework in CT angiography. **2023**, 159, 106886 o
- 158 BigBrain-MR: a new digital phantom with anatomically-realistic magnetic resonance properties at 100- μ m resolution for magnetic resonance methods development. **2023**, 273, 120074 o
- 157 Microcatheter tracking in thrombectomy procedures: A finite-element simulation study. **2023**, 234, 107515 o
- 156 Myocardial Regional Shortening from 4D Cardiac CT Angiography for the Detection of Left Ventricular Segmental Wall Motion Abnormality. **2023**, 5, o
- 155 Estimating age at death by Hausdorff distance analyses of the fourth lumbar vertebral bodies using 3D postmortem CT images. o
- 154 A Pseudo-labeling Approach to Semi-supervised Organ Segmentation. **2022**, 318-326 o
- 153 Paradoxical consequences of early hippocampal damage: greater atrophy is associated with better recall, working memory and visuospatial perception in developmental amnesia. o
- 152 Enhancing students' understanding of cardiac physiology by using 4D visualization. **2023**, 36, 542-549 o

- 151 Toward a realistic in silico abdominal phantom for QSM. **2023**, 89, 2402-2418 ○
- 150 A Multicenter Longitudinal MRI Study Assessing LeMan-PV Software Accuracy in the Detection of White Matter Lesions in Multiple Sclerosis Patients. ○
- 149 MRI Response Assessment in Patients with Glioblastoma Treated with Dendritic Cell-Based Immunotherapy. 31-32 ○
- 148 Aberrant functional connectivity of the bed nucleus of the stria terminalis and its age dependence in children and adolescents with social anxiety disorder. **2023**, 82, 103498 ○
- 147 Effects of inhaled cannabis high in Δ -THC or CBD on the aging brain: A translational MRI and behavioral study. 15, ○
- 146 Electric field simulations of transcranial direct current stimulation in children with perinatal stroke. 17, ○
- 145 Fully automated imaging protocol independent system for pituitary adenoma segmentation: A Convolutional Neural Network-based model on sparsely annotated MRI. ○
- 144 Longitudinal Assessment of Multiple Sclerosis Lesion Load With Synthetic Magnetic Resonance Imaging: A Multicenter Validation Study. **2023**, 58, 320-326 ○
- 143 Evaluation of statistical detection of change algorithm for triaging multiple sclerosis patients with new lesion activity on longitudinal brain MRI. ○
- 142 A deep learning model with data integration of ultrasound contrast-enhanced micro-flow cines, B-mode images, and clinical parameters for diagnosing significant liver fibrosis in patients with chronic hepatitis B. ○
- 141 Manganese Enhanced Magnetic Resonance Imaging reveals light-induced brain asymmetry in embryo. ○
- 140 Durable responses to alectinib in murine models of EML4-ALK lung cancer requires adaptive immunity. **2023**, 7, ○
- 139 Path integration selectively predicts midlife risk of Alzheimer's disease. ○
- 138 Prediction of 3-year recurrence rate of hepatocellular carcinoma after resection based on contrast-enhanced CT: a single-centre study. ○
- 137 Evaluating Histological Subtypes Classification of Primary Lung Cancers on Unenhanced Computed Tomography Based on Random Forest Model. **2023**, 2023, 1-8 ○
- 136 Validation of a New Coil Array Tailored for Dog Functional Magnetic Resonance Imaging Studies. **2023**, 10, ENEURO.0083-22.2022 ○
- 135 Time series radiomics for the prediction of prostate cancer progression in patients on active surveillance. ○
- 134 Reproducibility of 2D versus 3D radiomics for quantitative assessment of fetal lung development: a retrospective fetal MRI study. **2023**, 14, ○

- 133 Evaluation of KRASG12C inhibitor responses in novel murine KRASG12C lung cancer cell line models. 13, ○
- 132 Predicting prognosis of nasopharyngeal carcinoma based on deep learning: peritumoral region should be valued. **2023**, 23, ○
- 131 Loss of aquaporin-4 results in glymphatic system dysfunction via brain-wide interstitial fluid stagnation. 12, 1
- 130 Radiomics analysis in medical imaging research. **2023**, 70, 3-7 ○
- 129 Deep learning applications in osteoarthritis imaging. ○
- 128 Impact of Peripheral Auditory Structure on the Development of Auditory-Language Network in Children with Profound Sensorineural Hearing Loss. ○
- 127 Effect of deep gray matter atrophy on information processing speed in early relapsing-remitting multiple sclerosis. **2023**, 71, 104560 ○
- 126 Assessment of transmitral and left atrial appendage flow rate from cardiac 4D-CT. **2023**, 3, ○
- 125 A deep learning-based fully automatic and clinical-ready framework for regional myocardial segmentation and myocardial ischemia evaluation. ○
- 124 A Deep Learning Approach for Automated Bone Removal from Computed Tomography Angiography of the Brain. ○
- 123 Developmental biomechanics and age polyethism in leaf-cutter ants. ○
- 122 Swin Unet3D: a three-dimensional medical image segmentation network combining vision transformer and convolution. **2023**, 23, ○
- 121 Preoperative meningioma vascularity index is associated with significantly increased intraoperative blood loss and greater risk of subtotal resection. **2023**, 161, 583-591 ○
- 120 A biomechanical model for the relation between bite force and mandibular opening angle in arthropods. **2023**, 10, ○
- 119 At mid- to long-term follow-up after proximal hamstring tendon avulsion; there was greater fatty infiltration, muscle atrophy and strength deficit in the hamstring muscles of the injured leg than in the uninjured leg. **2023**, 18, ○
- 118 Automated Volumetric Quantification of Cardiac Chambers and Cross Sectional Measurement of Great Arteries in Cardiac CT. **2022**, ○
- 117 Opportunistic Evaluation of Trabecular Bone Texture by MRI Reflects Bone Mineral Density and Microarchitecture. ○
- 116 Outcome Prediction of Spontaneous Supratentorial Intracerebral Hemorrhage after Surgical Treatment Based on Non-Contrast Computed Tomography: A Multicenter Study. **2023**, 12, 1580 ○

- 115 Differentiating Multiple Myeloma and Osteolytic Bone Metastases on Contrast-Enhanced Computed Tomography Scans: The Feasibility of Radiomics Analysis. **2023**, 13, 755 o
- 114 A novel method to estimate adult age from the lumbar vertebral body using 3D PMCT images in Japanese. **2023**, 61, 102215 o
- 113 Fetal MRI based brain atlas analysis detects initial in utero effects of prenatal alcohol exposure. o
- 112 Machine Learning in Lung Cancer Radiomics. o
- 111 Preoperative prediction of tumor deposits in rectal cancer with clinical-magnetic resonance deep learning-based radiomic models. 13, o
- 110 The Effect of Blood Rheology and Inlet Boundary Conditions on Realistic Abdominal Aortic Aneurysms under Pulsatile Flow Conditions. **2023**, 10, 272 o
- 109 Neurological scoring and gait kinematics to assess functional outcome in an ovine model of ischaemic stroke. 14, o
- 108 Ultra-high-field pharmacological functional MRI of dopamine D1 receptor-related interventions in anesthetized rats. **2023**, 11, o
- 107 UNRAVELing the synergistic effects of psilocybin and environment on brain-wide immediate early gene expression in mice. o
- 106 Multimodal 3D Mouse Brain Atlas Framework with the Skull-Derived Coordinate System. **2023**, 21, 269-286 o
- 105 Automatic landmark identification in cone-beam computed tomography. 2
- 104 Paths to hippocampal damage in neuromyelitis optica spectrum disorders. **2023**, 49, o
- 103 Sex-specific effects of high-fat diet on rat brain glucose metabolism and early-onset dementia symptoms. **2023**, 211, 111795 o
- 102 Evaluation of eight registration algorithms applied to the insula and insular gyri. o
- 101 Brain growth in fetuses with congenital diaphragmatic hernia. o
- 100 Structural connectivity in recovery after coma: Connectome atlas approach. **2023**, 37, 103358 o
- 99 Deep-Learning Models for Detection and Localization of Visible Clinically Significant Prostate Cancer on Multi-Parametric MRI. o
- 98 Artificial intelligence-based computer-aided diagnosis system supports diagnosis of lymph node metastasis in esophageal squamous cell carcinoma: A multicenter study. **2023**, 9, e14030 o







- 97 Artificial Intelligence as a Diagnostic Tool in Non-Invasive Imaging in the Assessment of Coronary Artery Disease. **2023**, 11, 20 ○
- 96 Automatic placental and fetal volume estimation by a convolutional neural network. **2023**, 134, 23-29 ○
- 95 Effect of motion, cortical orientation and spatial resolution on quantitative imaging of cortical R2* and magnetic susceptibility at 0.3 mm in-plane resolution at 7 T. **2023**, 270, 119992 ○
- 94 MRI Liver Imaging Integrated with Texture Analysis in Native Liver Survivor Patients with Biliary Atresia after Kasai Portoenterostomy: Correlation with Medical Outcome after Surgical Treatment. **2023**, 10, 306 ○
- 93 MVI-TR: A Transformer-Based Deep Learning Model with Contrast-Enhanced CT for Preoperative Prediction of Microvascular Invasion in Hepatocellular Carcinoma. **2023**, 15, 1538 ○
- 92 Changes in psoas muscle size and ambulatory function after internal hemipelvectomy without reconstruction. **2023**, 105-B, 323-330 ○
- 91 Development of retinal structure in perinatally HIV-infected children and adolescents: A longitudinal and cross-sectional assessment. **2023**, 18, e0282284 ○
- 90 Functional connectivity alterations in traumatic brain injury patients with late seizures. **2023**, 179, 106053 ○
- 89 Predicting muscle invasion in bladder cancer based on MRI: A comparison of radiomics, and single-task and multi-task deep learning. **2023**, 233, 107466 ○
- 88 Magnetic resonance imaging-based radiomics assesses the level of immune cell infiltration in the breast cancer tumor microenvironment. ○
- 87 Quantitative analysis of pelvic bone marrow fat using an MRI-based machine learning method for distinguishing aplastic anaemia from myelodysplastic syndromes. **2023**, ○
- 86 Workflow Comparison for Combined 4D MRI/CFD Patient-Specific Cardiovascular Flow Simulations of the Thoracic Aorta. **2023**, 145, ○
- 85 SPECT and CT misregistration reduction in [99mTc]Tc-MAA SPECT/CT for precision liver radioembolization treatment planning. ○
- 84 Automatic segmentation of the choroid plexuses: Method and validation in controls and patients with multiple sclerosis. **2023**, 38, 103368 ○
- 83 Integrative Scoring System for Survival Prediction in Patients With Locally Advanced Nasopharyngeal Carcinoma: A Retrospective Multicenter Study. **2023**, ○
- 82 Deep Learning for Head and Neck CT Angiography: Stenosis and Plaque Classification. ○
- 81 Development and validation of a CT-based radiomics signature for identifying high-risk neuroblastomas under the revised Children's Oncology Group classification system. **2023**, 70, ○
- 80 External Validation of DeepBleed: The first open-source 3D Deep Learning Network for the Segmentation of Intracerebral and Intraventricular Hemorrhage. ○

- 79 Compact breast shape acquisition system for improving diffuse optical tomography image reconstructions. **2023**, 14, 1579 ○
- 78 A Comparison between the Results from Linear Analysis and Nonlinear Analysis in the Context of Simulation of Biological Materials. **2023**, 7, 109 ○
- 77 A neuroscientist's guide to using murine brain atlases for efficient analysis and transparent reporting. 17, ○
- 76 Neural network-derived perfusion maps: A model-free approach to computed tomography perfusion in patients with acute ischemic stroke. 17, ○
- 75 Annotated computed tomography coronary angiogram images and associated data of normal and diseased arteries. **2023**, 10, ○
- 74 Human parasagittal dura is a potential neuroimmune interface. **2023**, 6, ○
- 73 Morphological and Metrical Relationships Between Sphenoid Sinus and Sella Turcica: Possible Applications in Transnasal Transsphenoidal Surgery. Publish Ahead of Print, ○
- 72 Long-term high-fat diet increases glymphatic activity in the hypothalamus in mice. **2023**, 13, ○
- 71 An enigmatic pelagic fish with internalized red muscle: A future regional endotherm or forever an ectotherm?. ○
- 70 Pituitary Tumor Classification using Machine Learning. **2022**, ○
- 69 Fast layer-fMRI VASO with short stimuli and event-related designs at 7T. ○
- 68 Imaging angiogenesis in an intracerebrally induced model of brain macrometastasis using $\alpha\text{v}\beta\text{3}$ -targeted iron oxide microparticles. ○
- 67 Nonsymbolic Numerosity Maps at the Occipitotemporal Cortex Respond to Symbolic Numbers. **2023**, 43, 2950-2959 ○
- 66 The association between blood pressure variability and perihematoma edema after spontaneous intracerebral hemorrhage. 14, ○
- 65 Manual lesion segmentations for traumatic brain injury characterization. 2, ○
- 64 Application of Automatic Segmentation on Super-Resolution Reconstruction MR Images of the Abnormal Fetal Brain. **2023**, 44, 486-491 ○
- 63 Effect of Dataset Size and Medical Image Modality on Convolutional Neural Network Model Performance for Automated Segmentation: A CT and MR Renal Tumor Imaging Study. ○
- 62 In vivo assessment of differences in fungal cell density in cerebral cryptococcomas of mice infected with *Cryptococcus neoformans* or *Cryptococcus gattii*. **2023**, 105127 ○

- 61 A radiomics approach to the diagnosis of femoroacetabular impingement. 3, ○
- 60 Evaluation of non-traumatic brachial plexus using Diffusion Tensor Imaging. ○
- 59 Remote effects of temporal lobe epilepsy surgery: long-term morphological changes after surgical resection. ○
- 58 Predicting Regions of Local Recurrence in Glioblastomas Using Voxel-Based Radiomic Features of Multiparametric Postoperative MRI. **2023**, 15, 1894 ○
- 57 Differential Laminar Activation Dissociates Encoding and Retrieval in the Human Medial and Lateral Entorhinal Cortex. **2023**, 43, 2874-2884 ○
- 56 Helical flow in tortuous aortas and its relationship to turbulence: A whole-aorta 4D flow MRI study. 10, ○
- 55 Persistent Changes in Mechanical Nociception in Rats With Traumatic Brain Injury Involving Polytrauma. **2023**, ○
- 54 Three-Dimensional Radiographic Assessment of Different Fixation Methods Stability After L-shaped Osteotomy Reduction Malarplasty: A Comparative Retrospective Study. **2023**, 101454 ○
- 53 Clinical-radiomics models based on plain X-rays for prediction of lung metastasis in patients with osteosarcoma. **2023**, 23, ○
- 52 CT-based identification of pediatric non-Wilms tumors using convolutional neural networks at a single center. ○
- 51 Massive Neonatal Arterial Ischemic Stroke. **2023**, 144, 5-10 ○
- 50 Retrospective cohort study to devise a treatment decision score predicting adverse 24-month radiological activity in early multiple sclerosis. **2023**, 16, 175628642311618 ○
- 49 Pulmonary vein flow split effects in patient-specific simulations of left atrial flow. ○
- 48 Characterizations of three-dimensional root morphology and topological location of mandibular third molars by cone-beam computed tomography. ○
- 47 Novel metrics to characterize temporal lobe of very preterm infants on term-equivalent brain MRI. ○
- 46 Automatic Segmentation of the Left Atrium from Computed Tomography Angiography Images. ○
- 45 Predicting the Efficacy of SBRT for Lung Cancer with 18F-FDG PET/CT Radiogenomics. **2023**, 13, 884 ○
- 44 Development of an objective method to quantify hippocampal dentation. ○

- 43 Automatic detection of adenoid hypertrophy on cone-beam computed tomography based on deep learning. **2023**, 163, 553-560.e3 ○
- 42 Prognostic Value of Thrombus Volume and Interaction With First-Line Endovascular Treatment Device Choice. **2023**, 54, 1056-1065 ○
- 41 Metabolic Insights into Iron Deposition in Relapsing-Remitting Multiple Sclerosis via 7T Magnetic Resonance Spectroscopic Imaging. ○
- 40 Developing an automated skeletal phenotyping pipeline to leverage biobank-level medical imaging databases. ○
- 39 Residual fibroglandular breast tissue after mastectomy is associated with an increased risk of a local recurrence or a new primary breast cancer". **2023**, 23, ○
- 38 MR Imaging Radiomics Analysis Based on Lumbar Soft Tissue to Evaluate Lumbar Fascia Changes in Patients with Low Back Pain. **2023**, ○
- 37 Evaluation of surface-based hippocampal registration using ground-truth subfield definitions. ○
- 36 Strain estimation in aortic roots from 4D echocardiographic images using medial modeling and deformable registration. **2023**, 87, 102804 ○
- 35 Multimodal anatomical mapping of subcortical regions in Marmoset monkeys using high-resolution MRI and matched histology with multiple stains. ○
- 34 MRI-based radiomic score increased mrTRG accuracy in predicting rectal cancer response to neoadjuvant therapy. ○
- 33 Towards a learning-based CT segmentation of acetabular fractures. **2023**, ○
- 32 Peak width of skeletonized mean diffusivity and cognitive performance in cerebral amyloid angiopathy. 17, ○
- 31 Effect of Enlarged Perivascular Spaces in Reliable Distinction of Prospective Targeting During Deep Brain Stimulation in Patients With Advanced Parkinson's Disease: A Study of Deterministic and Probabilistic Tractography. **2023**, Publish Ahead of Print, ○
- 30 Dynamic monitoring of morphological and hemodynamic evolution of small cerebral aneurysms. **2023**, 12, 172-180 ○
- 29 No difference in extra-axial cerebrospinal fluid volumes across neurodevelopmental and psychiatric conditions in later childhood and adolescence. **2023**, 15, ○
- 28 MyoPS: A benchmark of myocardial pathology segmentation combining three-sequence cardiac magnetic resonance images. **2023**, 87, 102808 ○
- 27 Role of intravenous alteplase on late lesion growth and clinical outcome after stroke treatment. 0271678X2311677 ○
- 26 Implementing a 3D printing service in a hospital. **2023**, 231-252 ○

- 25 Experimental validation of computational models for the prediction of phase distribution during multi-channel transcranial alternating current stimulation. ○
- 24 CT-Based Phenotyping and Genome-Wide Association Analysis of the Internal Structure and Components of Maize Kernels. **2023**, 13, 1078 ○
- 23 Prediction of Deep Myometrial Infiltration, Clinical Risk Category, Histological Type, and Lymphovascular Space Invasion in Women with Endometrial Cancer Based on Clinical and T2-Weighted MRI Radiomic Features. **2023**, 15, 2209 ○
- 22 A low-rank deep image prior reconstruction for free-breathing ungated spiral functional CMR at 0.55 T and 1.5 T. ○
- 21 Fast, light, and scalable: harnessing data-mined line annotations for automated tumor segmentation on brain MRI. ○
- 20 Automatic and manual segmentation of the piriform cortex: Method development and validation in patients with temporal lobe epilepsy and Alzheimer's disease. ○
- 19 Arterial spin labelling reveals multi-regional cerebral hypoperfusion in patients with transient ischemic attack that are unrelated to ischemia location: A proof-of-concept study. **2023**, 4, 100164 ○
- 18 Two-Phase Flow Simulation of Capillary Underfilling as a Design Tool for Heterogenous Integration. **2023**, ○
- 17 Longitudinal alterations in brain microstructure surrounding subcortical ischemic stroke lesions detected by free-water imaging. ○
- 16 Exploring the peripheral mechanisms of lower limb immobilisation on muscle function using novel electrophysiological methods. **2023**, ○
- 15 Single-cell DNA Methyloome and 3D Multi-omic Atlas of the Adult Mouse Brain. ○
- 14 Near-wall hemodynamic parameters quantification in in vitro intracranial aneurysms with 7 T PC-MRI. ○
- 13 Volume of hyperintense inflammation (VHI): A quantitative imaging biomarker of inflammation load in spondyloarthritis, enabled by human-machine cooperation. **2023**, 18, e0284508 ○
- 12 BOUNTI: Brain vOlumetry and aUtomated parcellationN for 3D feTal MRI. ○
- 11 Evolution of cortical geometry and its link to function, behaviour and ecology. **2023**, 14, ○
- 10 Histopathological correlations and fat replacement imaging patterns in recessive limb-girdle muscular dystrophy type 12. ○
- 9 Co-existing intracranial and extracranial carotid atherosclerosis predicts large-artery atherosclerosis stroke recurrence: a single-center prospective study utilizing combined head-and-neck vessel wall imaging. ○
- 8 Early-life obesogenic environment integrates immunometabolic and epigenetic signatures governing neuroinflammation. ○

7	Restoration of normal blood flow in atherosclerotic arteries promotes plaque stabilization. 2023 , 26, 106760	
6	Neurobehavioral sex-related differences in Nf1+/±mice: female show a flamouflaging±type behavior. 2023 , 14,	
5	A multicenter study of artificial intelligence-aided software for detecting visible clinically significant prostate cancer on mpMRI. 2023 , 14,	
4	MRI-derived tumor volume as a predictor of biochemical recurrence and adverse pathology in patients after radical prostatectomy: a propensity score matching study.	
3	Young versus older subject diffusion magnetic resonance imaging data for virtual white matter lesion tractography.	
2	Development and optimisation of a preclinical cone beam computed tomography-based radiomics workflow for radiation oncology research. 2023 , 26, 100446	
1	Insights into the Age Dependency of Compositional MR Biomarkers Quantifying the Health Status of Cartilage in Metacarpophalangeal Joints. 2023 , 13, 1746	